

Annual Report  
Jahresbericht

2010



WALTHER-MEISSNER-INSTITUT  
für Tieftemperaturforschung  
Bayerische Akademie der Wissenschaften





**Contact:**

Prof. Dr. Rudolf Gross  
Walther-Meißner-Institut für Tieftemperaturforschung  
Bayerische Akademie der Wissenschaften  
and  
Lehrstuhl für Technische Physik – E23  
Technische Universität München

**Address:**

Walther-Meißner-Str. 8	Phone:	+49 – (0)89 289 14201
D - 85748 Garching	Fax:	+49 – (0)89 289 14206
GERMANY	e-mail:	Rudolf.Gross@wmi.badw.de
	WWW-address:	<a href="http://www.wmi.badw.de">http://www.wmi.badw.de</a>

**Secretary's Office and Administration:**

<b>Emel Dönertas</b>	Phone:	+49 – (0)89 289 14202
	Fax:	+49 – (0)89 289 14206
	e-mail:	Emel.Doenertas@wmi.badw.de Sekretariat@wmi.badw.de

<b>Ludwig Ossiander</b>	Phone:	+49 – (0)89 289 14205
	Fax:	+49 – (0)89 289 14206
	e-mail:	Ludwig.Ossiander@wmi.badw.de



## Preface

Dear friends, partners, and alumni of the Walther-Meißner-Institute for Low Temperature Research (WMI) of the Bavarian Academy for Sciences and Humanities (BAdW)!

On behalf of the members of WMI I am pleased to present to you our *Annual Report 2010*. WMI is looking back on a highly successful year 2010. We succeeded to further extend our efforts in research and teaching and keep our internationally leading position in several areas of low temperature research. The report is aiming to provide not only concise summaries of our ongoing research projects and their major results, but also information on our teaching activities as well as interesting data about publications, completed and ongoing Ph.D., diploma, bachelor and master theses, collaborations, funding, and recent developments in infrastructure and experimental facilities.

In 2010, WMI was involved in several long-term, coordinated research programs jointly put into effect in collaboration with partners from both Munich universities and other national and international research institutions. In some of these programs the WMI is playing a leading role and providing the spokesman of the program. I would like to particularly mention our successful work in the *Cluster of Excellence Nanosystems Initiative Munich* (see <http://www.nano-initiative-munich.de/>), the *Collaborative Research Center 631* (Solid State Quantum Information Processing, see <http://www.wmi.badw-muenchen.de/SFB631>), the *Transregional Collaborative Research Center TRR 80* (From Electronic Correlations to Functionality, see <http://www.trr80.de/trr80>), the *Research Unit FOR 538* (High Temperature Superconductivity, see <http://www.wmi.badw-muenchen.de/FG538>), and the *DFG Priority Programs 1285* (Semiconductor Spin Electronics) and *1458* (High Temperature Superconductivity in the Iron-Pnictides). Various other national and international research projects of WMI have been successfully continued in 2010 and promising new projects could be started. In particular, WMI started a new project on the *Doping Dependent Evolution of the Fermi Surface and Competing Ordering Phenomena in Superconducting Cuprates*, which already resulted in several high-level publications and was contributing to the approval of the new *Priority Program 1538* (Spin-Caloric Transport).

Our successful research in 2010 is reflected in many excellent publications, new extramural funding, collaborations with industry, and many invited presentations at national and international conferences. WMI also has organized national and international workshops and conferences, in this way promoting the scientific visibility of WMI. The total personnel of WMI, which has about doubled within the last 10 years, is reaching a saturation value: meanwhile about 70 people are working in the crowded laboratories and offices. The same is true for the outside funding, which was strongly increasing over the last decade and has reached a high level well above 1 Mio EUR per year. Regarding laboratory space, WMI succeeded to get extra money from the state government within the so-called "Konjunkturpaket II". This money has been used to establish the new *WMI Quantum Science Laboratory* in the basement of the building, providing about 150 m<sup>2</sup> additional laboratory space particularly suited for low temperature facilities and ultra-sensitive studies on solid state quantum systems. The building activities have been started late in 2009 and new laboratories will become operational early in 2011.

A key factor for the high level of scientific productivity of WMI is the collaborative atmosphere, the commitment and high motivation of its research and technical staff as well as the support of various funding agencies. In this context we gratefully acknowledge financial support from the BAdW, the DFG, the Bavarian Ministry for Science and Arts, the BMBF and the

EU. A further key to our success in research is the recruitment of outstanding, scientifically independent group leaders with complementary research interests and technical expertise, a process which is supported and monitored by the scientific advisory board of WMI, and the excellent quality of our Ph.D., diploma and master students. We are particularly proud of the fact that Achim Marx was honored with the *Rotary Prize Hofgarten 2010* of the Bavarian Academy of Sciences and Humanities. In addition, Matteo Mariantoni was receiving a prestigious *Elings Prize Postdoctoral Fellowship* of the California Nanosystems Institute, which allowed him to start a post-doctoral stay at UC Santa Barbara after finishing his Ph.D. thesis. Despite the continuous expansion of WMI, we are much committed to support and promote young scientists in their career.

I hope that our Annual Report 2010 inspires your interest in WMI. I take this opportunity to thank all the colleagues, guests, students, post-docs and cooperating partners, who contributed to the success of our research and teaching activities within the last year, and last but not least all our friends and sponsors for their interest, trust and continuous support.



Rudolf Gross

Garching, December 2010



# Contents

Preface . . . . .	1
The Walther–Meißner–Institute . . . . .	5
<b>Reports:</b>	<b>9</b>
<b>Joint Research Project</b>	<b>9</b>
The Collaborative Research Center 631 . . . . .	11
The Nanosystems Initiative Munich – NIM . . . . .	16
<b>Fifty Years of Fluxoid Quantization</b>	<b>19</b>
The Discovery of Fluxoid Quantization: $2e$ or not $2e$ . . . . .	21
<b>Basic Research</b>	<b>27</b>
From Strong to Ultrastrong Coupling in Circuit Quantum Electrodynamics . . . . .	29
Dual-Path State Reconstruction Scheme for Propagating Quantum Microwaves and Detector Noise Tomography . . . . .	32
Characterization of a Flux-Driven Josephson Parametric Amplifier . . . . .	34
Ultrastrong Coupling in Circuit Quantum Electrodynamics . . . . .	36
Response and Transport in Non–Centrosymmetric Superconductors . . . . .	40
Superconductivity at High Transition Temperatures . . . . .	45
Investigating the Doping-Dependent Fermi Surface of the Superconducting Cuprate $\text{Nd}_{2-x}\text{Ce}_x\text{CuO}_4$ with the Help of High Magnetic Fields . . . . .	47
Doping Dependence of the Electronic Properties of $\text{Ba}(\text{Fe}_{1-x}\text{Co}_x)_2\text{As}_2$ . . . . .	49
Magnetic Transformations in the Organic Conductor $\kappa\text{-(BETS)}_2\text{Mn}[\text{N}(\text{CN})_2]_3$ at the Metal–Insulator Transition . . . . .	51
AC Susceptibility of $\text{YbRh}_2\text{Si}_2$ . . . . .	53

<b>Application–Oriented Research</b>	<b>55</b>
A Superconducting 180° Hybrid Ring Coupler for Circuit Quantum Electrodynamics	57
Absence of Both Ferromagnetism and <i>p</i> -type Conductivity in (Li,Ni)-Codoped ZnO Thin Films . . . . .	60
Magnetic Microstructure and Magnetotransport in Co <sub>2</sub> FeAl Heusler Compound Thin Films . . . . .	62
Magnetoresistance and Crystalline Symmetry in Heusler Compounds . . . . .	65
Intercalation and Dynamics of Hydrated Fe <sup>2+</sup> in Vermiculites from Santa Olalla and Ojén . . . . .	67
<b>Materials, Thin Film and Nanotechnology, Experimental Techniques</b>	<b>69</b>
A Cryogen-Free <sup>4</sup> He-JT-Stage. Retrofit of our Cryogen-Free Dilution Refrigerator. . . . .	71
Susceptibility Measurements in a Diamond Anvil Pressure Cell . . . . .	74
Broadband Microwave Spectroscopy of Magnetic Thin Films . . . . .	76
Colloidal Graphite Oxide, its Purification, Phase Transfer and Electrokinetic Properties	78
<b>Experimental Facilities</b>	<b>81</b>
The Quantum Laboratories: Installation of New Laboratory Space for Sensitive Quantum Experiments . . . . .	83
IT Infrastructure Upgrade at the WMI . . . . .	84
Overview of Key Experimental Facilities and Infrastructure . . . . .	85
<b>Publications</b>	<b>99</b>
<b>Theses, Appointments, Honors and Awards, Membership in Advisory Boards, etc.</b>	<b>103</b>
<b>Research Projects and Cooperations</b>	<b>109</b>
<b>Invited Conference Talks and Seminar Lectures</b>	<b>119</b>
<b>Seminars, Courses, Lectures and other Scientific Activities</b>	<b>125</b>
<b>Staff of the Walther-Meißner-Institute</b>	<b>135</b>
<b>Guest Researchers</b>	<b>137</b>
<b>Commission for Low Temperature Physics</b>	<b>139</b>

## The Walther–Meißner–Institute

### General Information

The Walther–Meißner–Institute for Low Temperature Research (WMI) is operated by the Commission for Low Temperature Research of the Bavarian Academy of Sciences and Humanities (BAdW). The commission was founded in 1946 on Walther Meißner's initiative, who was president of BAdW from 1946 to 1950. The Commissions (Research Groups) of the Academy are set up in order to carry out long-term projects, which are too ambitious for the lifetime or capacity of any single researcher, or which require the collaboration of specialists in various disciplines. At present, the Bavarian Academy of Sciences and Humanities consists of 36 Commissions with more than 300 employees.

The Commission for Low Temperature Research of the BAdW started its research activities in 1946 in the Herrsching barracks. After the retirement of Walther Meißner in 1952, Heinz Maier-Leibnitz, who followed Walther Meißner on the Chair for Technical Physics of the Technische Universität München, became the new head of the Commission for Low Temperature Research. In 1967, the commission moved to the Garching research campus after the construction of the new "Zentralinstitut für Tieftemperaturforschung" (ZTTF) was completed (director: Prof. Heinz Maier-Leibnitz, technical director: Prof. Franz Xaver Eder). Until 1972, the theory group of the Institute Laue Langevin was hosted at the ZTTF. In 1980, Prof. Dr. Klaus Andres became the new director of the ZTTF again associated with the Chair for Technical Physics (E23) at the Technische Universität München, followed by Prof. Dr. Rudolf Gross in 2000. In 1982, the ZTTF was renamed into Walther-Meißner-Institute for Low Temperature Research (WMI) on the occasion of Walther Meißner's 100. birthday.

As already mentioned, it is a long tradition that WMI hosts the Chair for Technical Physics (E 23) of the Technische Universität München (TUM) with the director of the WMI being full professor at the Faculty of Physics of TUM. However, there are also close ties with the Ludwig-Maximilians-Universität (LMU). Between 2004 and 2010, WMI hosted a scanning probe division with the head of this division being professor at the Ludwig-Maximilians-Universität (LMU). In this way a tight collaboration has been established between WMI and research groups of both Munich universities, joining technological and human resources in the fields of experimental and theoretical solid-state and condensed matter physics, low temperature techniques, materials science as well as thin film and nanotechnology. Noteworthy, the WMI supplies liquid helium to more than 25 research groups at both Munich universities and provides the technological basis for low temperature research.

### Research Activities

The research activities of the Walther–Meißner–Institute are focused on low temperature solid-state and condensed matter physics (see reports below). The research program is devoted to both **fundamental** and **applied research** and also addresses **materials science, thin film and nanotechnology** aspects. With respect to **basic research** the main focus of the WMI is on

- superconductivity and superfluidity,
- magnetism and spin transport,
- quantum phenomena in mesoscopic systems and nanostructures,
- self-organization of molecules on surfaces,

- and the general properties of metallic systems at low and very low temperatures.

The WMI also conducts **applied research** in the fields of

- solid-state quantum information processing systems,
- superconducting and spintronic devices,
- oxide electronics,
- multi-functional and multiferroic materials,
- and the development of low and ultra low temperature systems and techniques.

With respect to **materials science, thin film and nanotechnology** the research program is focused on

- the synthesis of superconducting and magnetic materials,
- the single crystal growth of oxide materials,
- the thin film technology of complex oxide heterostructures including multi-functional and multiferroic material systems,
- the fabrication of superconducting, magnetic, and hybrid nanostructures,
- and the growth of self-organized molecular ad-layers.

The WMI also develops and operates systems and techniques for low and ultra-low temperature experiments. A successful development have been dry mK-systems that can be operated without liquid helium by using a pulse-tube refrigerator for precooling. Meanwhile, these systems have been successfully commercialized by the company VeriCold Technologies GmbH at Ismaning, Germany, which was taken over by Oxford Instruments in 2007. As further typical examples we mention a nuclear demagnetization cryostat for temperature down to below 100  $\mu$ K, or very flexible dilution refrigerator inserts for temperatures down to about 20 mK fitting into a 2 inch bore. These systems have been engineered and fabricated at the WMI. Within the last years, several dilution refrigerators have been provided to other research groups for various low temperature experiments. The WMI also operates a helium liquifier with a capacity of more than 150.000 liters per year and supplies both Munich universities with liquid helium. To optimize the transfer of liquid helium into transport containers the WMI has developed a pumping system for liquid helium that is commercialized in collaboration with a company.

To a large extent the research activities of WMI are integrated into national and international research projects such as Clusters of Excellence, Collaborative Research Centers, Research Units, or EU projects. The individual research groups of WMI offer a wide range of attractive research opportunities for diploma (graduate) students, PhD students and postdoctoral fellows.

## **Experimental Facilities and Resources**

The WMI is equipped with state of the art facilities for the preparation and characterization of superconducting and magnetic materials as well as for various low and ultra-low temperature experiments. The main experimental and technological resources of WMI are listed in the following.

## Materials Preparation and Fabrication of Nanostructures

- Laser Molecular Beam Epitaxy (L-MBE) system for oxide heterostructures (equipped with in-situ RHEED, Omicron AFM/STM system, atomic oxygen/nitrogen source, infrared-laser heating system, metallization)
- molecular beam epitaxy (MBE) system for metallic systems
- UHV magnetron sputtering systems for metals (e.g. Nb, Al, NiPd, ... )
- magnetron sputtering system for oxide heteroepitaxy (equipped with four sputtering guns and an oxygen ion gun)
- reactive ion etching (RIE) system, Plasmalab 80 Plus with ICP plasma source, Oxford Instruments Plasma Technology
- ion beam etching (IBE) system equipped with a LN<sub>2</sub> cooled sample holder
- polishing machine for substrate preparation
- ultrasonic bonding machine
- 50 m<sup>2</sup> class 1000 clean room facility
- optical lithography (Süss maskaligner MJB 3 and projection lithography)
- electron beam lithography (based on Philips XL 30 SFEG scanning electron microscope and Raith Elphy Plus lithography system including a laser stage)
- four-mirror image furnace for crystal growth

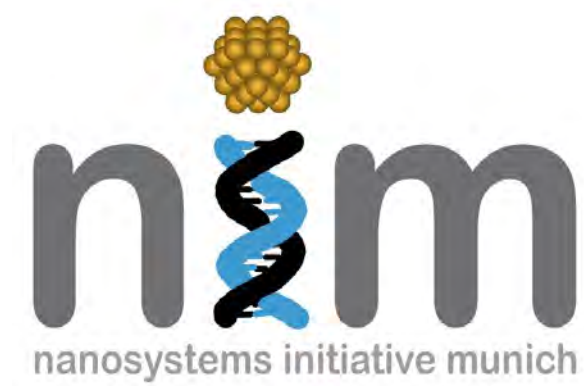
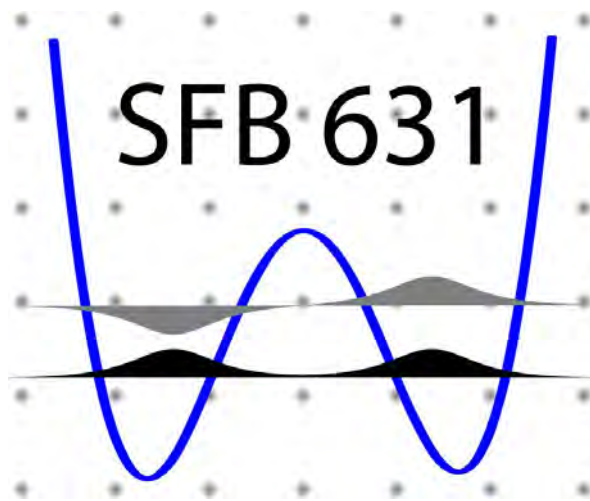
## Characterization

- 2-circle x-ray diffractometer (Bruker D8 Advance, sample temperature up to 1 600°C)
- high resolution 4-circle x-ray diffractometer with Göbel mirror and Ge monochromator (Bruker D8 Discover)
- scanning electron microscope with EDX analysis
- UHV room temperature AFM/STM system
- 2048 u high resolution mass spectrometer (Fa. Pfeiffer, cross beam ion source, SEM)
- Low Energy Electron Diffraction (SPECTA-LEED, Fa. Omicron)
- two Raman spectroscopy systems (1.5 to 300 K, in-situ sample preparation)
- SQUID magnetometer (Quantum Design, 1.5 to 700 K, up to 7 Tesla)
- several high field magnet systems (up to 17 Tesla) with variable temperature inserts
- 7 Tesla split coil magnet systems with optical access and variable temperature insert
- experimental set-ups for the measurement of noise including low noise SQUID amplifiers and signal analyzers
- high-frequency network analyzers (up to 40 GHz) and various microwave components (sources, mixers, circulators, attenuators) for the determination of high frequency parameters
- high-frequency cryogenic probing station (up to 20 GHz,  $T > 4$  K)
- magneto-optical Kerr effect (MOKE) system
- ferromagnetic resonance (FMR) system

**Low temperature systems and techniques**

- 5 K-Scanning Tunneling Microscope (low temperature STM, Fa. Omicron)
- several  $^3\text{He}/^4\text{He}$  dilution refrigerator inserts for temperatures down to 10 mK
- “dry” mK-cooler based on a dilution refrigerator with pulse-tube precooling
- ultra-low temperature facility for temperatures down to below  $100\ \mu\text{K}$  based on a nuclear demagnetization cryostat
- experimental set-ups for the measurement of specific heat, magnetization, thermal expansion as well as electrical and thermal transport properties as a function of temperature, magnetic field and pressure

# Joint Research Projects

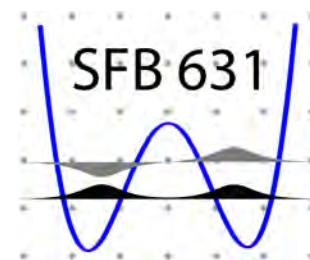




## The Collaborative Research Center 631

R. Gross, A. Marx, F. Deppe<sup>1</sup>

Quantum information science is a fascinating and one of the most rapidly growing fields of science and technology, residing at the interface between physics, mathematics, computer and materials science, and engineering. It is concerned with both fundamental questions and technological developments, aiming at the realization of a useful quantum information hardware. Over the last decade, the physics of solid state quantum systems has developed into a key research field of Walther-Meißner-Institute (WMI). It requires extremely sensitive measurements at low and ultra-low temperatures and therefore perfectly fits to the research profile of WMI.



Solid state systems are considered a particularly promising platform for the successful implementation of quantum information systems. The Collaborative Research Center 631 (SFB 631) studies the *physical concepts, materials aspects, and technological foundations of solid state quantum information processing (SQIP)*. It deals with the coherent dynamics of solid state quantum systems and has the vision to engineer them so as to allow to process and communicate information on the basis of quantum mechanical principles. To realize this vision, SFB 631 aims at the clarification of the key physical questions as well as the materials aspects and technological problems that have to be solved for the successful implementation of SQIP. Particular goals are to design and implement solid state quantum bits (qubits) with long coherence times, to learn how to efficiently control, manipulate and read-out qubits, to couple them to complex systems as well as to develop theoretical tools for modeling the dynamics of driven, damped qubits in different experimental systems. The long-term goal is the development of small-scale solid state quantum systems that are capable of performing elementary processing and communication of quantum information. This involves the design, fabrication and investigation of solid state qubits, oscillators, cavities and transmission lines that can be combined to create hybrid quantum circuits.

To cover the broad spectrum of fundamental and application oriented questions related to solid state quantum information systems in a comprehensive way, SFB 631 joins research activities from quantum information theory, experimental and theoretical solid state physics, quantum optics, materials science, and nanotechnology. Today, within SFB 631 research groups from the Bavarian Academy of Sciences and Humanities (BAW), the TU Munich (TUM), the Ludwig-Maximilians-University (LMU), the Max-Planck-Institute for Quantum Optics (MPQ), as well as Augsburg and Regensburg University are collaborating in 18 research projects. The main objective is to obtain a profound understanding of the physics, technology, and materials aspects of SQIP by making use of advanced experimental and theoretical methods in a coordinated interdisciplinary research effort. At present, SFB 631 joins more than 30 principal investigators and more than 60 Ph.D. and diploma students, as well as a large number of postdocs and guest scientists. WMI is one of the main actors, providing the coordination of the center from the beginning (spokesman: Rudolf Gross). SFB 631 has been established in 2003 and a second four-year funding period has been granted by the German Research Foundation (DFG) in 2007. Late in 2010, the funding proposal for the third four-year funding period (07/2011 – 06/2015) has been completed and submitted to the German Research Foundation. The review meeting is scheduled for February 2011.

<sup>1</sup>This work is supported by the German Research Foundation through SFB 631.

Within the project A3 on *Superconducting Quantum Circuits as Basic Elements for Quantum Information Processing* and project A8 on *Cavity Quantum Electrodynamics with Superconducting Devices*, the research program of WMI within SFB 631 is focussing on the fabrication and study of superconducting quantum information circuits. This includes the fabrication of superconducting flux qubits in which quantum mechanical superposition states of clockwise and counter-clockwise circulating persistent currents are used for the realization of solid state qubits. These qubits are coupled to superconducting microwave resonators. In this way fascinating quantum electrodynamic experiments with deliberately designed artificial solid state atoms become possible. Since such experiments are completely analogous to quantum optical experiments on natural atoms in optical resonators, this prospering new field is called circuit quantum electrodynamics (circuit QED). Here, particular goals are the strong coupling of superconducting qubits to high-quality superconducting microwave resonators, the generation and detection of non-classical microwave Fock states, the development of dispersive read-out and quantum non-demolition measurements, and the entanglement of superconducting qubits via multiple resonators. Regarding these research goals the WMI team closely collaborates with the theory groups at LMU (von Delft), the University of Augsburg (Hänggi, Reuther), the Universidad del País Vasco - Euskal Herriko Unibertsitatea at Bilbao (Solano), and the Canadian Institute for Quantum Computing at Waterloo (Wilhelm), as well as the experimental groups at the NTT Basic Research Laboratories (Semba) and the Nano Electronics Research Laboratories at NEC Corporation, Japan (Nakamura, Tsai, Yamamoto). The research work within SFB 631 is also closely linked to the activities within Research Area 1 of the Cluster of Excellence *Nanosystems Initiative Munich (NIM)* (see pp. 16–18).

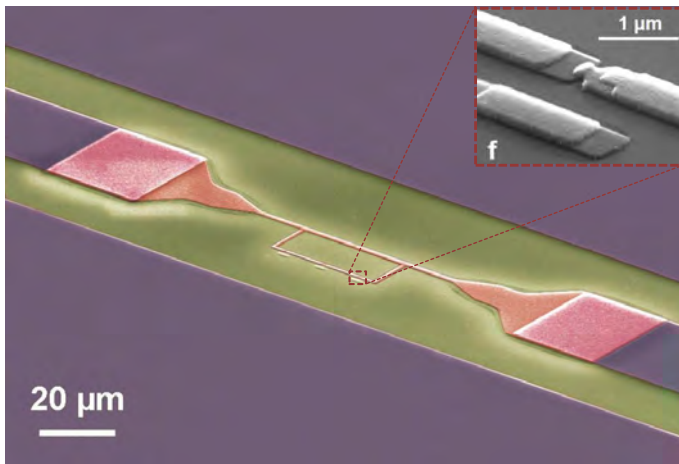


**Figure 1:** Scanning electron microscope image of a superconducting flux quantum bit (aluminium, red) galvanically coupled to the center conductor of a superconducting coplanar waveguide resonator (niobium, violet). The superconducting loop intersected by four about  $100 \times 100 \text{ nm}^2$  sized Josephson junctions (see inset) in the center of the image forms an artificial superconducting atom interacting with the microwave photons of the resonator. The structure has been used to demonstrate ultra-strong light-matter interaction.

### Ultrastrong light-matter interaction.

In 2010, the WMI qubit group could make several important contributions to the field of superconducting quantum circuits resulting in several high-level publications [1–6]. As shown in the reports by Deppe *et al.* (see pp. 29–31) and Niemczyk *et al.* (see pp. 36–39) we successfully could perform a series of beautiful circuit QED experiments with 3-Josephson junction flux qubits placed in Nb microwave coplanar waveguide resonators. As a highlight, in a collaboration with our partners from Spain and Augsburg we managed to enhance the light-matter interaction strength to the so-called “*ultra-strong coupling*” regime [1]. The interaction between matter and light is one of the most

fundamental processes in physics and has far reaching relevance for our everyday life. In the field of cavity QED this process is studied on the most fundamental level in systems consisting of only a single atom and photon. However, the interaction strength between light and natural atoms is very weak, making such experiments very demanding. Typically, the interaction strength  $g$  is many orders of magnitude smaller than the spacing  $\omega_q$  of the energy levels of

the atom. In our experiments we now could demonstrate a strongly enhanced light-matter interaction. This breakthrough was achieved in solid state systems formed by artificial superconducting atoms and microwave photons trapped in superconducting resonators. With these ingredients we were able to reach the so-called ultra-strong coupling regime, where the light-matter interaction  $g$  is of the same order of magnitude as the atom level spacing  $\omega_q$ . In this regime, light and matter are coupled so strongly that the coupled system has to be viewed as a new entity, a weird kind of molecule consisting of matter and light. Accessing the ultra-strong coupling regime opens fascinating new possibilities. On the one hand, this regime allows for novel experiments on fundamental quantum physics. On the other hand, it is a key ingredient for applications in solid state quantum information processing, which is considered a promising candidate for the next generation information technology.

Of course, we had to play some tricks to achieve the ultra-strong coupling between matter and light. First, the photon has to be locked up in a box allowing one to store the photon for a sufficiently long time. This box was realized by a high quality factor superconducting microwave resonator consisting of a quasi-one-dimensional electrical circuit with two highly reflecting “mirrors”. Second, the artificial superconducting atom has to be placed in the same box at a suitable position. In reality, the whole structure is fabricated as a superconducting circuit on a silicon chip using nanotechnology tools. Now, ultra-strong coupling is simply achieved by making the artificial atom very big (much bigger than natural atoms) and the photon box very small. It is obvious that in this case the photon can more easily “hit” the big atom and “comes close” to it due to the small box size. Translated to the language of physics, big atom simply means big dipole moment and small cavity small mode volume. The huge coupling achieved in our experiments has been realized by an additional circuit element, a so-called Josephson junction, which is unique to the world of superconducting circuits. With all these tricks the interaction strength could be increased to the astonishing level of 12% of the resonator frequency. This value is an order of magnitude larger than the values obtained previously in other circuit QED experiments and many orders of magnitude larger than the coupling achieved in experiments with natural atoms.

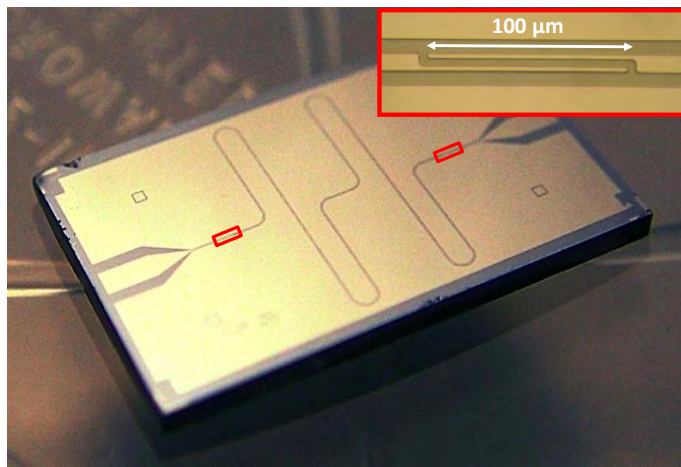


**Figure 2:** Optical micrograph of a coplanar waveguide resonator acting as a microwave photon box in circuit QED experiments. The inset shows one of the two coupling capacitors, playing the role of the mirrors in cavity QED.

Although we are quite happy to have achieved ultra-strong coupling between matter and light, at the same time this gives us a hard time. Owing to the huge light-matter coupling, the spectra observed in our experiments can no longer be explained by the renowned but simple Jaynes-Cummings model. The spectra rather belong to a novel complex object which can be considered a light-matter-molecule. The study of its detailed structure will keep us busy and in good mood.

**Tomography of propagating quantum microwaves.** In circuit QED experiments it is necessary to investigate not only fields confined in cavities but also propagating states of the

electromagnetic field, which for example are created, when a state is leaking out of a resonator. As shown in the report by Menzel *et al.* (see pp. 32–33) we succeeded to develop a novel experimental technique – the so-called dual path method – which allows us to reconstruct propagating quantum microwaves and to perform detector noise tomography. With this method we can determine – even in the presence of significant amplifier noise – all quadrature moments of propagating quantum microwaves based on cross-correlations from the dual-path amplification setup. Simultaneously, the detector noise properties are determined, allowing for tomography. We demonstrated the feasibility of our novel concept by proof-of-principle experiments with classical mixtures of weak coherent microwaves [2].

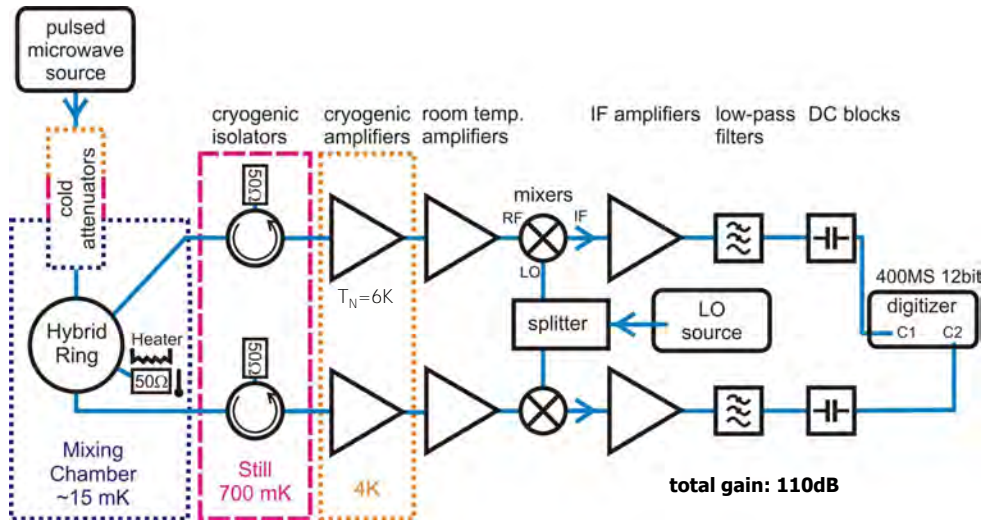


Figure 3: Circuit diagram of the dual path setup for the tomography of quantum microwaves.

**Planck spectroscopy.** Our ultra-sensitive detection scheme also has been successfully applied to perform Planck spectroscopy experiments, which allowed us to characterize microwave vacuum fluctuations as a function of frequency [3]. Furthermore, we provided clear experimental evidence that such vacuum fluctuations represent the fundamental minimum quantum noise added by a beam splitter to any given input signal.

**Microwave beam splitters and multi resonator systems.** An important ingredient of circuit QED experiments are microwave beam splitters. As shown in the report by Hoffmann *et al.* (see pp. 57–59) we successfully fabricated superconducting  $180^\circ$  hybrid ring couplers on both sapphire and silicon substrates, acting as microwave beam splitters. In a 2 GHz-band centered at 6 GHz, the devices show an almost ideal coupling of  $-3.5 \pm 0.5$  dB and an isolation of at least  $-15$  dB. The performance of these hybrid rings is suitable for experiments with propagating quantum microwaves [4]. We also made considerable progress in designing and fabricating a superconducting quantum switch based on two-resonator circuit QED [7]. In particular, in collaboration with the theory group at Augs-

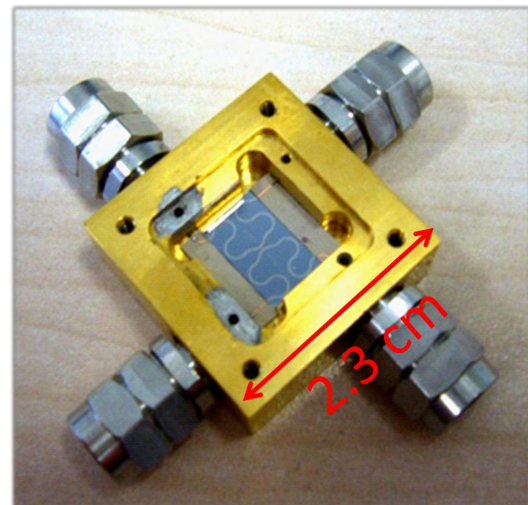


Figure 4: A superconducting multi-resonator circuit mounted in the sample box.

burg (Reuther, Hänggi) a detailed theoretical understanding for the dissipative two-resonator circuit QED setup was established [5].

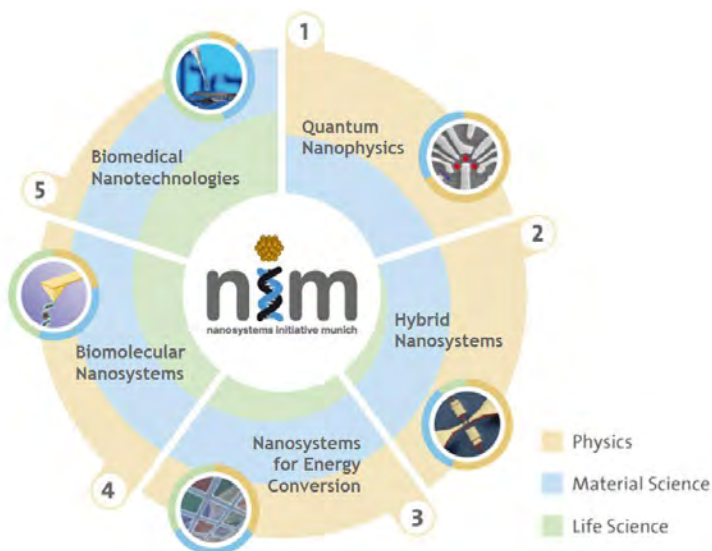
## References

- [1] T. Niemczyk, F. Deppe, H. Huebl, E. P. Menzel, F. Hocke, M. J. Schwarz, J. J. Garcia-Ripoll, D. Zueco, T. Hümmer, E. Solano, A. Marx, and R. Gross, *Nature Phys.* **6**, 772 (2010).
- [2] E. P. Menzel, F. Deppe, M. Mariantoni, M. A. Araque Caballero, A. Baust, T. Niemczyk, E. Hoffmann, A. Marx, E. Solano, and R. Gross, *Phys. Rev. Lett.* **105**, 100401 (2010).
- [3] M. Mariantoni, E. P. Menzel, F. Deppe, M. A. Araque Caballero, A. Baust, T. Niemczyk, E. Hoffmann, E. Solano, A. Marx, and R. Gross, *Phys. Rev. Lett.* **105**, 133601 (2010).
- [4] E. Hoffmann, F. Deppe, T. Niemczyk, T. Wirth, E. P. Menzel, G. Wild, H. Huebl, M. Mariantoni, T. Weisßl, A. Lukashenko, A. P. Zhuravel, A. V. Ustinov, A. Marx, and R. Gross, *Appl. Phys. Lett.* **97**, 222508 (2010).
- [5] G. M. Reuther, D. Zueco, F. Deppe, E. Hoffmann, E. P. Menzel, T. Weisßl, M. Mariantoni, S. Kohler, A. Marx, E. Solano, R. Gross, and P. Hänggi, *Phys. Rev. B* **81**, 144510 (2010).
- [6] B. G. U. Englert, G. Mangano, M. Mariantoni, R. Gross, J. Siewert, and E. Solano, *Phys. Rev. B* **81**, 134514 (2010).
- [7] M. Mariantoni, F. Deppe, A. Marx, R. Gross, F. K. Wilhelm, and E. Solano, *Phys. Rev. B* **78**, 104508 (2008).

## The Nanosystems Initiative Munich – NIM

R. Gross, S.T.B. Gönnenwein, H. Huebl, A. Marx<sup>1</sup>

The physics of quantum nanosystems is one of the main research directions of the Cluster of Excellence *Nanosystems Initiative Munich (NIM)* and also is the focus of several research activities at WMI. The NIM research areas dominated by quantum effects include single-electron and single-spin behavior at lowest temperatures, nanophotonic experiments, and investigation of practical strategies for quantum computation. To this end, a particular research direction of WMI focuses on quantum and correlation effects in hybrid mesoscopic structures consisting of superconducting, dielectric and magnetic materials. A further specific WMI activity addresses the fabrication, control/manipulation of magnetization direction, and spin transport in spin-nanosystems. Finally, in a collaboration with the group of Tobias Kippenberg from Max-Planck-Institute for Quantum Optics we started to design, fabricate and study electro-mechanical hybrid nanosystems.



NIM is one of the Clusters of Excellence which have been established in 2006 by the German government's *Excellence Initiative*. Within NIM, scientists from various research facilities in the greater Munich area in the fields of physics, biophysics, physical chemistry, biochemistry, biology, electrical engineering, and medicine are collaborating. The cluster joins research groups from LMU Munich, TU Munich, WMI, the University of Augsburg, the Munich University of Applied Science, the Max-Planck-Institutes

for Biochemistry and Quantum Optics, and the Deutsches Museum. It merges their combined expertise on man-made and biological nanoscale systems into a coherent and focused nanoscience cluster. While many individual nanoscale building blocks and components have been devised in recent years using top-down and bottom-up strategies, little is known about their integration into entire functional systems. The overarching vision guiding the research in NIM is therefore to design, fabricate and achieve control of a broad range of artificial and multi-functional nanoscale systems, and to unlock their potential for possible applications in fields as diverse as future information technologies, the life sciences, or combinations of both. To this end, it is essential to gain a fundamental understanding of their properties and behavior, which range from being purely quantum mechanical to being governed mainly by stochastic effects.

At WMI, several groups (Deppe, Gönnenwein, Gross, Huebl, Marx) are actively participating in the research program of NIM in the research areas 1: *Quantum Nanophysics* and 2: *Hybrid*

<sup>1</sup>This work is supported by the German Excellence Initiative via the Nanosystems Initiative Munich (NIM).

**Nanosystems.** In *Research Area 1* (coordinated by R. Gross, WMI), our research activities focus on the fabrication and characterization of spin-nanosystems, as well as on complex hybrid nanosystems composed of normal metals (N) and correlated electron materials (e.g. superconductors (S), ferro- (F) and antiferromagnets (AF)). Regarding the latter, the key goal is the control and manipulation of magnetization as well as the study of spin transport in magnetic nanosystems. To this end, considerable progress has been achieved within the last year [1–5].

For example, in the pioneering work by Czeschka *et al.* [1] the DC voltage  $V_{\text{ISH}}$  induced by spin pumping together with the inverse spin Hall (ISH) effect in ferromagnet/platinum bilayer films were systematically measured. For a large variety of different samples, comprising ferromagnetic  $3d$  transition metals, Heusler compounds, ferrite spinel oxides, and magnetic semiconductors, it was found that  $V_{\text{ISH}}$  invariably has the same polarity. Furthermore,  $V_{\text{ISH}}$  was found to scale with the magnetization precession cone angle with a universal prefactor, irrespective of the magnetic properties, the charge carrier transport mechanism or type. With these findings the present theoretical understanding of spin pumping in combination with the inverse spin Hall effect could be quantitatively corroborated.

In another research activity within *Research Area 1*, the experimental group at WMI and the theory groups at LMU (von Delft), TUM (Hartmann), U. of Augsburg (Reuther, Hänggi) and MPQ (Cirac, Giedke) are aiming at the study of superconducting qubits coupled to microwave resonators [6–11]. This new and very promising field of solid state quantum information processing is denoted as circuit quantum electrodynamics (circuit QED) and is analogue to cavity quantum electrodynamics in atom optics. In this field the research activities within NIM are closely linked to those of SFB 631 described already above (see pp. 11–15).

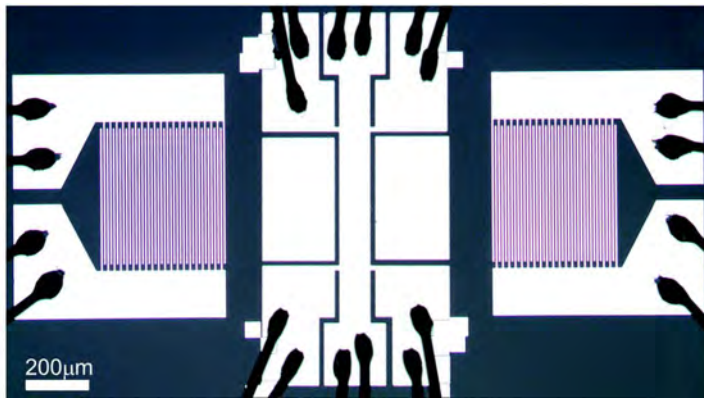


**Figure 1:** Sample chip for acoustically driven ferromagnetic resonance experiments consisting of two interdigital transducers for the generation and detection of surface acoustic waves and a Ni thin film structure in between.

tion is controlled via elastic mechanical strain generated by an applied electric field. That is, in this spin mechanics scheme we take advantage of the elastic channel to establish a continuous, reversible, electric-field control of magnetization orientation. Recently, Weiler *et al.* [2] successfully developed surface acoustic wave based device structures to perform a spin-mechanical control of magnetism at microwave frequencies. It is well known that the audible hum of a transformer is due to magnetostriction, describing the elastic deformation of a ferromagnetic body induced by a magnetic field. The inverse effect, magnetoelasticity, enables the control of magnetization via elastic stress. This spin-mechanical interaction prevails at radio frequencies (RF), so that magnonic and phononic degrees of freedom become coupled. We experimentally demonstrated that a purely elastic stimulus allows

In *Research Area 2* (coordinated by A. Wixforth, Augsburg), the WMI research activities focus on spin mechanics. It is well known that the magnetization of a ferromagnet can be controlled by means of a magnetic field. However, for nanodevices an electric field control would be more feasible. We could show that such an electric-field control of magnetization becomes indeed possible in multi-functional ferromagnetic-ferroelectric hybrid structures, where the magnetization direc-

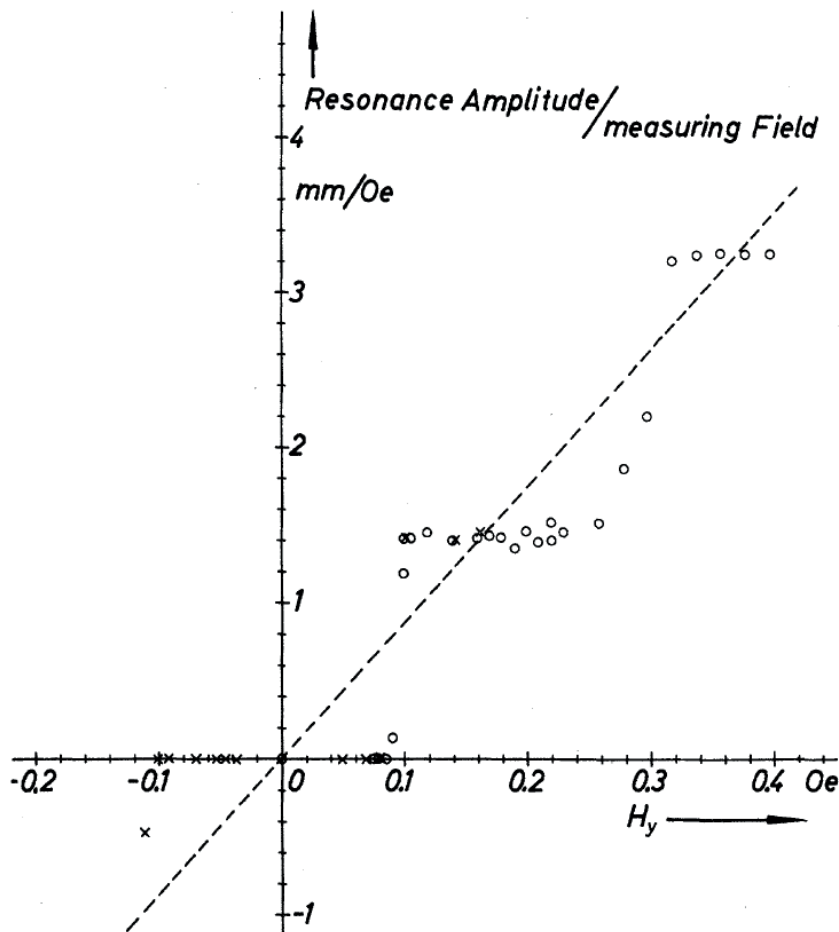
to resonantly drive magnetization dynamics in a ferromagnetic thin film. A hypersound surface acoustic wave (SAW) is launched in a microfabricated ferromagnetic/ferroelectric hybrid device. The SAW excites an RF magnetization precession in the ferromagnet, and probes its back-action onto the elastic properties of the hybrid. Our experiments open the path to study RF spin mechanics, e.g., the interaction of magnetic and elastic modes at radio frequencies, the interconversion of magnetic and elastic excitations, mechanical spin pumping, or magnetoelastic magnetization damping.

A new research field started at WMI about two years ago is nano-mechanics. Over the last few years opto-mechanical systems have become a topic of considerable interest. In such systems nano-mechanical harmonic oscillators are coupled to the electromagnetic field inside a suitable cavity. At sufficiently strong coupling, such systems allow to explore various quantum effects such as superposition and entanglement, or the generation of cat states at a macroscopic scale. Furthermore, they may allow to perform ultra-sensitive measurements on macroscopic objects or to combine opto-mechanical systems in the microwave regime with nonlinear circuit elements such as Josephson junctions or qubits. In a collaboration between the NIM research areas 1 and 2 we have fabricated electro-mechanical nanosystems consisting of a superconducting nanobeam coupled to a high quality factor superconducting microwave resonator.

## References

- [1] F. D. Czeschka, L. Dreher, M. S. Brandt, M. Weiler, M. Althammer, I. Imort, G. Reiss, A. Thomas, W. Schoch, W. Limmer, H. Huebl, R. Gross, and S. T. B. Goennenwein, ArXiv e-prints **1012.3017** (2010).
- [2] M. Weiler, L. Dreher, C. Heeg, H. Huebl, R. Gross, M. S. Brandt, and S. T. B. Goennenwein, ArXiv e-prints **1009.5798** (2010).
- [3] M. Weiler, F. D. Czeschka, I. Imort, G. Reiss, A. Thomas, G. Woltersdorf, R. Gross, and S. T. B. Goennenwein, ArXiv e-prints **1011.1417** (2010).
- [4] S. Goennenwein, Europhysics News **41(4)**, 17 (2010).
- [5] S. Geprägs, A. Brandlmaier, M. Opel, R. Gross, and S. T. B. Goennenwein, Applied Physics Letters **96**, 142509 (2010).
- [6] T. Niemczyk, F. Deppe, H. Huebl, E. P. Menzel, F. Hocke, M. J. Schwarz, J. J. Garcia-Ripoll, D. Zueco, T. Hümmer, E. Solano, A. Marx, and R. Gross, Nature Phys. **6**, 772 (2010).
- [7] E. P. Menzel, F. Deppe, M. Mariantoni, M. A. Araque Caballero, A. Baust, T. Niemczyk, E. Hoffmann, A. Marx, E. Solano, and R. Gross, Phys. Rev. Lett. **105**, 100401 (2010).
- [8] M. Mariantoni, E. P. Menzel, F. Deppe, M. A. Araque Caballero, A. Baust, T. Niemczyk, E. Hoffmann, E. Solano, A. Marx, and R. Gross, Phys. Rev. Lett. **105**, 133601 (2010).
- [9] E. Hoffmann, F. Deppe, T. Niemczyk, T. Wirth, E. P. Menzel, G. Wild, H. Huebl, M. Mariantoni, T. Weisßl, A. Lukashenko, A. P. Zhuravel, A. V. Ustinov, A. Marx, and R. Gross, Appl. Phys. Lett. **97**, 222508 (2010).
- [10] G. M. Reuther, D. Zueco, F. Deppe, E. Hoffmann, E. P. Menzel, T. Weisßl, M. Mariantoni, S. Kohler, A. Marx, E. Solano, R. Gross, and P. Hänggi, Phys. Rev. B **81**, 144510 (2010).
- [11] B. G. U. Englert, G. Mangano, M. Mariantoni, R. Gross, J. Siewert, and E. Solano, Phys. Rev. B **81**, 134514 (2010).

# Fifty Years of Fluxoid Quantization



Original experimental data of Doll and Näbauer demonstrating flux quantization in multiply connected superconductors in units of  $\Phi_0 = h/2e$  (according to R. Doll, M. Näbauer, *Phys. Rev. Lett.* 7, 51 (1961)). In the figure, the resonance amplitude divided by the measuring field  $H_x$  is plotted as a function of the applied cooling field  $H_y$ . The measured resonance amplitude is directly proportional to the magnetic flux frozen in a Pb cylinder during cooldown below the transition temperature.



## The Discovery of Fluxoid Quantization: $2e$ or not $2e$

*D. Einzel*

**Introduction.** The year 2011 is quite remarkable because it allows us to celebrate not only the centennial of the discovery of superconductivity by Heike Kamerlingh–Onnes [1] in 1911, but also the half–centennial of the discovery of what is referred to as *fluxoid quantization* in superconductors by Robert Doll and Martin Nábauer [2, 3], and, independently, by Bascom S. Deaver Jr. and William Fairbank [4]. Theoretically, the quantized fluxoid  $\Phi = n\Phi_0$ ,  $n = 0, \pm 1, \pm 2, \dots$  in a hollow superconducting cylinder is characterized by the quantum  $\Phi_0 = hc/ke$  with  $e$  the elementary charge and  $k$  the pair parameter, which allows to distinguish the cases of fictive charged bosons ( $k = 1$ ) and Fermion pairs ( $k = 2$ ). In 1950, Fritz London predicted the existence of  $\Phi_0$  [5], however with  $k = 1$ , whereas in 1958 Lars Onsager proposed that  $\Phi_0$  has to be applied to the case  $k = 2$ , thus anticipating the consequence of electron pairing. The experimental proof of the quantization of magnetic flux in hollow superconducting cylinders actually supports two important theoretical concepts, namely the pairing hypothesis ( $k = 2$ ) formulated in the BCS theory of superconductivity [6] and the concept of macroscopic phase coherence of the pair condensate. This contribution is devoted to a discussion of the physics behind the Doll–Nábauer Deaver–Fairbank discoveries and is intended to review historically the chain of events which motivated these talented experimentalists and which led to their independent discoveries at quite remote points of the earth. An extended version of this work will be published in 2011 as a book chapter [7] and a long version of it has been submitted for publication as a review in the *Journal of Low Temperature Physics* [8].

**The Doll–Nábauer experiment.** Robert Doll was born in Munich on January 16, 1923. In 1946 he started studying Physics at the *Technische Hochschule* (TH) in Munich. In 1949 Robert Doll began his diploma thesis with Prof. Walther Meißner at the chair of Technical Physics of the TH Munich. Walther Meißner (born on December 16, 1882 in Berlin) can certainly be regarded as a pioneer of low temperature physics in Germany. He was renowned in the physics community at that time for various scientific and social activities and achievements [9]. The diploma work ended in 1953. In the same year, Walther Meißner offered Robert Doll the position of a permanent research assistant connected with the possibility to write a doctoral thesis. The topic of the doctoral thesis was the measurement of the "*Gyromagnetic effect in superconductors*". Doll eventually received his PhD from the TH in Munich in 1958.

In the beginning of 1960, Robert Doll, his colleague Martin Nábauer (born 11. 1. 1919 in Karlsruhe, Germany, who worked at Walther Meißner's institute in Herrsching since 1. 12. 1951) and Gerhard Schubert, a visiting Professor from the University of Mainz, were inspired by a footnote in the book of Fritz London [5] to develop the idea of measuring the fluxoid quantum in a hollow superconducting Pb cylinder. They believed this fluxoid to be of the form  $\Phi_0 = hc/e$  according to ref. [5]. Meißner was, at that time, definitely not involved in this decision making process. In order to inform Meißner about their intentions, Doll and Nábauer wrote a detailed development proposal, which they showed to Meißner. Meißner agreed after a certain period of hesitation and signalled, that he would not like to be involved with this project in the near future.

The experimental apparatus (i.e. the suspension of the torsional oscillator) for the measurement of the quantization effect existed already, having been used before to measure the gyromagnetic effect of small superconducting spheres in connection with Doll's doctoral thesis.

The obvious plan was to use it in order to measure the torque exerted on a hollow superconducting Pb cylinder (radius  $R$  and wall thickness  $d$ ) connected to it, which could directly be translated into the value of the trapped flux. So only the hollow Pb cylinder had to be newly constructed and the sensitivity of the oscillator had to be estimated carefully. Major difficulties arose in connection with the fabrication of the Pb hollow cylinder, particularly with the determination of its inner ( $R$ ) and outer ( $R + d$ ) radius. This was the state of affairs around the middle of 1960. In fact, the experiment proceeded to its success in clearly less than one year. The experimental procedure contained the following different steps:

1. Application of a certain value of an external field  $H^{\text{ext}}$  parallel to the axis of the Pb cylinder.
2. Cooling the sample in the field through the (field-dependent) transition temperature  $T_c(H^{\text{ext}})$ .
3. Complete removal of the external field.
4. Cooling the sample with the trapped flux down further to a final temperature of about  $0.6T_c$ .
5. Application of a small field  $B_M$  perpendicular to the cylinder axis in order to produce a torque.
6. Measurement of the torque and derivation from it the step height  $\propto \Phi$ .
7. Warming up above  $T_c$  to start a new measurement.

The first run did not lead to any exploitable result, since the external field increments were too large. This fact can be traced back to the fluxoid quantum proposed by London being a factor of 2 too large. In early 1961, in a second run, Doll and Näbauer reduced the increments for the steps in the externally applied field dramatically, beginning at zero field. At a field  $H^{\text{ext}}$  of 0.1 Oe, they realized, that there was a trapped flux inside their cylinder, accompanied by a sharp step in the observed torque. This way, by April 1961, they had discovered the first step in the fluxoid quantization profile. At this time, Doll and Näbauer could, however, not answer the question, of why their measured flux quantum differed from the London proposal by a factor of 1.6...1.7. Doll's comment was "*Es hat halt nicht gestimmt! (It just didn't agree!)*".

It turned out that the precise value of the fluxoid quantum  $\Phi_0 = hc/ke$  can be deduced from the range of external fields  $\Delta H^{\text{ext}}$ , for which no torque was measured. It can *not* be determined from the step height, into which complicated factors due to the properties of the torsional oscillator enter. Taking the *outer* radius  $a = R + d$  for the computation of the trapped flux  $\Phi = \Delta H^{\text{ext}} \pi a^2$ , which is meaningful in the large magnetic penetration depth limit  $\lambda_L > d$  just below  $T_c$ , when the flux gets frozen in, Doll and Näbauer obtained the result  $\Phi_0 = (0.49 \pm 20\%) hc/e \approx hc/2e$ , surprisingly close to the result predicted by the BCS theory [3].

When it became clear that Doll and Näbauer had discovered the quantization effect, various things happened. *First*, there was the plan, that Martin Näbauer should participate at the IBM conference in Yorktown Heights in June 1961 in order to give a seminar on the quantization effect. *Second*, a publication for *The Physical Review Letters* was planned. *Third*, when the success of this experiment became visible, Walther Meißner, having adopted a neutral position before, changed his mind and all of a sudden requested to be accepted as a coauthor on the publication. This was the situation in Herrsching right before the beginning of the IBM conference in Yorktown Heights, in June 1961. At this stage, it appears to be meaningful, to split the scene and investigate, what happened in a completely uncorrelated manner, on the other side of the earth, namely at Stanford University.

**The Deaver–Fairbank experiment.** Bascom S. Deaver was born on August 16, 1930 in Macon, Georgia, USA. He received his undergraduate B.S. degree from the Georgia Institute of Technology in the year 1952 and his masters degree at the Washington University in St. Louis in 1954. Between 1954 and 1957, he joined the U. S. Air Force at the Air Force Special Weapons Center at the Kirtland Air Force Base in New Mexico as a physicist and commissioned lieutenant. In spring 1958, Bascom Deaver, while working as a part-time graduate student at the Stanford Research Institute, Menlo Park, California, consulted his friend and Stanford Professor George Pake about what kind of research he should pursue. Pake strongly recommended working for Prof. William Martin Fairbank, who would be arriving at Stanford University in fall 1959.

Like Walther Meißner, William M. Fairbank (born on 14. 2. 1917 in Minneapolis, Minnesota) can be viewed as a pioneer of low temperature physics. Around 1959, he could look back already to a very productive academic career [10]. In Fall 1959, William Fairbank joined the faculty at Stanford University and became the Max von Stein Professor of Physics. It was actually Felix Bloch, who persuaded Fairbank to a change from Duke to Stanford. He stayed there until his retirement in 1985, and as an emeritus Professor until his sudden death in the year 1989. Following Prof. Pake's advice, Bascom Deaver applied for a doctoral thesis at Fairbanks research group. Among the experimental topics that William Fairbank proposed to Bascom Deaver was *The measurement of the fluxoid, proposed by Fritz London in 1950*. Bascom Deaver found this idea *enormously appealing* and, without great hesitation, asked Fairbank to be allowed to work on it in fall 1959.

Fairbank's experimental concept was the use of a tiny *tin* cylinder ( $13\mu\text{m}$  i.d.,  $L = 1\text{cm}$ ) which was vibrated along its symmetry axis at 100 Hz with an amplitude of 1 mm. Two pickup coils measured the magnetic flux in the cylinder at various values of the applied external field. The output voltage from the pickup coils was calibrated by cooling the cylinder from its normal state to well below the superconducting transition temperature in zero applied field, so that no flux was trapped, and then measuring the voltage as a function of applied field as the cylinder was vibrated. Assuming that the cylinder was completely diamagnetic, knowing the applied field and the measured outside diameter of the cylinder and thus the area, so the ejected flux was just the applied field times the outside area of the cylinder, the voltage was calibrated directly in flux ( $\text{Gs cm}^2$ ).

During the progress of Bascom Deaver's work, he heard of three other endeavors to search for quantized flux, all of them unsuccessful. Therefore it is quite remarkable, that Deaver and Fairbank did not become aware of the fourth endeavor, namely the ongoing Doll–Näbauer experiment at Walther Meißner's institute in Herrsching, and vice versa. On May 3, 1961 Bascom S. Deaver could report the first definitive signature of quantized flux. He was at first surprised though, that the measured flux was so different from the value London predicted. However, Bill Fairbank quickly recalled Onsager's comment about the possibility of  $hc/2e$ . In this way, they found agreement with  $hc/2e$  within about 20%.

This was the situation in the middle of June 1961, where both experimental groups, represented by Martin Näbauer (Herrsching) and Bill Little (Stanford) intended to attend the IBM conference in Yorktown Heights. Bill Little had taken the task, besides presenting an own talk, to show the data points of Deaver and Fairbank, which he had received only a few hours before he left for the conference.

**The IBM conference 1961.** The *IBM Conference of Fundamental Research in Superconductivity*, took place in Yorktown Heights, New York, in June 1961. The conference was part of the dedication ceremonies for the new Thomas J. Watson Research Laboratory. At the IBM conference

Martin Näbauer had prepared a talk entitled "*Experiments on the quantization of magnetic flux in Superconductors*". Näbauer recalled [11], that on the evening before his presentation, Prof. Little visited him in the hotel and made inquiries about both the experimental apparatus and the results, which Näbauer readily provided in all details. The following dialogue is reported by Robert Doll: Little: "*Is the flux quantized?*" ("*Ist der Fluss quantisiert?*"). Näbauer: "*Sure!*" ("*Ja freilich ist er quantisiert!*"). On June 15, Näbauer presented his talk, followed by Bill Little's contribution "*Kapitza resistance of metals in the normal and superconducting states*". During the discussion of the latter, Bill Little showed the data of Deaver and Fairbank.

Bill Little recalled [12], that prior to the beginning of the IBM conference, he had a lively discussion with Brian Pippard over drinks. On this occasion, he showed to him Deaver's and Fairbank's results. Pippard was adamant, that the experiments were *wrong* and that he could prove this fact using a gauge-invariance argument. On June 15, Näbauer presented his and Doll's data on the flux quantization and Little presented the data of Deaver and Fairbank. A heated discussion developed which culminated in the conviction that the factor  $k = 2$  is ultimately needed, in order to understand *both* of the experimental results. Immediately after these presentations, according to Little, Phil Anderson spoke up and claimed, that the factor of  $k = 2$  was an *obvious consequence of the BCS pairing hypothesis*. Brian Pippard did not rebut further.

It became immediately clear to Näbauer, that the submission of the PRL paper was overdue. So he wrote a telegram back to Herrsching, asking what was going on with the paper. Clearly, the time delay was due to a series of discussions still going on between Doll and Meißner about Meißner's co-authorship. When Näbauer's telegram arrived, however, Meißner eventually had the capacity to understand, that his co-authorship was not such a good idea and the paper was submitted to PRL on June 19, 1961. Three days earlier, on June 16, Deaver and Fairbank had submitted their paper to PRL. The long and short of it, the paper by Doll and Näbauer appeared in the same volume of PRL as that of Deaver and Fairbank.

Bill Little recalled, that neither Deaver and Fairbank nor he knew anything about Robert Doll's and Martin Näbauer's activities before the IBM conference. "*It came as a big surprise and some relief that both parties had recognized the factor of two.*" Bascom Deaver commented the "2e" problem as follows: "*However obvious this last point seems now, it was surprisingly difficult to understand at that time*".

**Post-1961.** In 1962 Doll and Näbauer received Awards of both the Bavarian Academy of Sciences as well as the Academy of Sciences in Göttingen for the discovery of the fluxoid quantization. In the same year, Martin Näbauer passed away completely unexpectedly on September 10. In 1986, the Award "Bene Merenti" in silver was given to Robert Doll for his "*Contribution to the experimental discovery of the quantum nature of the magnetic flux in superconductors*" upon the "Solemn Annual Meeting" of the Bavarian Academy by its President Prof. Arnulf Schlüter.

Being known already all over the world for his quantum flux experiment, Bascom Deaver began his career as a Professor at the University of Virginia (UVA) in the year 1965. There he continued his basic research on superconductivity, and went on to explore its applications. He and his students did significant research on flux quantization and developed superconducting magnetometers, which have had important applications. As a whole, Bascom Deaver's research has spanned the entire range from most basic physics to practical applications. For more than 40 years, on the teaching side of his University activities, Deaver was responsible for a tremendous success of the undergraduate program at UVA for which he has worked tirelessly to ensure that it became first rate.



**Figure 1:** Recent portraits of Bascom S. Deaver Jr. (left) and Robert Doll.

In 1967 the *Commission of Low Temperature Research* moved from Herrsching into a new building on the University campus in Garching (about 20 km north of Munich), which was renamed *Walther–Meissner–Institut* (WMI) in 1982. Robert Doll worked there until his retirement as an Academic Director. His name does not only stand for experimental skills, but also for the development of numerous technical high precision devices, in which he took part significantly. These include the valve-free expansion reciprocating engine for the pre-cooling of helium prior to liquefaction and the maintenance-free submerged rotary pump for the filling of liquefied helium into the transport dewars.

Robert Doll retired in the year 1988. He decided to stay at the WMI though as a permanent guest, dealing with tasks requiring precision engineering via optics and interferometry, with problems in astrophysics and even theoretical physics. His strong affinity to the mathematical and esthetic beauty of the Ginzburg–Landau theory could be given proof of in a publication, which was written on the occasion of Vitaly Ginzburg’s 90th birthday, in which he used it for a comprehensive analysis of his experimental data on fluxoid quantization [13].

On November 15, 1974, Walther Meißner died at the age of 91 in Munich. 15 years later, on October 1, 1989 William M. Fairbank suffered a heart attack during his daily jogging in Palo Alto and died at the age of 72.

On January 16, 2008, Robert Doll could celebrate his 85th birthday in the best of health. On this occasion, an article of appreciation was written for the *Journal of the Bavarian Academy of Sciences* by two of his friends [14]. In May 2010 Bascom Deaver officially retired and became professor emeritus. He continued though to have his office and research lab and can be found at the department regularly working on various projects. Bascom Deaver could celebrate his 80th birthday on August 16, 2010 in the best of health.

**Summary.** We have provided a short historical review of the discovery of the fluxoid quantization by Doll/Näbauer in Bavaria and Deaver/Fairbank in California. A remarkable coincidence turned out to exist with respect to a couple of completely nontrivial ingredients for the success of both groups. These were the basic idea, which could be traced back to London's footnote in ref. [5], the starting time around 1959 – 1960, the duration of the experiments from the construction to the final answers in the first half of 1961, the conference on Superconductivity, where the two groups presented their results and finally, the Physics Journal (*The Physical Review Letters*) where the respective results were eventually brought to the attention of the world-wide physics community.

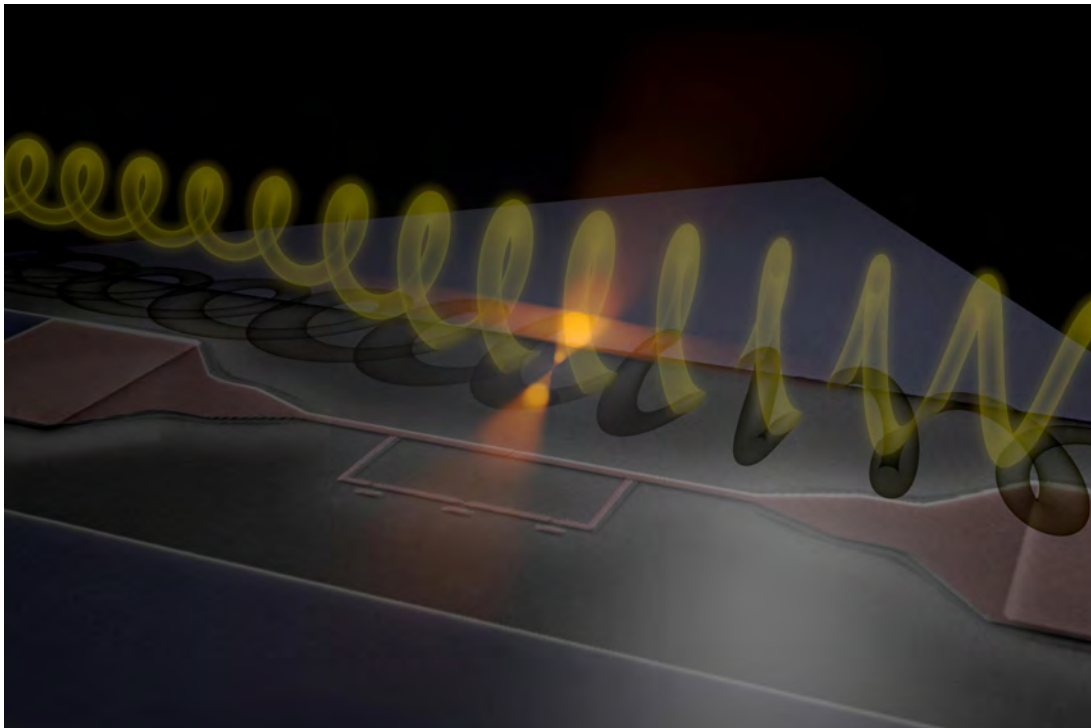
It is an exceptional fact in the history of science, that an important discovery is made independently by two experimental groups, which worked at fairly remote places, but came to the same conclusion almost at the same time namely that (i) the fluxoid is quantized and (ii) the fluxoid quantum is  $\Phi_0 = hc/2e$ . The discovery of quantized flux is often cited, however sometimes by omitting the Doll–Näbauer experiment on the American and the Deaver–Fairbank experiment on the European side. Given the importance of this discovery and the courage and ingenuity of the experimentalists, we believe that both parties deserve the same credit for their work and should always be cited together.

The impact of the fluxoid quantization is seen to largely exceed the mere fundamental understanding of superconductivity. It nowadays lies most notably in the high precision measuring technique and the information technique. Superconducting quantum interferometers, for example, can detect magnetic fields, which are by a factor of  $10^{-11}$  smaller than the earth's magnetic field. Application areas include medicine technique, minimally invasive material testing, sensors in geo-prospection and quantum information processing, to name only a few. What should remain at the end of this article, is the awareness, that the fluxoid quantization in its significance as a quantum phenomenon, seen on a macroscopic scale, detected for the first time fifty years ago, can be added, together with its theoretical interpretation, to the set of most exciting discoveries of the last century.

## References

- [1] H. Kamerlingh-Onnes, *Comm. Phys. Lab. Univ. Leiden*, Nos. 122 and 124 (1911).
- [2] R. Doll and M. Näbauer, *Phys. Rev. Lett.* **7**, 51 (1961).
- [3] R. Doll and M. Näbauer, *Z. Phys.* **169**, 526 (1962).
- [4] B. S. Deaver and W. M. Fairbank, *Phys. Rev. Lett.* **7**, 43 (1961).
- [5] F. London, *Superfluids*, page 152 (Wiley, New York, 1950).
- [6] J. Bardeen, L. N. Cooper, and J. R. Schrieffer, *Phys. Rev.* **108**, 1175 (1957).
- [7] H. Rogalla and P. Kes (eds.) *100 Years of Superconductivity* (Chapman & Hall, 2011).
- [8] D. Einzel, to be published in *J. Low Temp. Phys.*
- [9] R. Groß and D. Einzel, *Akademie Aktuell* 02/2009, page 47.
- [10] B. S. Deaver, in J. D. Fairbank, B. S. Deaver, C. W. F. Everitt, and P. F. Michelson (eds.) *Near Zero – New Frontiers in Physics*, pages 260–311 (W. H. Freeman and Co., New York, 1988).
- [11] G. Möllenstedt, *Physikalische Blätter* **43**, 60 (1987).
- [12] W. A. Little, private communication (2008).
- [13] R. Doll and D. Einzel, *J. Supercond. Nov. Magn.* **19**, 173.
- [14] D. Einzel and R. Hackl, *Akademie Aktuell* 01/2008, page 44.

# Basic Research



An artist's view of the interaction between a superconducting flux qubit incorporated into a stripline resonator with a microwave photon.



## From Strong to Ultrastrong Coupling in Circuit Quantum Electrodynamics

*F. Deppe, T. Niemczyk, E. P. Menzel, A. Marx, R. Gross*<sup>1,2</sup>

In circuit quantum electrodynamics (QED) [1], superconducting thin film circuits are used to investigate the light-matter interaction at the quantum level in the spirit of quantum-optical cavity QED. More specifically, superconducting quantum bit (qubit) circuits act as artificial two-level atoms and microwave resonator circuits can be viewed as quasi-1D “photon boxes”. In the recent years, this “quantum optics on a chip” has generated exciting studies of fundamental quantum mechanics as well as promising results for quantum information processing applications. There are two key figures of merit: the rate  $\Gamma$  at which uncontrolled interactions with the environment destroy quantum coherence and the interaction strength  $g$  between two quantum circuits. Although due to the influence of the solid-state environment  $\Gamma/2\pi$  is typically in the range of 1 MHz–1 GHz, the macroscopic nature of quantum circuits also makes  $g$  several orders of magnitude larger than in cavity QED. In this way, the strong coupling limit  $g > \Gamma$  has been successfully realized in many experiments. The question arising now is: Can we make  $g$  large not only with respect to  $\Gamma$ , but also with respect to the relevant transition frequency  $\omega$  of a circuit QED system? And what will happen then? The first step towards answering this question is to increase  $g$  such that it becomes a significant fraction of  $\omega$ . In this ultrastrong coupling regime [2] regime, ultrafast quantum gates and novel light-matter dynamics can be envisioned.

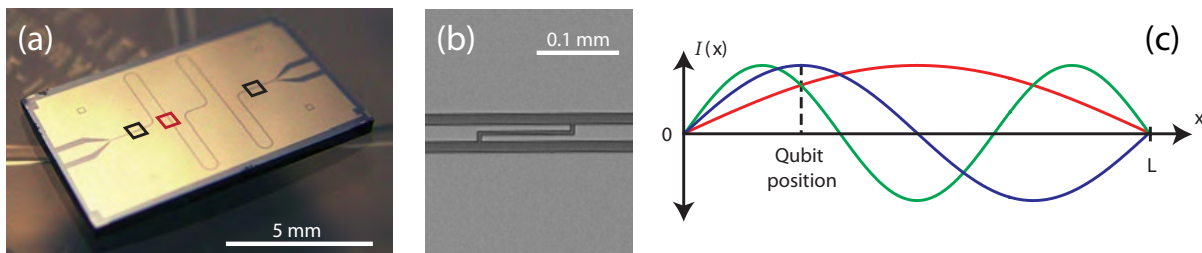


**Figure 1:** Niobium coplanar waveguide resonator for circuit QED experiments. (a) Resonator sample. Black boxes: positions of the capacitors defining the resonator. Red box: Qubit position [see Fig. 2(a)-(c)]. (b) Scanning electron microscopy (SEM) image of one of the capacitors defining the resonator. (c) Sketch of the resonator modes relevant for our experiments. Red: Fundamental mode. Blue: First harmonic. Green: Second harmonic. Physical resonator length  $L = 23$  mm.

In this report, we present experiments on a superconducting flux qubit [3] coupled to a superconducting coplanar transmission line resonator [4] fabricated on a silicon dioxide (50 nm) coated silicon chip. The resonator layout is shown in Fig. 1: The three lowest mode frequencies are  $\omega_1/2\pi = 2.78$  GHz,  $\omega_2/2\pi = 5.36$  GHz, and  $\omega_3/2\pi = 7.78$  GHz and the decay rates are  $\kappa_{1,2,3} \simeq 0.5 - 1.5$  MHz, corresponding to quality factors  $Q_{1,2,3} \simeq 3000 - 6000$ . At the position indicated in Fig. 1(a) and Fig. 1(c), one or two superconducting flux qubits are fabricated using electron beam lithography and aluminum shadow evaporation [4]. We investigate the three different coupling schemes shown in Figs. 2(a)-(c). In the non-galvanic coupling case, the qubit loop is separated from the resonator and the coupling rates  $g_{1,2,3}/2\pi$  are restricted to a few tens of megahertz for typical qubit loop sizes [see Fig. 2(d)]. Nevertheless, this sam-

<sup>1</sup>We acknowledge financial support from the German Research Foundation through SFB 631 and the German Excellence Initiative via NIM.

<sup>2</sup>In collaboration with E. Solano (Universidad del País Vasco and Ikerbasque Foundation, Bilbao, Spain), J. J. Garcia-Ripoll (Instituto de Física Fundamental, Madrid, Spain), and D. Zueco (Instituto de Ciencia de Materiales de Aragón, CSIC-Universidad de Zaragoza, Zaragoza, Spain).

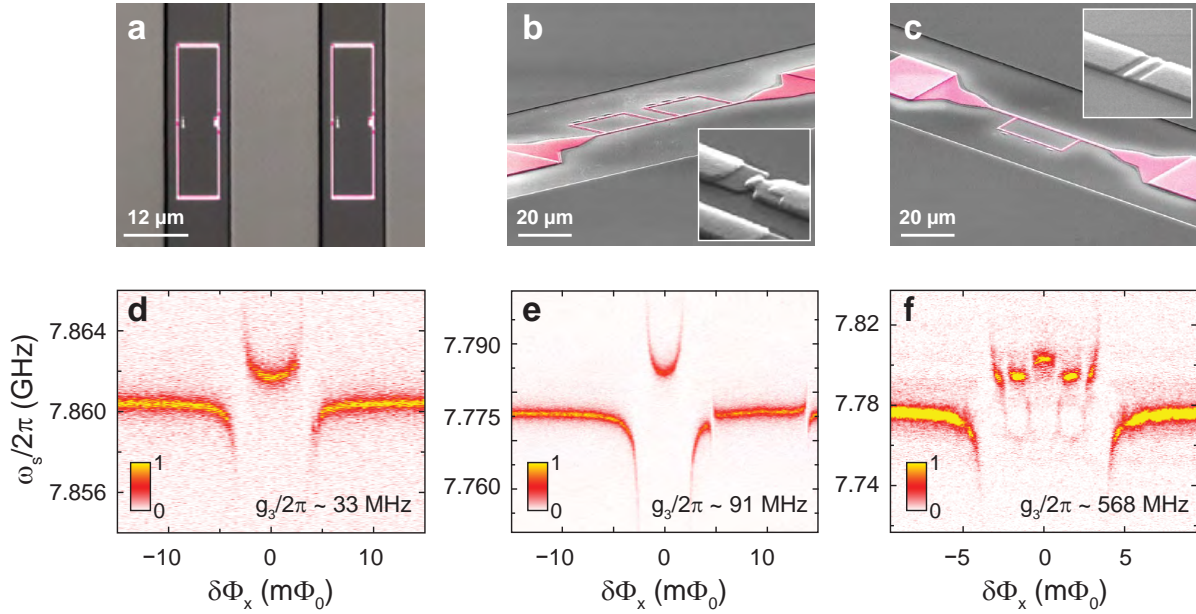


**Figure 2:** Techniques for qubit-resonator coupling and resonator transmission spectra. **(a)** SEM image of a two-qubit nongalvanic coupling sample. **(b)** SEM image of a two-qubit galvanic coupling sample. Inset: typical Josephson junction of our flux qubits (area  $A \sim 0.03 \mu\text{m}^2$ ). **(c)** SEM image of the single flux qubit ultrastrong coupling sample. The mutual inductance is the sum of the geometric inductance (non-galvanic and galvanic; 15 %) and the Josephson inductance of the coupling junction in the shared segment (85 %). Inset: coupling junction with area  $7A$ . **(d)**, **(e)**, **(f)** Resonator transmission magnitude (color code) near the second harmonic as a function of the excitation frequency and the qubit flux for the samples shown in **(a)**, **(b)**, **(c)**, respectively. The excitation power corresponds to an average photon number  $n_3 < 1$  in the resonator mode.

ple already fulfills the strong coupling condition. Second, for galvanic coupling, qubit and resonator share a thin segment as shown in Fig. 2(b). In this case, despite of a smaller qubit loop, the coupling is enhanced by the kinetic inductance of the narrow line segment shared by the resonator and the qubit loop [see Fig. 2(e)]. Third, the coupling can further be significantly increased by the Josephson inductance of a junction inserted into the shared segment as shown in Fig. 2(c). In this way,  $g_3$  is increased by a factor of 6, yielding  $g_3/\omega_3 = 7\%$ . [see Fig. 2(f)]. For the fundamental and first harmonic mode, we even obtain  $g_1/\omega_1 = 11\%$  and  $g_2/\omega_2 = 12\%$ , respectively [2]. These values imply that we have reached, for the first time with superconducting circuits, the ultrastrong coupling regime. In addition to the coupling strengths, we determine the tunneling matrix element  $\Delta$  and the persistent current  $I_p$  of the qubit from the transmission spectra of Figs. 2(d)-(f). The extracted parameters are  $\Delta/h = 5.81$  GHz and  $I_p = 271$  nA for the non-galvanic,  $\Delta/h = 6.88$  GHz and  $I_p = 266$  nA for the galvanic, and  $\Delta/h = 2.25$  GHz and  $I_p = 315$  nA for the ultrastrong coupling sample.

In conclusion, we have realized strong coupling between a flux qubit and a coplanar waveguide resonator using non-galvanic, galvanic, and Josephson junction mediated coupling schemes. The latter enabled us to reach the ultrastrong coupling regime, where the coupling constant becomes a significant fraction of the qubit and resonator transition frequencies. Hence, our system is a promising testbed for ultrafast quantum information processing and ultrastrong light-matter interaction.

## References

- [1] A. Wallraff, D. I. Schuster, A. Blais, L. Frunzio, R.-S. Huang, J. Majer, S. Kumar, S. M. Girvin, and R. J. Schoelkopf, *Nature* **431**, 162 (2004).

- 
- [2] T. Niemczyk, F. Deppe, H. Huebl, E. P. Menzel, F. Hocke, M. J. Schwarz, J. J. Garcia-Ripoll, D. Zueco, T. HÃijmer, E. Solano, A. Marx, and R. Gross, *Nature Phys.* **6**, 772 (2010).
- [3] J. E. Mooij, T. P. Orlando, L. Levitov, L. Tian, C. H. van der Wal, and S. Lloyd, *Science* **285**, 1036 (1999).
- [4] T. Niemczyk, F. Deppe, M. Mariani, E. P. Menzel, E. Hoffmann, G. Wild, L. Eggenstein, A. Marx, and R. Gross, *Supercond. Sci. Technol.* **22**, 034009 (2009).

## Dual-Path State Reconstruction Scheme for Propagating Quantum Microwaves and Detector Noise Tomography

*E. P. Menzel, F. Deppe, M. Mariani, A. Baust, M. Á. Araque Caballero, E. Hoffmann, T. Niemczyk, C. Probst, K. Neumaier, K. Uhlig, A. Marx, E. Solano,<sup>1</sup> and R. Gross<sup>2</sup>*

With the advent of circuit quantum electrodynamics (QED) [1], superconducting quantum circuits have enabled exciting studies of the quantum nature of microwave light confined in resonators acting as “photon boxes” [2]. Propagating quantum microwaves, despite of their potential use in the toolbox of “quantum optics on a chip”, have received attention only recently [3–7]. In particular, the efficient coupling of superconducting qubits to open transmission lines has been demonstrated [6, 7]. Driven by the resulting perspective of quantum information processing with propagating microwaves in the spirit of all-optical quantum computing [8], we have developed a novel state reconstruction method. In this method the signal is split into two amplification and detection chains based on off-the-shelf cryogenic linear amplifiers and then detected using signal recovery techniques. We showed that by this dual-path method access to arbitrary moments of both weak propagating quantum microwaves and the detector noise is obtained [3].

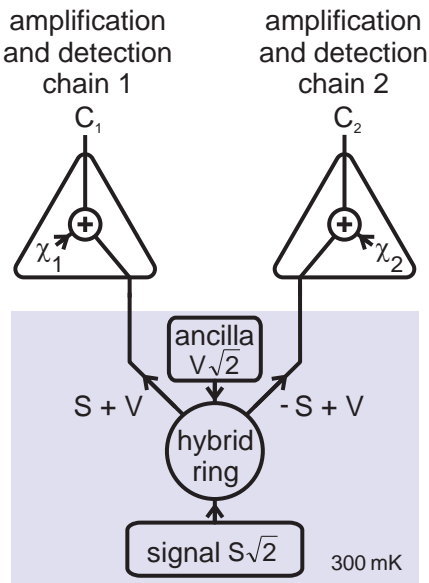


**Figure 1:** Diagram of the dual-path setup for the tomography of quantum microwaves. The beam splitter is a hybrid ring or a Wilkinson power divider. For a full tomography of arbitrary states at the quantum level, the ancilla state  $V$  (typically the vacuum) incident at the fourth port of the beam splitter must be known.  $\chi_{1,2}$  are the (uncorrelated) noise contributions from the two amplification chains.

amplification chain was used, whereas in Fig. 2(d) the dual-path scheme has been applied based on the same dataset, however, using both chains’ data. Comparing Fig. 2(c) and (d) the

The principle of the dual-path method is sketched in Fig. 1. We first split the signal into two amplification and detection chains, down-convert the amplified fields from the GHz- to the MHz-regime by mixers, and then measured them with a 400 MS/s 12-bit A/D-converter card. Details of the amplification and detection chains can be found in Ref. [3]. By calculating suitable correlations of the two outputs, our method allows for quantum state reconstruction despite the presence of significant amplifier noise. To validate our dual-path method we performed proof-of-principle experiments with statistical mixtures of weak pulsed coherent microwaves. Using cryogenic HEMT amplifiers, which add 10–20 noise photons on average (POA), we demonstrate sufficient sensitivity for recovering the first two moments [see Fig. 2(a)] of signals at a power level of 1–2 POA. The resolution limit of the third central moment is currently 10–20 POA [see Fig. 2(b)]. In Figs. 2(c) and (d) we show the third central moment, which is a measure of the asymmetry of a histogram. The brown curves are the result of a statistical mixture of phase shifted signals with an equally distributed histogram, where the third central moment is flat. Skewing the histogram by shifting one fourth of the pulses to the left and the rest to the right results in an oscillating third central moment signal (green curves). For the curves in Fig. 2(c) only one

<sup>1</sup>Universidad del País Vasco and Ikerbasque Foundation, Bilbao, Spain.

<sup>2</sup>We gratefully acknowledge financial support from the German Research Foundation through SFB 631 and the German Excellence Initiative via NIM.

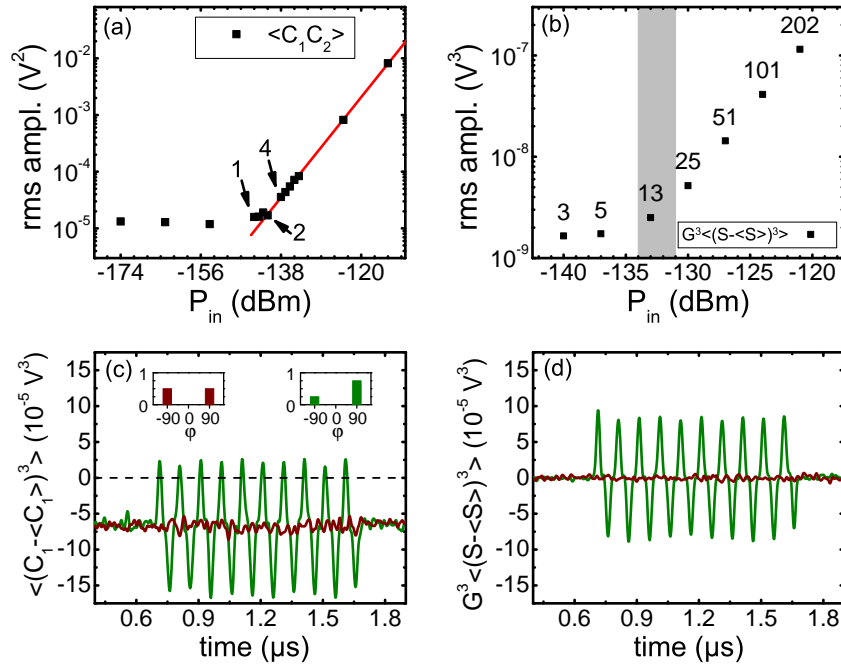


**Figure 2:** Experimental Results. (a) Resolution limit for the second moment probed with 5.85 GHz coherent pulses. The numbers above the arrows indicate the pulse power in POA. (b) Power dependence of the third central moment probed with a suitable classical mixture of phase-shifted pulses. The numbers above the arrows indicate the pulse power in POA. Gray area: detection limit (10–20 POA). (c) Third central moment at 100 POA measured with a single amplification chain. Insets: histograms. (d) Third central moment measured with the dual-path method, data set as in (c). For technical reasons, in (b) a Wilkinson power divider was used instead of the hybrid ring.

advantage of the dual-path scheme is clearly visible: On the one hand the noise in the curves is reduced and on the other hand an offset of the third central moment in the case of a single chain is suppressed by the dual-path method. This offset can be identified as the third central moment of the detector noise, indicating a non-Gaussian statistics [3].

In conclusion, our results show that the dual-path method is a suitable tool for characterizing propagating quantum signals such as squeezed states from a Josephson parametric amplifier, Fock states leaking out of an on-chip resonator, or nonclassical microwave field states generated in a two-resonator circuit QED setup.

## References

- [1] A. Wallraff, D. I. Schuster, A. Blais, L. Frunzio, R.-S. Huang, J. Majer, S. Kumar, S. M. Girvin, and R. J. Schoelkopf, *Nature* **431**, 162 (2004).
- [2] M. Hofheinz, H. Wang, M. Ansmann, R. C. Bialczak, E. Lucero, M. Neeley, A. D. O’Connell, D. Sank, J. Wenner, J. M. Martinis, and A. N. Cleland, *Nature* **459**, 546 (2009).
- [3] E. P. Menzel, F. Deppe, M. Mariani, M. A. Araque Caballero, A. Baust, T. Niemczyk, E. Hoffmann, A. Marx, E. Solano, and R. Gross, *Phys. Rev. Lett.* **105**, 100401 (2010).
- [4] M. Mariani, E. P. Menzel, F. Deppe, M. A. Araque Caballero, A. Baust, T. Niemczyk, E. Hoffmann, E. Solano, A. Marx, and R. Gross, *Phys. Rev. Lett.* **105**, 133601 (2010).
- [5] D. Bozyigit, C. Lang, L. Steffen, J. M. Fink, M. Baur, R. Bianchetti, P. J. Leek, S. Filipp, M. P. da Silva, A. Blais, and A. Wallraff, *arXiv:1002.3738* (2010).
- [6] O. Astafiev, A. M. Zagoskin, A. A. Abdumalikov, Y. A. Pashkin, T. Yamamoto, K. Inomata, Y. Nakamura, and J. S. Tsai, *Science* **327**, 840 (2010).
- [7] Y.-F. Chen, D. Hover, S. Sendelbach, L. Maurer, S. Merkel, E. Pritchett, F. Wilhelm, and R. McDermott, *arXiv:1011.4329* (2010).
- [8] J. L. O’Brien, *Science* **318**, 1567 (2007).

## Characterization of a Flux-Driven Josephson Parametric Amplifier

A. Baust, E. P. Menzel, T. Niemczyk, E. Hoffmann, M. Häberlein, F. Deppe, A. Marx, R. Gross<sup>1</sup>  
K. Inomata,<sup>2</sup> T. Yamamoto, Y. Nakamura<sup>3</sup>

The reconstruction of the Wigner function of weak quantum microwave states is a fundamental challenge in the field of circuit QED. Detectors with single photon resolution do not exist in the microwave regime and the commonly used linear, phase-insensitive HEMT amplifiers inevitably add noise to the signal that may be considerably larger than the signal itself. One approach to the reconstruction of, in principle, all statistical moments and hence the Wigner function of propagating microwave signals is the dual-path scheme introduced by E. P. Menzel *et al.* [1]. This method has already been successfully demonstrated for statistical mixtures of coherent states [1] and weak thermal states [2]. The next challenge is to prove that the dual-path scheme is also capable of reconstructing non-classical signals. The signal of choice is a squeezed state, i.e. a quantum state where the uncertainty is increased in one signal quadrature and reduced in the other. Such states can be generated using linear, phase-sensitive amplifiers. In our work, a flux-driven Josephson parametric amplifier (JPA) designed by T. Yamamoto *et al.* [3] was studied [4].

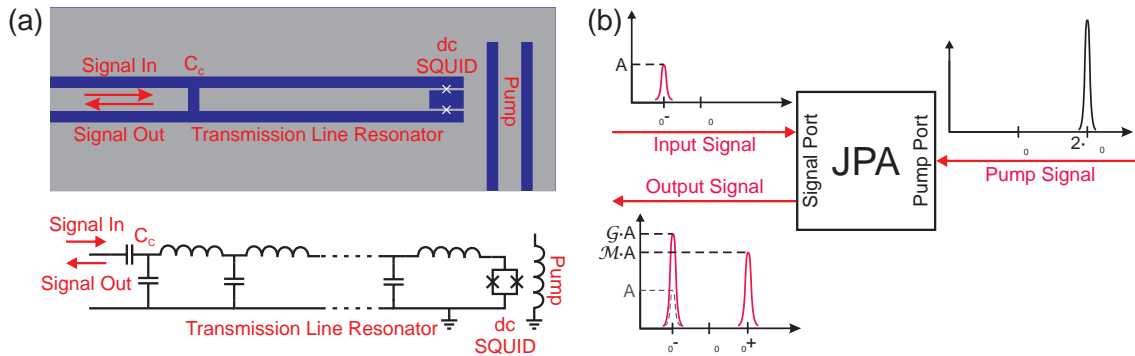


**Figure 1:** (a) Sample layout (top figure) and circuit diagram (bottom figure) of a flux-driven Josephson parametric amplifier. A magnetic flux  $\Phi$  is applied to the SQUID loop via the pump line thereby modulating the resonant frequency of the transmission line resonator. The output signal of the JPA is detected at the same port where the input signal is applied. (b) Working principle of a JPA. The schematic shows the process of idler mode generation and signal mode amplification by means of a pump signal.

The operating principle of a JPA is analogue to a playground swing, where the deflection amplitude is amplified by modulating the swing length at twice the oscillation frequency. In the case of the JPA, the oscillating system is the circuit analogue of the mechanical pendulum, namely a microwave resonator. The resonant frequency of such a resonator is determined by its capacitance and inductance. The latter can be varied by a superconducting quantum interference device (SQUID) consisting of a superconducting loop intersected by two Josephson junctions. The SQUID terminates the center conductor of the resonator to ground, thereby adding a flux-dependent nonlinear inductance to the resonator, cf. Fig. 1(a). Applying a dc flux signal to the SQUID allows to adjust the resonant frequency  $\omega_0$  to the desired operation point, whereas an additional ac flux (pump signal) results in a periodic modulation of the resonant frequency. At a pump frequency  $2\omega_0$  the microwave signal coupled into the resonator is amplified. If an input signal at frequency  $\omega_0 - \omega$  is applied to the signal port of the JPA,

<sup>1</sup>This work is supported by the German Research Foundation through SFB 631 and the German Excellence Initiative via NIM.

<sup>2</sup>RIKEN, Wako, Japan

<sup>3</sup>NEC Corporation Tsukuba and RIKEN, Wako, Japan

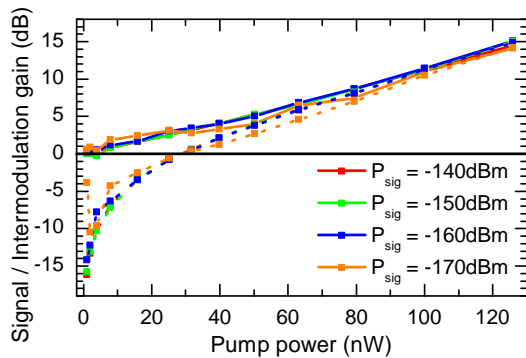


**Figure 2:** Signal gain (solid line) and intermodulation gain (dotted line) at a resonant frequency of 5.639 GHz. For large gains, signal and intermodulation gain converge as predicted by theory.

over at least three orders of magnitude. In order to determine the bandwidth of the amplifier, we measured the gain for different input signal frequencies around 5.639 GHz and a fixed pump frequency. For a pump power of -39 dBm, we found a 3-dB bandwidth of 3.13 MHz. Reducing the pump power by 3 dB increases the bandwidth to 6.34 MHz, but in turn reduces the gain by a factor of 5.7. Hence, in order to maximize the gain-bandwidth product of the JPA, a quantity relevant for the amplification of broadband signals, one would rather aim for higher gain instead of higher bandwidth as the decreasing gain is not fully compensated by the increasing bandwidth.

An important special case arises when the input signal frequency matches half the pump frequency, the so-called *degenerate-mode operation* of the JPA. Here, the idler mode is generated at the input signal frequency and will therefore interfere with the signal mode. As shown in Fig. 3, this *degenerate gain* depends on the phase of the pump signal. For a pump power of -39 dBm, we observed a maximum degenerate gain of 20.7 dB.

In conclusion, we showed that our JPA sample is performing very well. The large available gain suggests that squeezed states with a high degree of squeezing can be generated. A highly interesting application is to squeeze the vacuum and to reconstruct this squeezed state by our dual-path scheme.

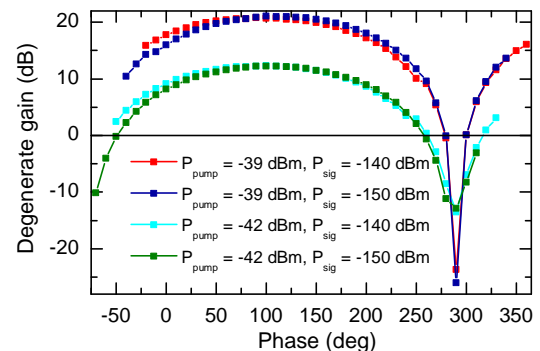


**Figure 3:** Phase-dependent gain at a resonant frequency of 5.639 GHz for different input signal and pump power levels.

## References

- [1] E. P. Menzel, F. Deppe, M. Mariantoni, M. A. Araque Caballero, A. Baust, T. Niemczyk, E. Hoffmann, A. Marx, E. Solano, and R. Gross, *Phys. Rev. Lett.* **105**, 100401 (2010).
- [2] M. Mariantoni, E. P. Menzel, F. Deppe, M. A. Araque Caballero, A. Baust, T. Niemczyk, E. Hoffmann, E. Solano, A. Marx, and R. Gross, *Phys. Rev. Lett.* **105**, 133601 (2010).
- [3] T. Yamamoto, K. Inomata, M. Watanabe, K. Matsuba, T. Miyazaki, W. D. Oliver, Y. Nakamura, and J. S. Tsai, *Appl. Phys. Lett.* **93**, 042510 (2008).
- [4] A. Baust, *Characterization of Flux-driven Josephson Parametric Amplifiers*, Diploma thesis, Technische Universität München (2010).
- [5] B. Yurke, L. R. Corruccini, P. G. Kaminsky, L. W. Rupp, A. D. Smith, A. H. Silver, R. W. Simon, and E. A. Whittaker, *Phys. Rev. A* **39**, 2519 (1989).

## Ultrastrong Coupling in Circuit Quantum Electrodynamics

T. Niemczyk, F. Deppe, H. Huebl, E. Menzel, M. Schwarz, F. Hocke, E. Hoffmann, A. Marx, R. Gross<sup>1</sup>

J.J. Garcia-Ripoll<sup>2</sup>, D. Zueco<sup>3</sup>, T. Hümmer<sup>4</sup>, E. Solano<sup>5</sup>

Circuit quantum electrodynamics (QED) studies the interaction of superconducting artificial atoms coupled to on-chip cavities. This relatively new field of research has gained a lot of momentum since the *strong coupling limit* could be accessed experimentally [1]. In this regime, the artificial solid state atom and the cavity can coherently exchange a photon frequently before coherence is lost. The dynamics of the coupled system is well described by the renowned Jaynes-Cummings model. However, this model is no longer appropriate when the ultrastrong limit of light-matter coupling is reached [2]. Here, we report on the first experimental realization of a circuit QED system operating in the ultrastrong coupling limit [3]. To this end, we use the large nonlinear inductance of a Josephson junction (JJ) shared between a flux qubit and a coplanar waveguide resonator. In the novel and yet unexplored regime of ultrastrong light-matter interaction, the atom-photon coupling rate  $g$  reaches a considerable fraction of the relevant system's transition frequencies. Therefore, the transmission spectra of the combined system reveal direct evidence for the breakdown of the Jaynes-Cummings (JC) model.

Images of our superconducting quantum circuit are shown in Fig. 1. At a current antinode for the  $\lambda$ -mode of a niobium superconducting resonator (see Fig. 1a and b), a small part of the center conductor is replaced with a narrow aluminum strip interrupted by a large-area JJ. The Josephson inductance of this junction mediates most of the inductive coupling between a superconducting 3-JJ-flux qubit which galvanically connected to the strip (see Fig. 1c). The flux qubit consists of three nanometer-scaled JJs interrupting a superconducting loop, which is threaded by an external flux bias  $\Phi_x$ . Scanning electron microscope (SEM) images of the qubit loop and the JJs are shown in Fig. 1c–e.

For suitable junction sizes, the qubit potential landscape can be reduced to a double-well potential, where the two minima correspond to states with clockwise and counter-clockwise persistent currents  $|\pm I_p\rangle$ . At  $\delta\Phi_x = 0$ , these two states are degenerate and separated by an energy gap  $\Delta$ . Here,  $\delta\Phi_x = \Phi_x \pm k\Phi_0/2$  is the relative qubit flux bias and  $k \in \mathbb{Z} \setminus \{0\}$ . In the qubit eigenbasis, the qubit Hamiltonian reads  $\hat{H}_q = \hbar\omega_q\hat{\sigma}_z/2$ . Here,  $\omega_q = \sqrt{\Delta^2 + (2I_p \cdot \delta\Phi_x)^2}/\hbar$  is the qubit transition frequency which can be adjusted by  $\delta\Phi_x$ . The resonator modes are described as harmonic oscillators,  $\hat{H}_n = \hbar\omega_n(\hat{a}_n^\dagger\hat{a}_n + 1/2)$ , where  $\omega_n$  is the resonance frequency and  $n$  is the resonator mode index. The operator  $\hat{a}_n^\dagger$  ( $\hat{a}_n$ ) creates (annihilates) a photon in the  $n^{\text{th}}$  resonator mode<sup>6</sup>.

The Hamiltonian of the quantum circuit can be written as

$$\hat{H} = \hat{H}_q + \sum_n \left[ \hat{H}_n + \hbar g_n \left( \hat{a}_n^\dagger + \hat{a}_n \right) \left( \cos \theta \hat{\sigma}_z - \sin \theta \hat{\sigma}_x \right) \right], \quad (1)$$

<sup>1</sup>We acknowledge financial support by the German Research Foundation through SFB 631 and the German Excellence Initiative through NIM.

<sup>2</sup>Instituto de Física Fundamental, CSIC, Madrid, Spain

<sup>3</sup>Instituto de Ciencia de Materiales de Aragón, CSIC-Universidad de Zaragoza, Zaragoza, Spain

<sup>4</sup>Institut für Physik, Universität Augsburg, Augsburg, Germany

<sup>5</sup>Departamento de Química Física, Universidad del País Vasco - Euskal Herriko Unibertsitatea and IKER-BASQUE, Basque Foundation for Science, Bilbao, Spain

<sup>6</sup>Throughout this work, we refer to the  $n^{\text{th}}$  mode as the  $n\lambda/2$ -mode

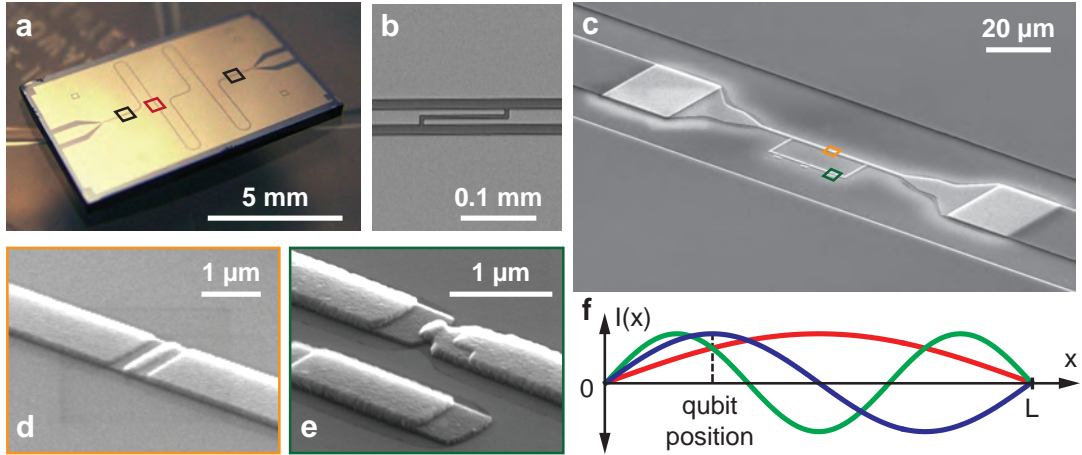


**Figure 1:** Images of the superconducting quantum circuit and sketch of current distribution in the resonator. (a) Optical image of the superconducting  $\lambda/2$  coplanar waveguide resonator. The red and black rectangles mark the position of the qubit and the resonators' coupling capacitors. (b) Scanning electron microscope (SEM) image of one of the coupling capacitors acting as "mirrors" for the quantized electromagnetic field in the resonator. (c) SEM image of the galvanically coupled flux qubit. The width in the overlap regions with the center conductor is  $20\mu\text{m}$ , whereas that of the constriction is only  $1\mu\text{m}$ . The orange and green rectangle mark the positions of coupling and qubit Josephson junctions (JJs), respectively. (d) SEM image of the large JJ shared by resonator and qubit. This JJ mediates most of the inductive coupling between qubit and resonator. (e) SEM image of a regular small JJ embedded in the qubit loop. (f) Sketch of the current distribution of the first three resonator modes. Their resonance frequencies are  $\omega_1/2\pi = 2.782\text{ GHz}$  ( $\lambda/2$ , red),  $\omega_2/2\pi = 5.357\text{ GHz}$  ( $\lambda$ , blue) and  $\omega_3/2\pi = 7.777\text{ GHz}$  ( $3\lambda/2$ , green). The resonator has a length  $L = 23\text{ mm}$  and the qubit is fabricated at a current antinode of the  $\lambda$ -mode.

where  $\hat{\sigma}_{x,z}$  denote Pauli operators,  $g_n$  is the coupling rate of the qubit to the  $n^{\text{th}}$  cavity mode, and the flux dependence is encoded in  $\sin\theta = \Delta/\hbar\omega_q$  and  $\cos\theta$ . The operator  $\hat{\sigma}_x$  is conveniently expressed as sum of the qubit raising ( $\hat{\sigma}_+$ ) and lowering ( $\hat{\sigma}_-$ ) operator. Thus, in contrast to the Jaynes-Cummings model, the Hamiltonian in Eq. (1) explicitly contains counter-rotating terms of the form  $\hat{a}_n^\dagger\hat{\sigma}_+$  and  $\hat{a}_n\hat{\sigma}_-$ .

**Experimental results.** First, we present measurements allowing the extraction of the coupling constants of the qubit to the first three resonator modes. The spectroscopy data in Fig. 2a shows the dressed qubit transition frequency with the expected hyperbolic flux-dependence and a minimum at  $\delta\Phi_x = 0$ . Furthermore, the two lowest resonator modes ( $\omega_1$  and  $\omega_2$ ) are visible. In principle, a fit to the Hamiltonian in Eq. (1) would yield all system parameters. However, our measurement resolution does not allow us to reliably determine all relevant system parameters, in particular the undressed qubit energy gap  $\Delta$  and the coupling constants  $g_n$  in this situation. Instead, we extract them from a cavity transmission spectrum with negligible photon population. For that purpose, we first measure the power-dependent ac-Zeeman shift of the qubit transition frequency at  $\delta\Phi_x = 0$ . The data is shown in the inset of Fig. 2a. The average photon number  $\bar{n}_3$  can be estimated using the relation  $P_{\text{rf}} = \bar{n}_3\hbar\omega_3\kappa_3$ , where  $\kappa_3/2\pi \approx 3.7\text{ MHz}$  is the full width at half maximum of the cavity resonance and  $P_{\text{rf}}$  the probe power referred to the input of the resonator.

Figure 2b shows a color coded transmission spectrum for the  $3\lambda/2$ -mode as a function of  $\delta\Phi_x$ . The data is recorded at an input power  $P_{\text{rf}} \approx -140\text{ dBm}$  (green data point in Fig. 2a, inset) corresponding to  $\bar{n}_3 = 0.18$ . We observe a spectrum with a large number of anticrossings resulting from the multimode structure of our cavity system. To extract the individual coupling constants  $g_n$ , we calculate the lowest nine transition frequencies of the Hamiltonian given by

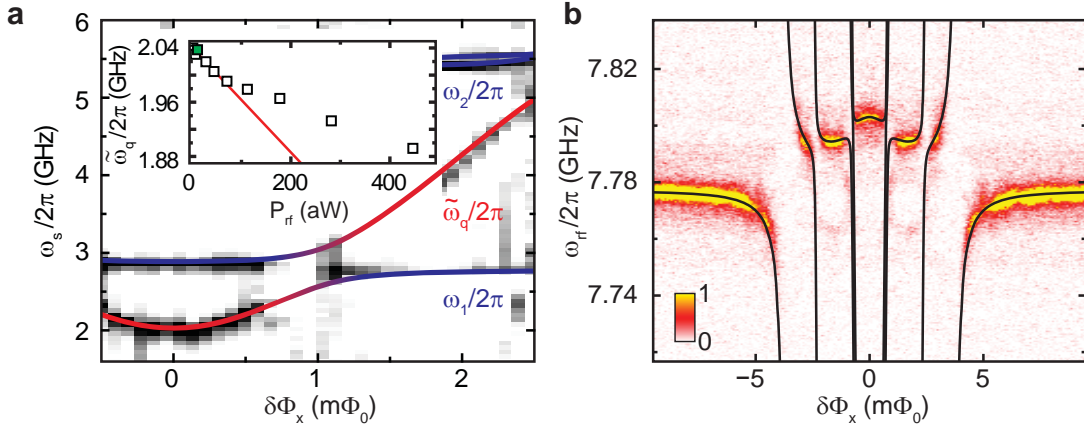


**Figure 2:** Qubit microwave spectroscopy and low power transmission spectra. **(a)** Microwave spectroscopy of the coupled qubit-cavity system. The measured transmission magnitude (color code; black=low; white=high) is plotted as a function of the relative flux bias  $\delta\Phi_x$  and the spectroscopy frequency  $\omega_s/2\pi$ . The colored lines indicate the dressed qubit-like (red) and cavity-like (blue) energy level spectrum of Hamiltonian (1) obtained with the fit parameters from the cavity transmission data in (b). Inset: center frequency of the qubit spectroscopy signal at  $\delta\Phi_x = 0$  as a function of the probe power  $P_{\text{rf}}$ . The green dot indicates the power level at which the spectra in (b). **(b)** Cavity transmission ( $3\lambda/2$ -mode, linear scale, arb. units) as a function of  $\delta\Phi_x$  and probe frequency  $\omega_{\text{rf}}/2\pi$ . The black lines represent a numerical fit of the Hamiltonian (1) to the data.

Eq. (1), taking into account the first three resonator modes. As shown in Fig. 2b, the calculated spectrum is in excellent agreement with the experimental data of the  $3\lambda/2$ -mode. Fitting the data, we obtain  $2I_p = 630$  nA and  $\Delta/h = 2.25$  GHz for the qubit. Note that  $\Delta/h$  deviates significantly from the dressed qubit transition frequency  $\tilde{\omega}_q$  at  $\delta\Phi_x = 0$  (cf. Fig. 2a, inset), providing further evidence for very strong qubit-cavity interaction. Most importantly, we find coupling rates of  $g_1/2\pi = 314$  MHz,  $g_2/2\pi = 636$  MHz, and  $g_3/2\pi = 568$  MHz. These values for  $g_n$  correspond to normalized coupling rates  $g_n/\omega_n$  of remarkable 11.2 %, 11.8 %, and 7.3 %, respectively. These large coupling rates – an order of magnitude larger than the highest value reported so far [4] in a circuit QED architecture – allows us to access the ultrastrong coupling regime.

We now analyze the features in our data which provide unambiguous evidence for the breakdown of the rotating-wave approximation inherent to the Jaynes-Cummings (JC) model. In Fig. 3, we compare the energy level spectrum of the full Hamiltonian in Eq. (1) to that of a three-mode JC model approximation. We note that, depending on  $\delta\Phi_x$ , there are regions where our data can be well described by the JC model (see Fig. 3a). However, there are also regions with significant qualitative deviations between our data and the JC model (see Fig. 3c). For our analysis we use the notation  $|q, N_1, N_2, N_3\rangle = |q\rangle \otimes |N_1\rangle \otimes |N_2\rangle \otimes |N_3\rangle$ , where  $q = \{g, e\}$  denotes the qubit ground or excited state, respectively, and  $|N_n\rangle = \{|0\rangle, |1\rangle, |2\rangle, \dots\}$  represents the Fock-state with photon occupation  $N$  in the  $n^{\text{th}}$  resonator mode. At the outermost anti-crossings (cf. Fig. 3b), where  $\omega_3 \approx \omega_q$ , the eigenstates  $|\psi_{\pm}\rangle$  of the coupled system are in good approximation symmetric and antisymmetric superpositions of the states  $|e, 0, 0, 0\rangle$  and  $|g, 0, 0, 1\rangle$  with the same excitation number (one in the qubit or one in the resonator). Since the coupling of states with the same excitation number is a characteristic of the JC model, here the situation is well described by the JC model prediction. On the contrary, the origin of the anticrossing shown in Fig. 3c is of different nature. Here, the dominant contributions to the eigenstates  $|\psi_{\pm}\rangle$  are about symmetric and antisymmetric superpositions of the degenerate states  $\varphi_1 = |e, 1, 0, 0\rangle$  and  $\varphi_2 = |g, 0, 0, 1\rangle$  with different excitation number. The transition from  $\varphi_1$  to  $\varphi_2$  can be understood as the annihilation of two excitations, one in the  $\lambda/2$ -mode and one in the qubit, while, simultaneously, creating only a single excitation in the

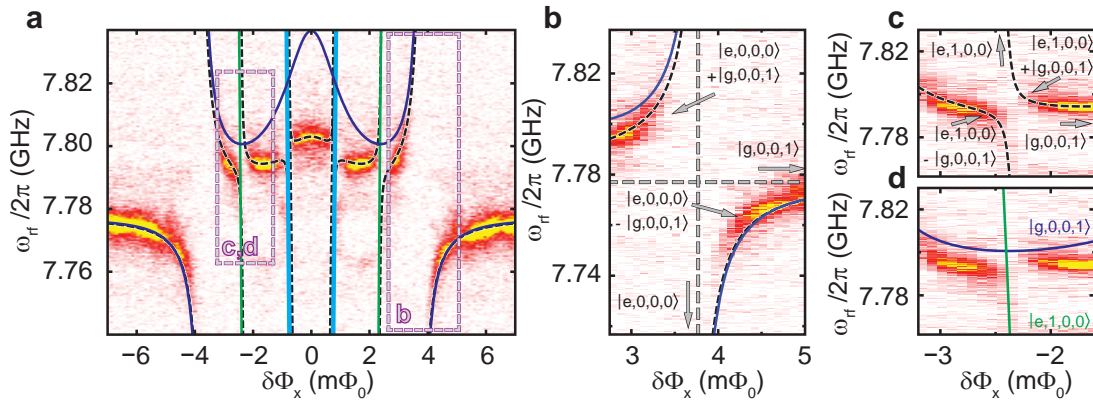


**Figure 3:** Breakdown of the Jaynes-Cummings model. **(a)** Cavity transmission ( $3\lambda/2$ -mode, linear scale, arb. units) as a function of  $\delta\Phi_x$  and probe frequency  $\omega_r/2\pi$ . The black dashed lines in all plots represent the energy level spectrum obtained from the Hamiltonian (1). The colored lines in all plots are the energy level spectrum obtained from the Jaynes-Cummings model (dark blue:  $|g,0,0,1\rangle$ , except for anticrossing region shown in (b); green:  $|e,1,0,0\rangle$ ; light blue:  $|e,0,1,0\rangle$  and  $|e,2,0,0\rangle$ , which are indistinguishable within the resolution of this plot). The grey dashed boxes mark the areas magnified in (b)-(d). **(b)** Single excitation anticrossing. The quantitative deviations of the Jaynes-Cummings model from Eq. (1) are attributed to a small admixture of the state  $|g,1,1,0\rangle$ . The uncoupled states are indicated by dashed grey lines. **(c)** Avoided crossing due to a coupling between the degenerate states  $|g,0,0,1\rangle$  (one excitation) and  $|e,1,0,0\rangle$  (two excitations). This is caused by counterrotating terms in the Hamiltonian (1). Within the framework of the Jaynes-Cummings model, only states with an equal number of excitations can be coupled. **(d)** Same as (c), but for the Jaynes-Cummings model. Within numerical accuracy, no anticrossing is predicted, clearly contradicting the data.

$3\lambda/2$ -mode. Such a process can only result from counter-rotating terms as they are included in the full Hamiltonian (1), but not in the JC approximation. There only eigenstates with an equal number of excitations are coupled. Although counter-rotating terms in principle exist in any real circuit QED system, their effect becomes prominent only in the ultrastrong coupling limit with large normalized couplings  $g_n/\omega_n$  as realized in our system. Hence, the observed anticrossing shown in Fig. 3c is a direct experimental manifestation of physics beyond the rotating-wave approximation in the JC model. As shown in Fig. 3d, the latter would imply a crossing of the involved energy levels, which is not observed.

**Summary.** We have performed measurements on a superconducting circuit QED system in the ultrastrong-coupling regime. Our transmission spectra are in excellent agreement with theoretical predictions and show clear evidence for physics beyond the JC model. Our system can act as an on-chip prototype for unveiling the physics of ultrastrong light-matter interaction. Future explorations may include squeezing, causality effects in quantum field theory, the generation of bound states of qubits and photons, in situ switching of distinct physical regimes, and ultrafast quantum operations in circuit QED for quantum information protocols.

## References

- [1] A. Wallraff, D. I. Schuster, A. Blais, L. Frunzio, R.-S. Huang, J. Majer, S. Kumar, S. M. Girvin, and R. J. Schoelkopf, *Nature* **431**, 162 (2004).
- [2] J. Bourassa, J. M. Gambetta, A. A. Abdumalikov, O. Astafiev, Y. Nakamura, and A. Blais, *Phys. Rev. A* **80**, 032109 (2009).
- [3] T. Niemczyk, F. Deppe, H. Huebl, E. P. Menzel, F. Hocke, M. J. Schwarz, J. J. Garcia-Ripoll, D. Zueco, T. Hümmer, E. Solano, A. Marx, and R. Gross, *Nature Phys.* **6**, 772 (2010).
- [4] L. Bishop, J. Chow, J. Koch, A. Houck, M.H.Devoret, E. Thuneberg, S. Girvin, and R. Schoelkopf, *Nature Phys.* **5**, 105 (2008).

# Response and Transport in Non–Centrosymmetric Superconductors

*D. Einzel*

*L. Klam, D. Manske*<sup>1</sup>

**Abstract.** We formulate a kinetic theory for non–centrosymmetric superconductors at low temperatures in the clean limit. The transport equations are solved quite generally in spin– and particle–hole (Nambu) space by performing first a transformation into the band basis and second a Bogoliubov transformation to the quasiparticle–quasihole phase space. Our result is a particle–hole–symmetric, gauge–invariant and charge conserving description, which is valid in the whole quasiclassical regime ( $|\mathbf{q}| \ll k_F$  and  $\hbar\omega \ll E_F$ ). We calculate the current response, the specific heat capacity, and the Raman response function. For the Raman case, we investigate within this framework the polarization–dependence of the electronic (pair–breaking) Raman response for the recently discovered non–centrosymmetric superconductors at zero temperature. Possible applications include the systems CePt<sub>3</sub>Si and Li<sub>2</sub>Pd<sub>x</sub>Pt<sub>3–x</sub>B, which reflect the two important classes of the involved spin–orbit coupling. We provide analytical expressions for the Raman vertices for these two classes and calculate the polarization–dependence of the electronic spectra. We predict a two–peak structure and different power laws with respect to the unknown relative magnitude of the singlet and triplet contributions to the superconducting order parameter, revealing a large variety of characteristic fingerprints of the underlying condensate.<sup>2</sup>

**1. Introduction.** In a large class of conventional and in particular unconventional superconductors a classification of the order parameter with respect to spin singlet/even parity and spin triplet/odd parity is possible, using the Pauli exclusion principle. A necessary prerequisite for such a classification is, however, the existence of an inversion center. Something of a stir has been caused by the discovery of the bulk superconductor CePt<sub>3</sub>Si without inversion symmetry (see [1, 2] and references therein), which initiated extensive theoretical (see [1, 2] and references therein) and experimental studies (see [1, 2] and referenced therein). In such systems the existence of an antisymmetric potential gradient causes a parity–breaking antisymmetric spin–orbit coupling (ASOC), that gives rise to the possibility of having admixtures of spin–singlet and spin–triplet pairing states. Such parity–violated, non–centrosymmetric superconductors (NCS) are the topic of this chapter, which is dedicated particularly to a theoretical study of response and transport properties at low temperatures. We will use the framework of a kinetic theory described by a set of generalized Boltzmann equations, successfully used before in [3], to derive various response and transport functions such as the normal and superfluid density, the specific heat capacity (i. e. normal fraction and condensate properties, that are native close to the long wavelength, stationary limit) and in particular the electronic Raman response in NCS (which involves frequencies  $\hbar\omega$  comparable to the energy gap  $\Delta_{\mathbf{k}}$  of the superconductor).

A few general remarks about the connection between response and transport phenomena are appropriate at this stage. Traditionally, the notion of transport implies that the theoretical description takes into account the effects of quasiparticle scattering processes, represented, say, by a scattering rate  $\Gamma$ . Therefore, we would like to demonstrate with a simple example, how response and transport are intimately connected: consider the density response of normal metal electrons to the presence of the two electromagnetic potentials  $\Phi^{\text{ext}}$  and  $\mathbf{A}^{\text{ext}}$ , which

<sup>1</sup>Max–Planck–Institut für Festkörperforschung, Stuttgart, Germany

<sup>2</sup>This project will be published as a book chapter [1] and is available as a preprint on arXiv [2].

generate the gauge-invariant form of the electric field  $\mathbf{E} = -\nabla\Phi^{\text{ext}} - \partial\mathbf{A}/c\partial t$ . In Fourier space ( $\nabla \rightarrow i\mathbf{q}$ ,  $\partial/\partial t \rightarrow -i\omega$ ) one may write for the response of the charge density:

$$\delta n_e = e^2 i\mathbf{q} \cdot \mathbf{M}_0(\mathbf{q}, \omega) \cdot \mathbf{E}$$

with  $\mathbf{M}_0$  the Lindhard tensor and  $\mathbf{q} \cdot \mathbf{M}_0 \cdot \mathbf{q} \equiv M_0$  the Lindhard function, appropriately renormalized by collision effects [4]:

$$M_0(\mathbf{q}, \omega) = \frac{\mathcal{L}_0(\mathbf{q}, \omega + i\Gamma)}{1 - \frac{i\Gamma}{\omega + i\Gamma} \left[ 1 - \frac{\mathcal{L}_0(\mathbf{q}, \omega + i\Gamma)}{\mathcal{L}_0(\mathbf{q}, 0)} \right]}$$

Here  $\mathcal{L}_0(q, \omega)$  denotes the unrenormalized Lindhard function in the collisionless limit  $\Gamma \rightarrow 0$ :

$$\mathcal{L}_0(\mathbf{q}, \omega) = \frac{1}{V} \sum_{\mathbf{p}\sigma} \frac{n_{\mathbf{p}+\mathbf{q}/2}^0 - n_{\mathbf{p}-\mathbf{q}/2}^0}{\epsilon_{\mathbf{p}+\mathbf{q}/2}^0 - \epsilon_{\mathbf{p}-\mathbf{q}/2}^0 - \hbar\omega} .$$

In this definition of the Lindhard function,  $n_{\mathbf{k}}^0$  denotes the equilibrium Fermi–Dirac distribution function and  $\epsilon_{\mathbf{k}}^0 = \xi_{\mathbf{k}} + \mu$  represents the band structure. Now the aspect of transport comes into play by the observation that  $M_0(\mathbf{q}, \omega + i\Gamma)$  may be expressed through the full dynamic conductivity tensor  $\sigma(\mathbf{q}, \omega) = e^2(\partial n/\partial \mu)\mathbf{D}(\mathbf{q}, \omega)$  of the electron system as follows:

$$M_0(\mathbf{q}, \omega) \equiv \frac{\mathbf{q} \cdot \sigma(\mathbf{q}, \omega) \cdot \mathbf{q}}{i\omega - \mathbf{q} \cdot \mathbf{D}(\mathbf{q}, \omega) \cdot \mathbf{q}/(1 - i\omega\tau)}$$

with  $\mathbf{q} \cdot \sigma \cdot \mathbf{q} \stackrel{\Gamma \rightarrow 0}{\equiv} i\omega e^2 \mathcal{L}_0(\mathbf{q}, \omega)$  and with the so-called diffusion pole in the denominator of  $M_0(\mathbf{q}, \omega)$  reflecting the charge conservation law. This expression for the Lindhard response function  $M_0$  clearly demonstrates the connection between response (represented by  $M_0$  itself) and transport (represented by the conductivity  $\sigma$ ), which can be evaluated both in the clean limit  $\Gamma \rightarrow 0$  and in the presence of collisions  $\Gamma \neq 0$ . In this sense, the notions of response and transport are closely connected and therefore equitable. In this whole chapter we shall limit our considerations to the collisionless case.

An important example for a response phenomenon involving finite frequencies is the electronic Raman effect. Of particular interest is the so-called pair-breaking Raman effect, in which an incoming photon breaks a Cooper pair of energy  $2\Delta_{\mathbf{k}}$  on the Fermi surface, and a scattered photon leaves the sample with a frequency reduced by  $2\Delta_{\mathbf{k}}/\hbar$ , has turned out to be a very effective tool to study unconventional superconductors with gap nodes. This is because various choices of the photon polarization with respect to the location of the nodes on the Fermi surface allow one to draw conclusions about the node topology and hence the pairing symmetry. An example for the success of such an analysis is the important work by Devereaux *et al.* [5] in which the  $d_{x^2-y^2}$ -symmetry of the order parameter in cuprate superconductors could be traced back to the frequency-dependence of the electronic Raman spectra, that directly measured the pair-breaking effect. Various theoretical studies of NCS have revealed a very rich and complex node structure in parity-mixed order parameters, which can give rise to qualitatively very different shapes, i. e. frequency dependencies, of the Raman intensities, ranging from threshold- and cusp- to singularity-like behavior [6]. Therefore the study of the polarization dependence of Raman spectra enables one to draw conclusions about the internal structure of the parity-mixed gap parameter in a given NCS.

**2. Antisymmetric spin-orbit coupling.** The order parameter of conventional and unconventional superconductors is usually classified as either spin singlet (even parity) or spin triplet

(odd parity) by the Pauli exclusion principle. A necessary prerequisite for such a classification is, however, the existence of an inversion center. Something of a stir has been caused by the discovery of the bulk superconductor CePt<sub>3</sub>Si without inversion symmetry which initiated extensive theoretical and experimental studies. In such systems the existence of an antisymmetric potential gradient causes a parity–breaking antisymmetric spin–orbit coupling (ASOC) that leads to a splitting of the Fermi surface and, moreover, gives rise to the unique possibility of having admixtures of spin–singlet and spin–triplet pairing states. At present, however, the relative magnitude of both contributions to the superconducting order parameter is unknown. In this letter, we propose that inelastic (Raman) light scattering provides a powerful tool to solve this problem and, in general, to investigate the underlying condensate in such parity–violated, non–centrosymmetric superconductors (NCS). This is because various choices of the photon polarization with respect to the location of the nodes on the Fermi surface allow one to draw conclusions about the node topology and hence the pairing symmetry. Therefore, our predictions of the polarization dependence of Raman spectra enable one to draw conclusions about the internal structure of the parity–mixed condensate in a given NCS.

The model Hamiltonian for noninteracting electrons in a non-centrosymmetric crystal reads

$$\hat{H} = \sum_{\mathbf{k}\sigma\sigma'} \hat{c}_{\mathbf{k}\sigma}^\dagger [\zeta_{\mathbf{k}}\delta_{\sigma\sigma'} + \mathbf{g}_{\mathbf{k}} \cdot \boldsymbol{\tau}_{\sigma\sigma'}] \hat{c}_{\mathbf{k}\sigma'} \quad (1)$$

where  $\zeta_{\mathbf{k}}$  represents the bare band dispersion,  $\sigma, \sigma' = \uparrow, \downarrow$  label the spin state and  $\boldsymbol{\tau}$  are the Pauli matrices. The second term describes an ASOC with a coupling  $\mathbf{g}_{\mathbf{k}}$ . In NCS two important classes of ASOCs are realized reflecting the underlying point group  $\mathcal{G}$  of the crystal. Therefore, we shall be interested in the tetragonal point group  $C_{4v}$  (application to CePt<sub>3</sub>Si, for example) and the cubic point group  $O(432)$  (applicable to the system Li<sub>2</sub>Pd<sub>x</sub>Pt<sub>3-x</sub>B). For  $\mathcal{G} = C_{4v}$  the ASOC reads  $\mathbf{g}_{\mathbf{k}} = g_{\perp}(\hat{\mathbf{k}} \times \hat{\mathbf{e}}_z) + g_{\parallel}\hat{k}_x\hat{k}_y\hat{k}_z(\hat{k}_x^2 - \hat{k}_y^2)\hat{\mathbf{e}}_z$ . In the purely two-dimensional case ( $g_{\parallel} = 0$ ) one recovers what is known as the Rashba interaction. For the cubic point group  $\mathcal{G} = O(432)$   $\mathbf{g}_{\mathbf{k}}$  reads  $\mathbf{g}_{\mathbf{k}} = g_1\hat{\mathbf{k}} - g_3 \left[ \hat{k}_x(\hat{k}_y^2 + \hat{k}_z^2)\hat{\mathbf{e}}_x + \hat{k}_y(\hat{k}_z^2 + \hat{k}_x^2)\hat{\mathbf{e}}_y + \hat{k}_z(\hat{k}_x^2 + \hat{k}_y^2)\hat{\mathbf{e}}_z \right]$ , where the ratio  $g_3/g_1$  can be estimated to be  $\simeq 3/2$ . Diagonalizing the Hamiltonian one finds the eigenvalues  $\zeta_{\mathbf{k}\pm} = \zeta_{\mathbf{k}} \pm |\mathbf{g}_{\mathbf{k}}|$ , which physically correspond to the lifting of the Kramers degeneracy between the two spin states at a given  $\mathbf{k}$ . Sigrist and co-workers have shown that the presence of the ASOC generally allows for an admixture between a spin–triplet order parameter and a spin–singlet pairing gap. This implies that we can write down the following ansatz for the energy gap matrix in spin space  $\Delta_{\mathbf{k}\sigma\sigma'} = [(\psi_{\mathbf{k}}(T)\mathbf{1} + \mathbf{d}_{\mathbf{k}}(T) \cdot \boldsymbol{\tau})i\tau^y]_{\sigma\sigma'}$ , where  $\psi_{\mathbf{k}}(T)$  and  $\mathbf{d}_{\mathbf{k}}(T)$  reflect the singlet and triplet part of the pair potential, respectively. It is then easy to see that the ASOC is not destructive for triplet pairing if one assumes  $\mathbf{d}_{\mathbf{k}} \parallel \mathbf{g}_{\mathbf{k}}$ . This results in the following ansatz for the gap function on both bands (+,–)

$$\Delta_{\mathbf{k}\pm} = \psi \pm d|\mathbf{g}_{\mathbf{k}}| = \psi (1 \pm p|\mathbf{g}_{\mathbf{k}}|) \equiv \Delta_{\pm} , \quad (2)$$

where the parameter  $p = d/\psi$  represents the unknown triplet–singlet ratio. Accordingly, the Bogoliubov–quasiparticle dispersion is given by  $E_{\pm}^2(\mathbf{k}) = \zeta_{\pm}^2(\mathbf{k}) + \Delta_{\pm}^2(\mathbf{k})$ . If we assume no  $\mathbf{q}$ –dependence of the order parameter,  $\Delta_{\lambda}(\mathbf{k})$  [and also  $E_{\lambda}(\mathbf{k})$ ] is of even parity i.e.  $\Delta_{\lambda}(-\mathbf{k}) = \Delta_{\lambda}(\mathbf{k})$ . It is quite remarkable that although the spin representation of the order parameter  $\Delta_{\sigma\sigma'}(\mathbf{k})$  has no well–defined parity w.r.t.  $\mathbf{k} \rightarrow -\mathbf{k}$ , the energy gap in band representation has. Note that for Li<sub>2</sub>Pd<sub>x</sub>Pt<sub>3-x</sub>B the parameter  $p$  seems to be directly related to the substitution of platinum by palladium, since the larger spin–orbit coupling of the heavier platinum is expected to enhance the triplet contribution. This seems to be confirmed by penetration depth experiments. The remaining part of section 2 is devoted to a discussion of the equilibrium gap equation, which cannot be given here for lack of space. For the same reason we shall have to restrict ourselves to providing only a short description of the contents of the sections 3 to 8:

**3. Derivation of the transport equations.** Here we derive the kinetic transport equations for NCS in particle–hole (Nambu) space at low temperatures in the clean limit and transform these equations into the more convenient band–basis.

**4. Solution by Bogoliubov transformation.** In this section the transport equations will be solved quite generally in band– and Nambu space by first performing a Bogoliubov transformation to the quasiparticle–quasihole phase space and second performing the inverse Bogoliubov transformation to recover the original distribution functions.

**5. Gauge invariance.** We shall demonstrate gauge invariance of our theory in this section by rigorously taking the fluctuations of the order parameter into account. It can be shown how the gauge–invariance is intimately connected with the charge conservation law for the condensate.

**6. Normal and superfluid density.** As an example for the local (reactive) quasiparticle and condensate response, we calculate in this section the normal and superfluid density.

**7. The specific heat capacity.** This section is devoted to an understanding of the thermodynamics of the gas of thermal excitations and particularly deals with the result for the specific heat capacity.

**8. A case study: Raman response.** In this section our particular interest will be focussed on the electronic Raman response. We investigate the polarization–dependence of the pair–breaking Raman response at zero temperature for two important classes of the involved spin–orbit coupling.

**9. Conclusion.** In this book chapter, we derived response and transport functions for non-centrosymmetric superconductors from a kinetic theory with particular emphasis on the Raman response. We started from the generalized von Neumann equation which describes the evolution of the momentum distribution function in time and space and derived a linearized matrix–kinetic (Boltzmann) equation in  $\omega$ – $\mathbf{q}$ –space. This kinetic equation is a  $4 \times 4$  matrix equation in both particle–hole (Nambu) and spin space. We explored the Nambu–structure and solved the kinetic equation quite generally by first performing an  $SU(2)$  rotation into the band–basis and second applying a Bogoliubov–transformation into quasiparticle space. Our theory is particle–hole symmetric, applies to any kind of antisymmetric spin–orbit coupling, and holds for arbitrary quasiclassical frequency and momentum with  $\hbar\omega \ll E_F$  and  $|\mathbf{q}| \ll k_F$ . Furthermore, assuming a separable ansatz in the pairing interaction, we demonstrated gauge invariance and charge conservation for our theory. Within this framework, we derived expressions for the normal and superfluid density and compared the results in the static and long–wavelength limit with those from a local equilibrium analysis. The same investigations were done for the specific heat capacity. In both cases we recover the same results, which validates our theory. Finally, we presented analytic and numeric results for the electronic (pair–breaking) Raman response in noncentrosymmetric superconductors for zero temperature. Therefore we analyzed the two most interesting classes of tetragonal and cubic symmetry, applying for example to  $CePt_3Si$  ( $\mathcal{G} = C_{4v}$ ) and  $Li_2Pd_xPt_{3-x}B$  ( $\mathcal{G} = O$ ). Accounting for the antisymmetric spin–orbit coupling, we provide various analytic results such as the Raman vertices for both point groups, the Raman response for several pure triplet states, and power laws and kink positions for mixed–parity states. Our numeric results cover all relevant cases

from weak to strong triplet–singlet ratio and demonstrate a characteristic two–peak structure for Raman spectra of non–centrosymmetric superconductors. Our theoretical predictions can be used to analyze the underlying condensate in parity–violated noncentrosymmetric superconductors and allow the determination of the unknown triplet–singlet ratio.

## References

- [1] E. Bauer and M. Sigrist (eds.) *Non-centrosymmetric Superconductivity* (Springer Verlag, Heidelberg, 2011).
- [2] L. Klam, D. Manske, and D. Einzel, arXiv:1003.0407v1 (2010).
- [3] D. Einzel and L. Klam, *J. Low Temp. Phys.* **150**, 57 (2008).
- [4] N. D. Mermin, *Phys. Rev. B* **1**, 2362 (1970).
- [5] T. P. Devereaux, D. Einzel, B. Stadlober, R. Hackl, D. H. Leach, and J. J. Neumeier, *Phys. Rev. Lett.* **72**, 396 (1994).
- [6] L. Klam, D. Einzel, and D. Manske, *Phys. Rev. Lett.* **102**, 027004 (2009).

## Superconductivity at High Transition Temperatures

R. Hackl<sup>1,2</sup>

After six years, the funding for the DFG Research Unit “Doping Dependence of Phase Transitions and Ordering Phenomena in Copper-Oxygen Superconductors” (FOR 538) expired on June 30, 2010. Six and nine groups participated during the two funding periods between 2004 and 2010. The focus was placed on the physics of copper-oxygen superconductors and shifted partially to the ferro-pnictides after 2008. Both material classes are characterized by competing ordering instabilities and high superconducting transition temperature  $T_c$  as shown in Fig. 1.

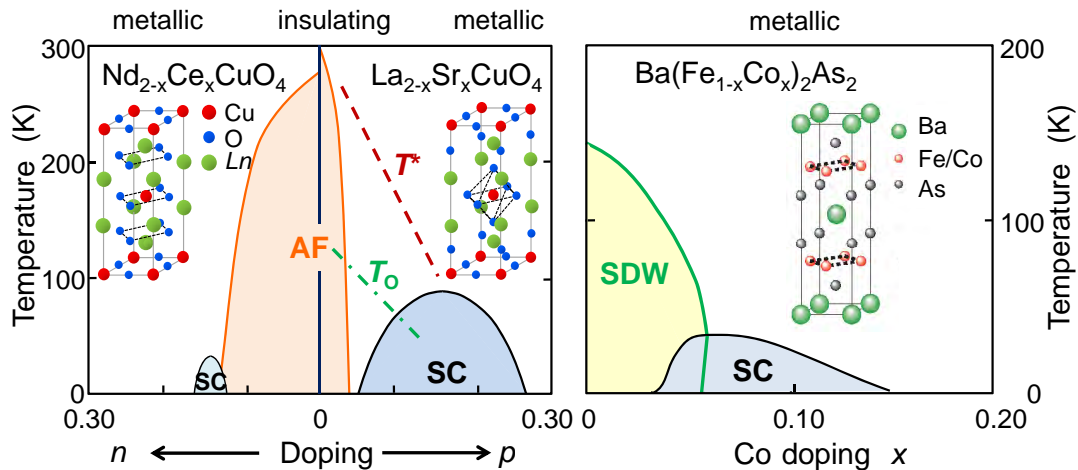


**Figure 1:** Phase diagrams of copper (left) and iron based (right) superconductors. Typical crystal structures are shown in the insets.  $\text{La}_{2-x}\text{Sr}_x\text{CuO}_4$  with a maximal transition temperature  $T_c^{\text{max}}$  of approximately 40 K belongs to the material class first discovered by Bednorz and Müller in 1986 [1]. The antiferromagnetism (AF) close to half filling (zero doping) and the superconducting (SC) dome are similar in all hole-doped cuprates and only  $T_c^{\text{max}}$  varies between 30 and 160 K. Additional crossover behavior is observed at  $T^*$  and  $T_0$ . On the electron doped side,  $T_c^{\text{max}}$  does not exceed 30 K.  $\text{Ba}(\text{Fe}_{1-x}\text{Co}_x)_2\text{As}_2$  belongs to the oxygen-free “122” iron pnictides [2] with  $T_c^{\text{max}} = 38$  K. In the oxy-pnictides  $T_c^{\text{max}}$  can reach 56 K. In contrast to the cuprates the phase diagrams of the pnictides depend on the material class. The continuous suppression of the competing spin-density wave state (SDW) is so far observed only in the 122 compounds.

Even if the most tantalizing question as to the origin of the high  $T_c$  could not be answered substantial progress towards a better understanding was achieved. Recently, it could be shown that the pairing interaction between the electrons is predominantly retarded similarly as in conventional superconductors with electron-phonon coupling. In the strongly correlated cuprates instantaneous contributions originating from the Coulomb repulsion do not dominate the Cooper pairing [3]. Secondly, the other instabilities, primarily spin and charge order, are closely related to superconductivity, and their fluctuations are candidates for mediating electron pairing. Since phonons couple directly to charge fluctuations the lattice cannot be disregarded either in the case of the cuprates. In the iron arsenides, on the other hand, the electron-lattice interaction is considered particularly weak [4].

The basis of the systematic studies in the Research Unit were high-quality single crystals in the broadest possible doping ranges. This was achieved during the two funding periods for both electron and hole doped cuprates [5]. The quality of the  $\text{Nd}_{2-x}\text{Ce}_x\text{CuO}_4$  crystals was high enough to facilitate the observation of quantum oscillations. Although  $\text{YBa}_2\text{Cu}_3\text{O}_{6+x}$  has

<sup>1</sup>The work at WMI has been done in collaboration with A. Baum, T. Böhm, T. Buttler, H.-M. Eiter, A. Erb, C. Hartinger, P. Jaschke, F. Kretschmar, M. Lambacher, N. Munnikes, B. Muschler, W. Prestel, L. Tassini, F. Venturini.

<sup>2</sup>Support by the German Research Foundation (DFG) via Research Unit FOR 538 and Priority Program SPP 1458 is gratefully acknowledged.

still the best crystal quality angle-resolved photoemission experiments (ARPES) rely to a large extent on  $\text{Bi}_2\text{Sr}_2\text{CaCu}_2\text{O}_{8+\delta}$  for the superior surface quality after in-situ cleaving. Therefore, a sensible selection of samples remains a central issue.

The close collaboration of spectroscopists, material scientists, and theorists in FOR 538 offered the opportunity to simultaneously analyze the results of independent spectroscopical methods and to derive the coupling spectra and their impact on the electron dynamics in the spirit of an Eliashberg approach. Various aspects could be clarified in this way. In one of the joint efforts the spin-excitation spectrum of underdoped  $\text{YBa}_2\text{Cu}_3\text{O}_{6.6}$  was measured by neutron scattering and used to determine the renormalization of the electronic dispersion. The synthetic spectrum compares well with the dispersion derived from ARPES. The coupling constant obtained for electron-spin interaction appears to be sufficient for high- $T_c$  superconductivity [6]. Other experiments show that charge fluctuations and phonons couple also strongly to the electrons. In a recent time-resolved experiment in  $\text{YBa}_2\text{Cu}_3\text{O}_{6.93}$  the coupling between the apex-oxygen phonon and the condensate was measured directly [7]. The inversion of the electronic Raman spectra yields a distinct momentum dependence of the coupling spectra indicating that different types of excitations couple to the electrons in different regions of the Brillouin zone [8]. Selection rules resulting from higher order interaction terms show that charge fluctuations couple preferably to the electrons propagating along the diagonals of the  $\text{CuO}_2$  plane while the spins interact with the electrons in the  $(\pi, 0)$  regions. Above optimal doping the charge contribution gains influence at the expense of the spin fluctuations [9]. In the pseudogap range of underdoped  $\text{YBa}_2\text{Cu}_3\text{O}_{6+x}$  the doping dependence of the  $c$ -axis conductivity [9] also indicates a competition between different instabilities.

This brief summary may demonstrate that some larger steps towards a better understanding of the cuprates have been made. The study of the pnictides may further the clarification since the origin of superconductivity here is probably less diverse than in the cuprates even if the non-universal phase diagrams argue otherwise at first glance [10].

The results of the Research Unit have been communicated in more than 100 topical publications, many of them in high-profile journals. A recent snapshot can be found in volume 188 of the European Physical Journal Special Topics (October 1, 2010) which features also an extended version of this contribution here [11]. In addition to publications, the Research Unit disseminated the results in 7 international meetings in Dresden, Ringberg and Munich with typically 60 participants and 20 invited international speakers guaranteeing a high visibility.

## References

- [1] J. G. Bednorz and K. A. Müller, *Z. Phys. B* **64**, 189 (1986).
- [2] M. Rotter, M. Tegel, and D. Johrendt, *Phys. Rev. Lett.* **101**, 107006 (2008).
- [3] W. Hanke, M. L. Kiesel, M. Aichhorn, S. Brehm, and E. Arrigoni, *Eur. Phys. J. Special Topics* **188**, 15 (2010).
- [4] L. Boeri, O. V. Dolgov, and A. A. Golubov, *Phys. Rev. Lett.* **101**, 026403 (2008).
- [5] M. Lambacher, T. Helm, M. Kartsovnik, and A. Erb, *Eur. Phys. J. Special Topics* **188**, 61 (2010).
- [6] T. Dahm, V. Hinkov, S. V. Borisenko, A. A. Kordyuk, V. B. Zabolotnyy, J. Fink, B. Büchner, D. J. Scalapino, W. Hanke, and B. Keimer, *Nature Phys.* **5**, 217 (2009).
- [7] A. Pashkin, M. Porer, M. Beyer, K. W. Kim, A. Dubroka, C. Bernhard, X. Yao, Y. Dagan, R. Hackl, A. Erb, J. Demsar, R. Huber, and A. Leitenstorfer, *Phys. Rev. Lett.* **105**, 067001 (2010).
- [8] B. Muschler, W. Prestel, E. Schachinger, J. P. Carbotte, R. Hackl, Shimpei Ono, and Yoichi Ando, *J. Phys.: Condensed Matter* **22**, 375702 (2010).
- [9] S. Caprara, C. Di Castro, B. Muschler, R. Hackl, M. Lambacher, A. Erb, Seiki Komiyama, Yoichi Ando, and M. Grilli, arXiv: 1010.0180 (2010).
- [10] C. Honerkamp, *Eur. Phys. J. Special Topics* **188**, 33 (2010).
- [11] R. Hackl and W. Hanke, *Eur. Phys. J. Special Topics* **188**, 3 (2010).

## Investigating the Doping-Dependent Fermi Surface of the Superconducting Cuprate $\text{Nd}_{2-x}\text{Ce}_x\text{CuO}_4$ with the Help of High Magnetic Fields

T. Helm, M. V. Kartsovnik, W. Biberacher, A. Erb, and R. Gross <sup>1</sup>  
C. Putzke <sup>2</sup>, I. Sheikin <sup>3</sup>, C. Proust <sup>4</sup>

High-field magnetotransport has recently proved extremely helpful for elucidating the fermiology of cuprate superconductors [1–5]. We succeeded to observe quantum oscillations of the magnetoresistance, the Shubnikov-de Haas (SdH) effect, in the electron-doped cuprate  $\text{Nd}_{2-x}\text{Ce}_x\text{CuO}_4$  (NCCO) [4]. A dramatic change in the oscillation spectrum was found, revealing a transformation of the cyclotron orbit topology on increasing the doping level  $x$  from 0.16 to 0.17. On the other hand, angle-dependent magnetoresistance oscillations (AMRO) did not show an appreciable change in the same doping range [3]. Here, we present new results on the angle-dependent magnetoresistance and SdH oscillations obtained at higher magnetic fields [5]. Our data provides a compelling evidence for a translational symmetry breaking persisting in the material up to highest doping level.

The NCCO crystals used in our experiments were grown by traveling solvent floating zone technique [6]. In the magnetotransport experiment an *in situ* sample rotation was performed with a home-made 2-axes rotator at temperatures between 25 K and 1.4 K. The interlayer resistance was measured as a function of polar angle  $\theta$  between the field direction and crystallographic [001]-axis in fields up to 34 T, at different fixed azimuthal angles  $\varphi$  [see Fig. 1(b)]. SdH oscillations were studied in pulsed fields up to 70 T applied perpendicular to  $\text{CuO}_2$  layers.

The angle-dependent interlayer magnetoresistance of NCCO appears to be very complex due to competing contributions from incoherent, coherent orbital, and superconducting effects. Fig. 1(a) shows data of 3 different

electron-doping levels ranging from a nearly optimal,  $x = 0.15$ , to a strongly overdoped,  $x = 0.17$ , composition. In the range  $|\theta| \leq 30^\circ$  they display an anomalous dome which we could not relate to AMRO due to its anomalous  $T$ -dependence. It is more likely associated with an incoherent, spin-dependent interlayer transport mechanism found also for underdoped samples [3]. Compared to the data obtained in fields up to 28 T, the AMRO

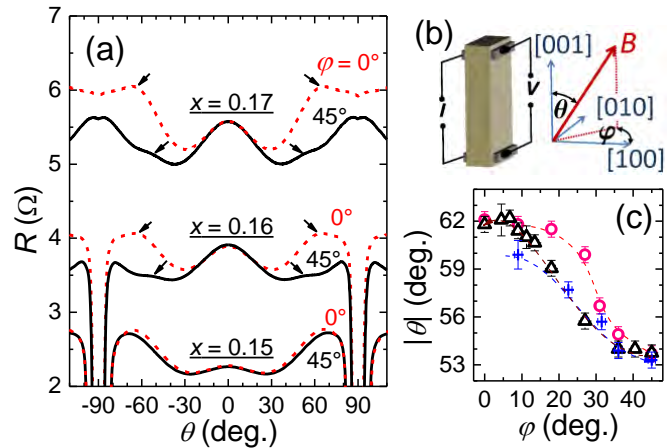


**Figure 1:** (a) Angle-dependent interlayer magnetoresistance of  $\text{Nd}_{2-x}\text{Ce}_x\text{CuO}_4$  for different doping levels  $x$  as a function of tilt angle  $\theta$ , at  $B = 34$  T and  $T = 1.4$  K. The range  $|\theta| < 75^\circ$  corresponds to the normal conducting state; the rapid drop around  $|\theta| = 90^\circ$  is due to superconductivity. Arrows point to the AMRO features. (b) Sketch of the experimental configuration. (c) Angular positions  $|\theta|$  of the AMRO features plotted vs. the azimuthal angle  $\varphi$  for  $x = 0.16$  (blue crosses), 0.165 (black triangles) and 0.17 (pink circles).

<sup>1</sup>This work was supported by the German Research Foundation via the Research Unit FOR 538 and grant GR 1132/15, as well as by EuroMagNET II under the EC contract 228043.

<sup>2</sup>Hochfeld-Magnetlabor Dresden, Forschungszentrum Dresden-Rossendorf, Dresden, Germany

<sup>3</sup>Laboratoire National des Champs Magnétiques Intenses, CNRS, Grenoble, France

<sup>4</sup>Laboratoire National des Champs Magnétiques Intenses, (CNRS, INSA, UJF, UPS), Toulouse, France

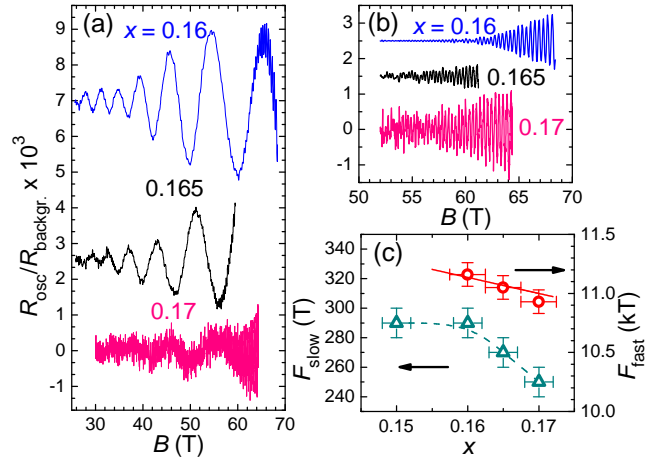
features (indicated by arrows) are more pronounced at 34 T and we were able to trace their  $\varphi$ -dependence in more detail for  $x = 0.16, 0.165$  and  $0.17$ , see Fig. 1(c). The fact that the  $\varphi$ -dependence of the AMRO positions is almost identical for all three doping levels means that the shape of the relevant Fermi surfaces is also the same. For  $x = 0.15$ , the angle-dependent magnetoresistance background appears to be similar but without AMRO features.

Figure 2(a) shows SdH oscillations in the interlayer resistance for  $x = 0.17, 0.165$  and  $0.16$  obtained in pulsed magnetic fields up to 70 T. Fast oscillations [Fig. 2(b)] with frequencies  $F_{\text{fast}} \sim 11$  kT were observed above 52 T. They are superimposed by slow oscillations which can be traced down to below 40 T. The low frequencies are similar to the value  $F_{\text{slow}} = 290$  T measured for crystals with  $x = 0.15$  [4]. Fig. 2(c) shows the decrease of both high and low frequencies when the carrier concentration is increased towards strong overdoping. The frequency shift for the large orbit is in good agreement with what is expected from band structure calculations [see red line in Fig. 2(c)]. Thus, a mixture of two phases as origin for the different Fermi surfaces can be ruled out unambiguously. It was pointed out in our previous work [4] that the occurrence of low frequency oscillations is attributed to small hole pockets of the reconstructed Fermi surface. The simultaneous occurrence of slow and fast oscillations at very high fields can consistently be explained by magnetic breakdown through the gap between electron- and hole-like parts of the Fermi surface.

The present data [5] clearly indicates that the Fermi surface is still reconstructed even at  $x = 0.17$ , which is the highest obtainable doping level in bulk NCCO crystals [6]. The corresponding superlattice potential is, however, very weak, allowing magnetic breakdown, as evidenced by the observation of the fast SdH oscillations. Further high-field experiments are required to understand why AMRO and SdH oscillations are not found below optimal doping and how the ordering responsible for the present Fermi surface reconstruction is related to superconductivity in this material class.

## References

- [1] N. Doiron-Leyraud, C. Proust, D. LeBoeuf, J. Levallois, J.-B. Bonnemaïson, R. Liang, D. A. Bonn, W. N. Hardy, and L. Taillefer, *Nature* **447**, 565 (2007).
- [2] N. E. Hussey, M. Abdel-Jawad, A. Carrington, A. P. Mackenzie, and L. Balicas, *Nature* **425**, 814 (2003).
- [3] T. Helm, M. V. Kartsovnik, A. Erb, and R. Gross, WMI annual report 68–74 (2009).
- [4] T. Helm, M. V. Kartsovnik, M. Bartkowiak, N. Bittner, M. Lambacher, A. Erb, J. Wosnitza, and R. Gross, *Phys. Rev. Lett.* **103**, 157002 (2009).
- [5] T. Helm, M. V. Kartsovnik, I. Sheikin, M. Bartkowiak, F. Wolff-Fabris, N. Bittner, W. Biberacher, M. Lambacher, A. Erb, J. Wosnitza, and R. Gross, *Phys. Rev. Lett.* **105**, 247002 (2010).
- [6] M. Lambacher, T. Helm, M. Kartsovnik, and A. Erb, *Eur. Phys. J. Special Topics* **188**, 61 (2010).



**Figure 2:** (a) Normalized oscillating part of the interlayer magnetoresistance for three different doping levels in pulsed fields up to 70 T, at  $T = 2.5$  K. Curves are shifted vertically for a better visibility. (b) High field fragments showing high frequency oscillations. (c) Frequencies of fast and slow oscillations plotted vs. electron-doping  $x$ . The red line is a fit to what is expected from the band structure.

## Doping Dependence of the Electronic Properties of $\text{Ba}(\text{Fe}_{1-x}\text{Co}_x)_2\text{As}_2$

B. Muschler, F. Kretzschmar, R. Hackl <sup>1</sup>  
 J.-H. Chu, J. G. Analytis, I. R. Fisher <sup>2,3</sup>

The superconductivity in the iron-pnictides with transition temperatures  $T_c$  up to 56 K is probably not originating from electron-phonon coupling [1]. The compounds have well nested electron and hole pockets at the  $(\pi, 0)$  points and the center of the one iron Brillouin zone, respectively, with similar cross sections. In this study we present the doping dependence of the carrier dynamics of  $\text{Ba}(\text{Fe}_{1-x}\text{Co}_x)_2\text{As}_2$  in the normal state as seen via electronic Raman scattering (ERS). ERS offers the possibility to probe these bands independently in  $A_{1g}$  (hole pockets) and  $B_{1g}$  (electron pockets) symmetry [2] and to test the bulk properties of the material. The samples used are single crystals with doping levels  $x = 0.045, 0.051, 0.055, 0.061$  and  $0.085$  and a maximal transition temperature of 24 K for optimal doping ( $x = 0.061$ ).

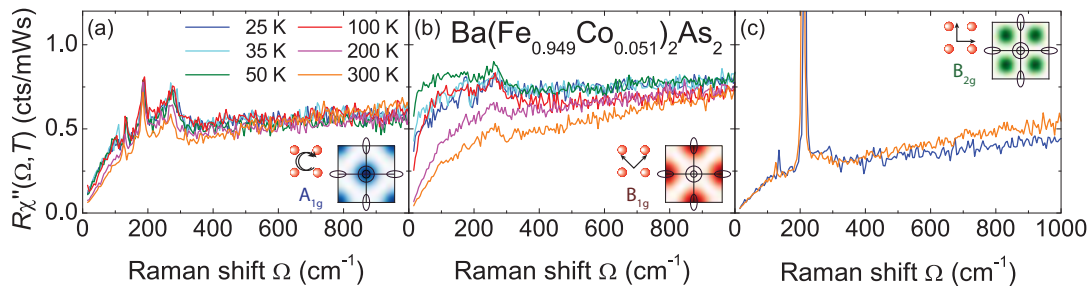


**Figure 1:** Raman response of  $\text{Ba}(\text{Fe}_{1-x}\text{Co}_x)_2\text{As}_2$  with  $x=0.051$  in three different symmetries. The insets show the first Brillouin zone and the most sensitive region of the corresponding symmetry.

In Fig. 1 we show the Raman spectra of  $\text{Ba}(\text{Fe}_{0.949}\text{Co}_{0.051})_2\text{As}_2$  as a function of temperature in three different symmetries. The sample is slightly underdoped with a superconducting transition temperature of 18 K. The response in  $A_{1g}$  symmetry [Fig. 1(a)] is superposed by two allowed phonons: the mode at  $135 \text{ cm}^{-1}$  corresponds to the vibration of the iron and arsenic atoms in  $b$ -direction. The mode at  $185 \text{ cm}^{-1}$  corresponds to the displacement of the arsenic atoms in  $c$ -direction. The electronic continuum shows a weak temperature dependence. The initial slope increases with decreasing temperature but below 100 K there is hardly any change in the spectral shape. The same holds for  $B_{2g}$  symmetry [Fig. 1(c)]. For the lack of any temperature dependence of the spectra, as confirmed at other doping levels, we show only the spectra at 25 and 300 K. The spectra are superposed by the phonon at  $135 \text{ cm}^{-1}$  and a phonon at  $215 \text{ cm}^{-1}$ , which corresponds to the vibration of the iron atoms in  $c$ -direction. Only in  $B_{1g}$  symmetry we observe a pronounced temperature dependence of the Raman spectra [Fig. 1(b)]. Lowering the temperature from 300 to 50 K increases the initial slope of the spectra continuously. This trend is reversed for temperatures below 50 K down to the lowest measured temperature in the normal state. Here the initial slope of the spectra decreases with decreasing temperatures.

We analyze the Raman spectra applying an extended Drude analysis where we can extract relaxation rates, which are inversely proportional to the initial slope of the Raman spectra. This analysis is adopted from the well known Drude analysis of the IR spectroscopy and is described elsewhere [3]. In the limit  $\Omega \rightarrow 0$  we can extract static Raman relaxation rates and

<sup>1</sup>Supported by the German Research Foundation via FOR 538, SPP 1458 and TRR 80

<sup>2</sup>Stanford Institute for Materials and Energy Sciences, SLAC National Accelerator Laboratory, 2575 Sand Hill Road, Menlo Park, CA 94025, USA

<sup>3</sup>Geballe Laboratory for Advanced Materials & Dept. of Applied Physics, Stanford University, CA 94305, USA

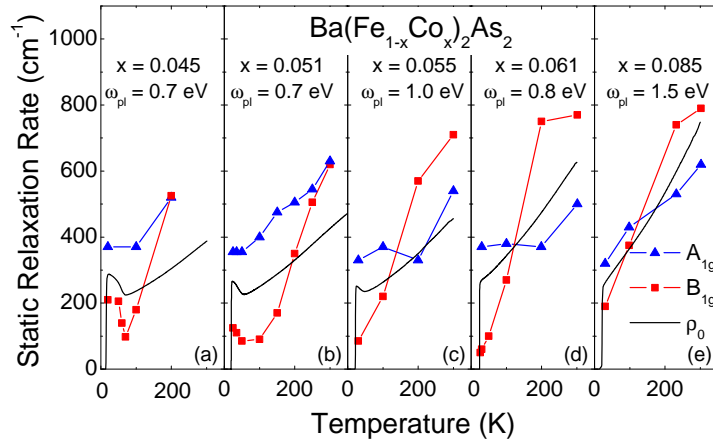


**Figure 2:** Doping dependence of the Raman relaxation rates on the hole ( $A_{1g}$ ) and electron bands ( $B_{1g}$ ). The resistivity measured on the same crystals are shown in solid black lines. The plasma frequency for the conversion of the transport data to units of wavenumbers is indicated.

compare them to the data of DC resistivity measurements. For the conversion of the transport data in units of  $m\Omega\text{cm}$  to units of wavenumbers we need to introduce a plasma frequency. The result of this analysis is presented in Fig. 2. In every panel the plasma frequencies are indicated and in approximate agreement with published data [4]. For all doping levels the temperature dependence of the relaxation rates in  $B_{1g}$  symmetry is much stronger than that in  $A_{1g}$  symmetry. For optimal doping [Fig. 2(d)] the relaxation rates for the lowest measured temperatures in the normal state are very small having values of  $60\text{ cm}^{-1}$ , which argues for the high crystal quality. In  $A_{1g}$  symmetry we find an almost temperature independent rate and the transport data seem to be an average of the rates of both symmetries. For the over- as well as for the underdoped samples the relaxation rates on the hole bands show a stronger temperature dependence than for optimal doping but only for the overdoped side [Fig. 2(e)] we find a good agreement between the Raman relaxation rates and the transport data. On the underdoped side the  $B_{1g}$  relaxation rates show a nonmonotonic temperature dependence in accordance with transport measurements on the same crystals [5]. Here the rates increase with the temperatures decreasing below approximately 60 K [Fig. 2(a),(b)].

Thus, with ERS we find strong and weak temperature dependencies of the relaxation rates for the electron and hole bands, respectively. The different rates in  $B_{1g}$  and  $A_{1g}$  symmetry for all doping levels are a clear indication of band and momentum dependent electron dynamics in the iron pnictides. These anisotropies favor electron-electron and electron-spin interactions which in turn would lead to a highly anisotropic energy gap in the superconducting state as shown earlier for this compound [6].

## References

- [1] L. Boeri, O. V. Dolgov, and A. A. Golubov, *Phys. Rev. Lett.* **101**, 026403 (2008).
- [2] I. I. Mazin, T. P. Devereaux, J. G. Analytis, J.-H. Chu, I. R. Fisher, B. Muschler, and R. Hackl, *Phys. Rev. B* **82**, 180502 (2010).
- [3] M. Opel, R. Nemetschek, C. Hoffmann, R. Philipp, P. F. Müller, R. Hackl, I. Tüttő, A. Erb, B. Revaz, E. Walker, H. Berger, and L. Forró, *Phys. Rev. B* **61**, 9752 (2000).
- [4] N. Barisić, D. Wu, M. Dressel, L. J. Li, G. H. Cao, and Z. A. Xu, *Phys. Rev. B* **82**, 054518 (2010).
- [5] J.-H. Chu, J. G. Analytis, C. Kucharczyk, and I. R. Fisher, *Phys. Rev. B* **79**, 014506 (2009).
- [6] B. Muschler, W. Prestel, R. Hackl, T. P. Devereaux, J. G. Analytis, J.-H. Chu, and I. R. Fisher, *Phys. Rev. B* **80**, 180510 (2009).

## Magnetic Transformations in the Organic Conductor $\kappa$ -(BETS)<sub>2</sub>Mn[N(CN)<sub>2</sub>]<sub>3</sub> at the Metal–Insulator Transition

M. V. Kartsovnik, W. Biberacher <sup>1</sup>

O. M. Vyaselev <sup>2</sup>

Crystalline organic conductors have constantly been in focus of research activities due to their rich electronic phase diagrams originating from strong electron correlations, particular Fermi surface topologies, and very high sensitivity to external parameters such as pressure and magnetic field. Synthesis of charge transfer salts of organic  $\pi$ -donors with paramagnetic metal-complex anions has added a new dimension to the physics of these materials due to the interaction between the conduction electrons of the  $\pi$  band with localized  $d$  electrons. This interaction leads to new fascinating phenomena such as magnetic-field-induced insulator-metal [1] and even superconducting [2] transitions.

The new layered conductor  $\kappa$ -(BETS)<sub>2</sub>Mn[N(CN)<sub>2</sub>]<sub>3</sub> [3] is expected to present a thrilling combination of potentially non-trivial magnetic properties, arising from the nearly triangular network of Mn<sup>2+</sup> ions in the anion layer, with strong electron correlations characteristic of the narrow half-filled conducting band of organic layers. At ambient pressure this compound undergoes a metal-insulator (MI) transition at  $T_{\text{MI}} \approx 25$  K, which is easily suppressed by external pressure  $< 1$  kbar, giving way to superconductivity below 5.5 K [4]. While the ambient pressure ground state was suggested to be a Mott insulator [1], the role of the interaction between itinerant spins in the donor layers and localized spins of Mn<sup>2+</sup> is still an open question. To clarify this issue, we have studied magnetic properties of  $\kappa$ -(BETS)<sub>2</sub>Mn[N(CN)<sub>2</sub>]<sub>3</sub> around the MI transition by means of dc magnetization and magnetic torque measurements.

Magnetization measurements were done in a Quantum Design MPMS-XL SQUID magnetometer on a 90  $\mu\text{g}$  sample with a magnetic field  $\mu_0 H \leq 7$  T directed along the crystallographic  $b$  and  $c$  axes parallel to the conducting BETS layers as well as along  $a^* \perp bc$ . At temperatures above  $T_{\text{MI}}$  the magnetization precisely follows the Curie law  $M = \chi_{\text{CW}} H$ , where  $\chi_{\text{CW}} = C_m / (T - \theta)$  is the Curie-Weiss susceptibility with  $C_m = 5.50 \text{ m}^3 \text{ K/mol}$  and  $\theta = -5.9$ ,  $-4.6$ , and  $-4.9$  K, for  $H \parallel a^*$ ,  $b$ , and  $c$ , respectively. This result indicates a dominating role of localized moments of Mn<sup>2+</sup> in the high-spin state with antiferromagnetic (AF) interactions, in agreement with an earlier report [3]. Below  $T_{\text{MI}}$  the magnetic susceptibility  $\chi$  deviates downwards from  $\chi_{\text{CW}}$ , as shown in Fig. 1(a), suggesting a progressive freezing of the Mn<sup>2+</sup> spin degrees of freedom. However, the effect is rather weak and develops very slowly with cooling, which is atypical of a usual Néel-type ordering.

Magnetic torque measurements were done using a home-made cantilever beam setup on a 40  $\mu\text{g}$  sample in fields up to 15 T. The field was rotated in different planes perpendicular to the conducting  $bc$ -plane. Like in the dc magnetization case, the torque behavior starts deviating from the normal paramagnetic one at cooling below  $T_{\text{MI}}$ . Fig. 1(b) shows examples of field-dependent torque recorded at different field directions within the  $a^*b$ -plane;  $\beta$  is the angle between the field direction and the  $a^*$ -axis.

The most interesting feature arising below the MI transition temperature is a sharp kink observed in the angular range  $-20^\circ \lesssim \beta \lesssim 20^\circ$ , at  $\mu_0 H \geq 7$  T. By contrast to the monotonic torque component periodic as  $\sin 2(\beta - \beta_0)$ , ( $\beta_0 = 85^\circ$ ), the kink exhibits a periodicity with  $\text{sgn} \beta \cos \beta$ . The position of the kink on the field scale is minimum at  $H \parallel a^*$  and shifts to higher

<sup>1</sup>The work was supported by the DFG-RFBR grant RUS 113/926/0

<sup>2</sup>Institute of Solid State Physics, Rus. Ac. Sci., 142432 Chernogolovka, Russia

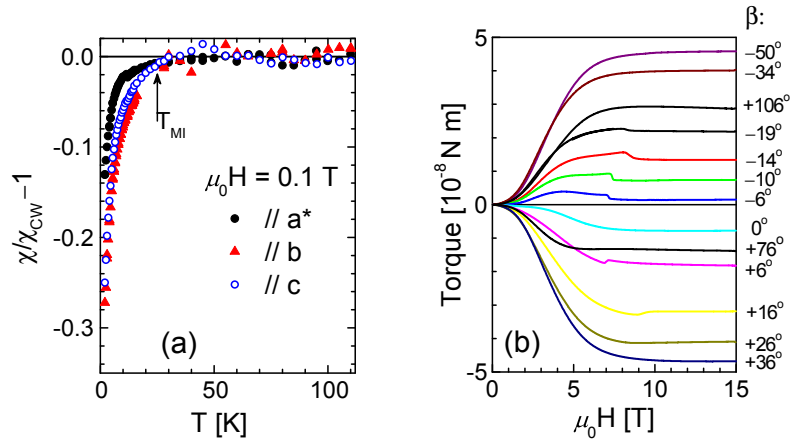


**Figure 1:** (a) Relative deviation of  $\chi$  from the Curie-Weiss value  $\chi_{CW}$  as a function of temperature, at a field  $\mu_0 H = 0.1$  T parallel to the  $a^*$ -,  $b$ -, and  $c$ -axes. The arrow points to the metal-insulator transition temperature; (b) Field dependence of the  $c$ -axis torque at  $T = 1.5$  K at different angles  $\beta$  between the field direction and  $a^*$  (normal to conducting layers).

fields at increasing  $|\beta|$ . Furthermore, this feature displays a significant hysteresis with respect to the field sweep direction. This behavior leads us to consider the kink as a manifestation of a spin flop from a preferential orientation close to the  $a^*$  axis in a magnetically ordered system.

It is important that neither of the magnetization principal axes of the  $Mn^{2+}$  network lies near the  $a^*$  direction. We, therefore, speculate that the kink is related to another magnetic subsystem, namely, to localized  $\pi$ -electron spins in BETS layers. Indeed, if the MI transition is caused by the Mott instability [4], one can expect the spins associated with the localized  $\pi$  electrons to be antiferromagnetically ordered. While we currently have no information about the principal axes of the  $\pi$ -electron spin system, it is likely that one of them is along  $a^* \perp bc$ . The size of the kink,  $\sim 10$  times smaller than the maximum torque in Fig. 1(b), is also consistent with what one would expect as a contribution from  $\pi$  electrons on BETS molecules.

Summarizing the obtained results, we suggest the following scenario. The MI transition is caused by the Mott instability and leads to an AF ordering of  $\pi$ -electron spins in BETS layers. The latter, in turn, stimulates ordering of  $3d$  spins of  $Mn^{2+}$  in anion layers. However, the triangular arrangement of manganese ions in the layers causes a frustration, thus obstructing the usual Néel ordering in this magnetic subsystem. Further experiments including NMR and high-pressure magnetization measurements would be very useful in verifying the proposed scenario and better elucidating the interplay between the charge and spin degrees of freedom in this system.

## References

- [1] L. Brossard, R. Clerac, C. Coulon, M. Tokumoto, T. Ziman, D. Petrov, V. N. Laukhin, M. J. Naughton, A. A. F. Goze, A. Kobayashi, H. Kobayashi, and P. Cassoux, *Eur. Phys. J. B* **1**, 439 (1998).
- [2] S. Uji, H. Shinagawa, T. Terashima, T. Yakabe, Y. Terai, M. Tokumoto, A. Kobayashi, H. Tanaka, and H. Kobayashi, *Nature* **410**, 908 (2001).
- [3] N. D. Kushch, E. B. Yagubskii, M. V. Kartsovnik, L. I. Buravov, A. D. Dubrovskii, A. N. Chekhlov, and W. Biberacher, *J. Am. Chem. Soc.* **130**, 7238 (2008).
- [4] V. N. Zverev, M. V. Kartsovnik, W. Biberacher, S. S. Khasanov, R. P. Shibaeva, L. Ouahab, L. Toupet, N. D. Kushch, E. B. Yagubskii, and E. Canadell, *Phys. Rev. B* **82**, 155123 (2010).

## AC Susceptibility of $\text{YbRh}_2\text{Si}_2$

*E. Schubert*  
*L. Steinke*<sup>1,2</sup>

$\text{YbRh}_2\text{Si}_2$ , a special Heavy-Fermion compound, shows quite unconventional behavior around a quantum critical point (QCP) at 60 mT. A QCP marks a continuous phase transition at  $T = 0\text{K}$  with pronounced deviations from the Landau Fermi liquid state which is usually present in metals. It can be reached, e.g., by suppressing magnetic order by pressure, through doping, and in some cases by a magnetic field.  $\text{YbRh}_2\text{Si}_2$  is a case where an antiferromagnetic phase below 70 mK can be tuned through a QCP by a magnetic field of only 60 mT. To find the thermodynamic ground state of this interesting compound we have studied it at the lowest possible temperatures already during the last two years. These measurements were continued, and in the present work we included AC magnetization experiments with a modified rf SQUID magnetometer in low magnetic fields (less than 2.5 mT) and again at temperatures down to 800  $\mu\text{K}$ .

The AC measurements with the existing magnetometer could be done only at relatively small frequencies. The upper limit is given by the shortest time constant of the SQUID electronic and is 100 Hz. Most data were taken at 17.3 Hz and 37.3 Hz applied through an additional coil inside the magnetometer. A DC magnetic field could be superimposed to the AC excitation component by an outer coil and the AC signal was detected by a digital two-channel Lock-In amplifier yielding the in-phase and the out-of-phase components. The DC magnetization was recorded simultaneously via the SQUID electronics. Data were taken in different fields and with different frequencies. Best results were obtained using a 17.3 Hz modulation.

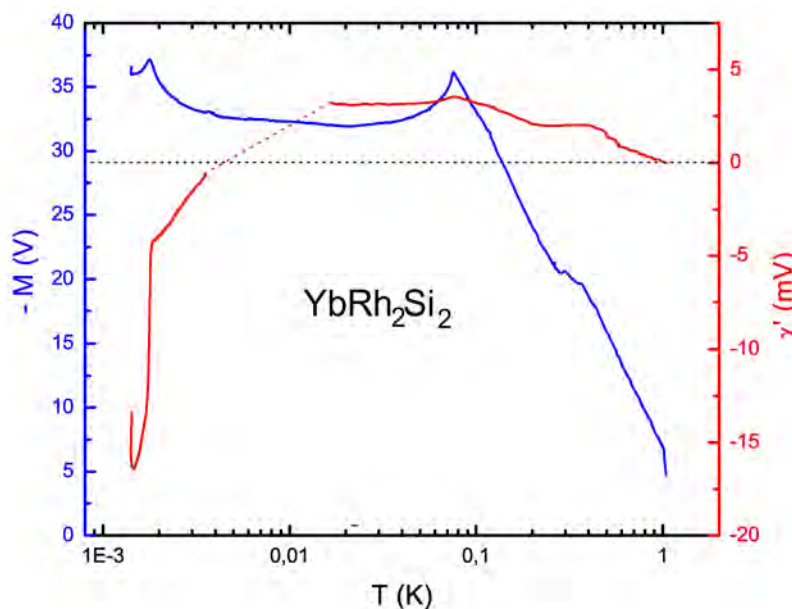


**Figure 1:** DC and AC susceptibility of  $\text{YbRh}_2\text{Si}_2$  in earth field (0.06 mT). The blue curve shows the DC component, the red one the in-phase AC component  $\chi'$ . Units are given in the output voltage of the respective detectors.

The result for the most interesting case is shown in Fig. 1. At 2.2 mK, the transition temperature of the A phase, a sharp decrease of  $\chi'$  extends to negative values which indicates superconducting contributions. But already in fields above 0.1 mT this feature is absent. Since magnetization curves in previous experiments had not shown negative values (no shielding effect) these superconducting contributions cannot come from volume superconductivity but are indicative of weak superconducting fluctuations. Nevertheless they show up at small

<sup>1</sup>Max-Planck Institut für Chemische Physik fester Stoffe, Dresden, Germany.

<sup>2</sup>We acknowledge financial support of this work by the Max-Planck Institut für CPFS Dresden.

fields and temperatures. On the other hand, they cannot be responsible for the whole A and B phases which must have a different origin. Fig. 2 shows the combined results of our previous and present measurements. Inside the AF region there are two phases A and B which start at 2.2 mK and 15 mK, respectively, and extend to 5 mT and 60 mT, respectively. Inside the A-phase there is the small region of weak superconductivity mentioned above.

In summary, we have continued experiments to characterize the two newly found phases in the Heavy Fermion compound  $\text{YbRh}_2\text{Si}_2$ . It seems clear that the phases are superconducting only in a very small T-B region and the superconductivity is of a weak, fluctuating nature. The A phase is apparently the ground state of the Kondo lattice system which starts around 10 K. A possible szenario is that around 15 mK the Kondo effect

begins to break down and the increasing (because less efficiently quenched moments lead to the observed increase in DC magnetization (see blue curve in Fig. 1). The recovered moments then order antiferromagnetically in the A-phase, the B-phase being a precursor of that phase, possibly with a different spin structure. The A-phase is - as the 70 mK antiferromagnetic phase - suppressed by the magnetic field of 60 mK at the QCP.

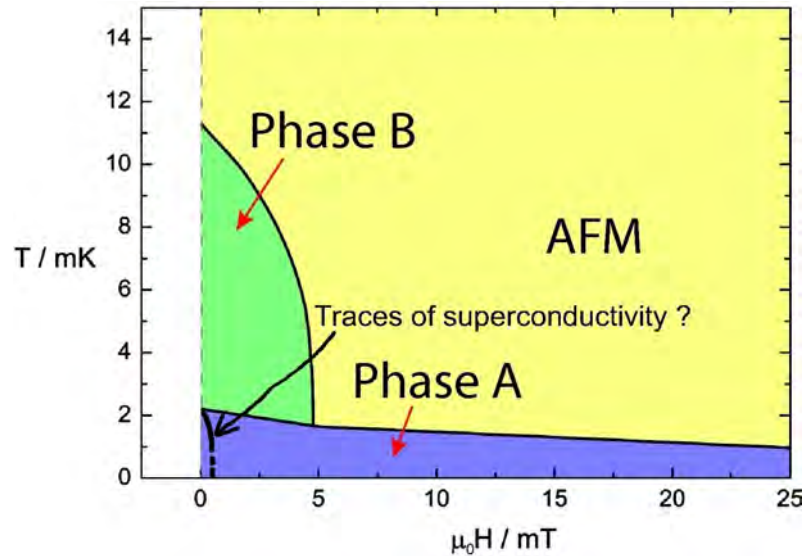
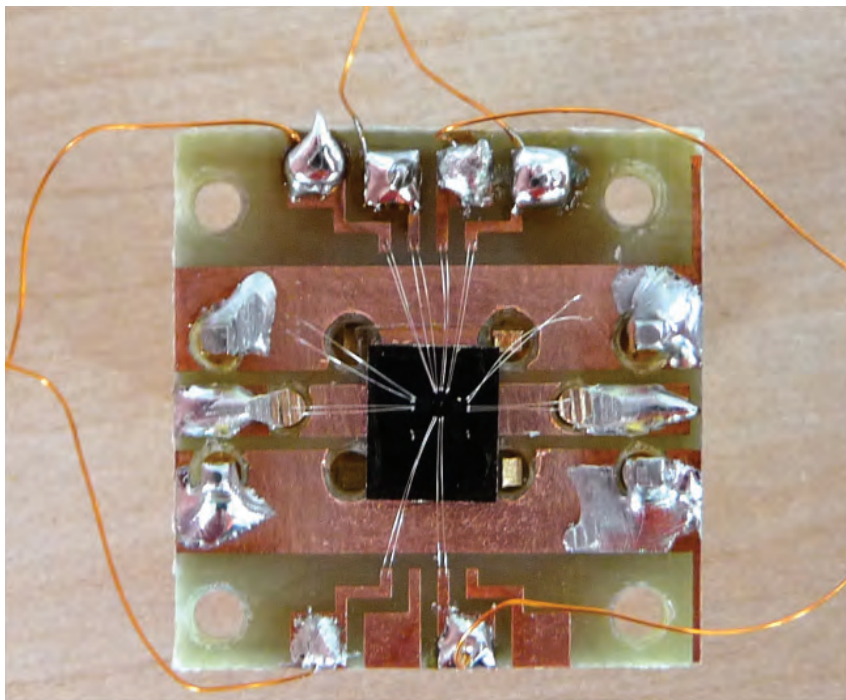


**Figure 2:** Resulting phase diagram for  $\text{YbRh}_2\text{Si}_2$ . At very small fields and temperatures a small region of superconducting fluctuations is found. The nature of the A and B phases is not clear, so far. A breakdown of the Kondo effect an subsequent antiferromagnetic ordering of localized spins seems to be the most plausible explanation

## Application–Oriented Research



Sample for surface acoustic wave (SAW) spin mechanics experiments bonded on a printed circuit board chip carrier. The wires to the top and bottom bond pads provide contacts to a Hall-bar-shaped ferromagnetic film, the other to the interdigital transducers for the generation and detection of SAWs.



## A Superconducting $180^\circ$ Hybrid Ring Coupler for Circuit Quantum Electrodynamics

*E. Hoffmann, F. Deppe, T. Niemczyk, E. P. Menzel, G. Wild, H. Huebl, M. Mariani, T. Weisł, A. Marx, R. Gross*<sup>1</sup>  
*T. Wirth, A. Lukashenko, A. V. Ustinov*<sup>2</sup>  
*A. P. Zhuravel*<sup>3</sup>

In circuit quantum electrodynamics (QED) [1], standing-wave quantum microwave light has been characterized with unprecedented accuracy via its interaction with superconducting quantum circuits [2]. Inspired by these developments, experiments on the quantum properties of microwaves propagating in open transmission lines have recently become an important research focus at the WMI [3–6]. In this context, it is highly desirable to adapt and extend well-established techniques from quantum optics to the world of superconducting microwave circuits. A paradigmatic example is an, ideally lossless, beam splitter, which is of fundamental importance in many quantum optics experiments. In the microwave regime, an equivalent device is the  $180^\circ$  hybrid ring. It is entirely based on interference effects and usually realized as normal conductive device. However, since for circuit QED experiments the on-chip integration of a beam splitter with the quantum circuit under test is favorable in order to minimize undesired reflections and interconnect losses, we designed, fabricated and characterized superconducting hybrid rings [6].

Our devices have a microstrip architecture and are fabricated from niobium (thickness: 200 nm) on silicon and sapphire substrates. As shown in Fig. 1, the beam splitter consists of a superconducting ring with four signal ports. The circumference of the ring determines the center frequency  $f_0$  (in our case  $\approx 6$  GHz). An input signal of frequency  $f$  incident at port one (or three) is split into its clockwise and counterclockwise propagating components which interfere constructively (3 dB coupling) at ports two and four, whereas they interfere destructively (isolation) at ports three and one. When two signals are applied to port one and port three, their sum and difference is present at port two and four, respectively. For the characterization of the microwave properties, the chip is mounted inside a gold-plated copper box in a  $^4\text{He}$ -cryostat.

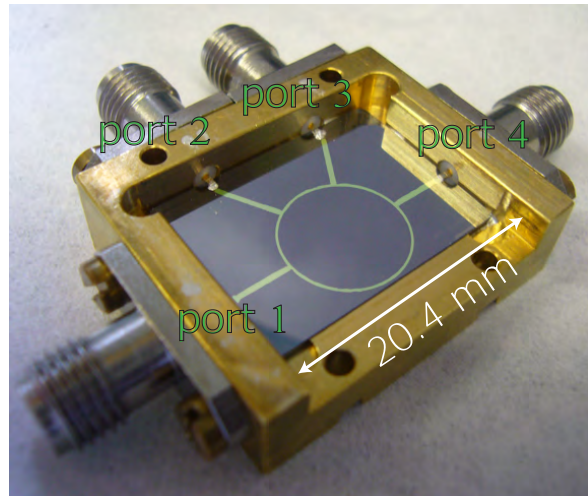


**Figure 1:** A Nb hybrid ring fabricated on a silicon substrate is mounted inside the sample box.

We recorded the coupling and isolation properties from seven (four) different hybrid rings fabricated on silicon (sapphire) substrates, each one remeasured several times to test the reproducibility. The S-parameter measurements of our hybrid rings are shown in Figs. 2(a)-(d), where the two additional ports are terminated into  $50\ \Omega$  right at the sample box. Figure 2(a)

<sup>1</sup>We acknowledge financial support by the German Research Foundation through SFB 631 and the German Excellence Initiative via NIM.

<sup>2</sup>Karlsruher Institut für Technologie (KIT), Physikalisches Institut, Karlsruhe, Germany

<sup>3</sup>B. I. Verkin Institute for Low Temperature Physics and Engineering, National Academy of Sciences of Ukraine, Kharkov, Ukraine

and Fig. 2(c) display the  $S$ -parameters for constructive interference at the respective output port. For both substrate materials we find a coupling magnitude of  $-3.3 \pm 0.2$  dB at the center frequency  $f_0$  as expected for a  $-3$  dB beam splitter. Within the 2 GHz-band centered at  $f_0$ , the coupling magnitude is in the range of  $-3.5 \pm 0.5$  dB. The isolation is shown in Fig. 2(b) and Fig. 2(d) for sapphire and silicon substrates, respectively. In both cases, the isolation magnitude exceeds  $-15$  dB within the 2 GHz-band centered at  $f_0$ , showing the excellent performance of the hybrid rings. We note that despite the  $\text{SiO}_2$  coating of the silicon substrate, the performance of our hybrid rings is robust with respect to dielectric losses. In some devices, we find characteristic changes in the transmission data upon remounting. As shown in Fig. 2(d), the frequency of the maximum isolation may shift and a “hump” may appear. Concurrently, the coupling spectra may become asymmetric and their magnitudes at the center frequency may vary slightly as indicated in Fig. 2(c). The likely origin of these features are reflections at the contact between the superconducting on-chip feed lines and the normal conducting microwave connectors, which affect the interference pattern in the ring. In the following, we visualize the effects of these reflections using low temperature laser scanning microscopy (LTLSM) [6, 7].

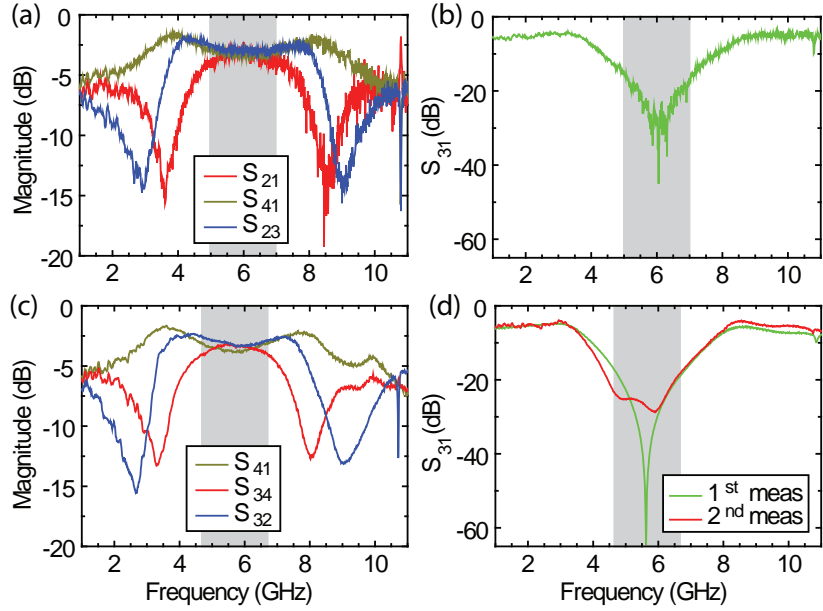


**Figure 2:** Typical transmission data for hybrid rings on sapphire [(a), (b), no averaging] and silicon [(c), (d), 20 curves averaged] substrates at 4.2 K. Input power:  $-40$  dBm. Grey area: frequency band for specifications given in the text. (d) Typical effect of sample remounting.

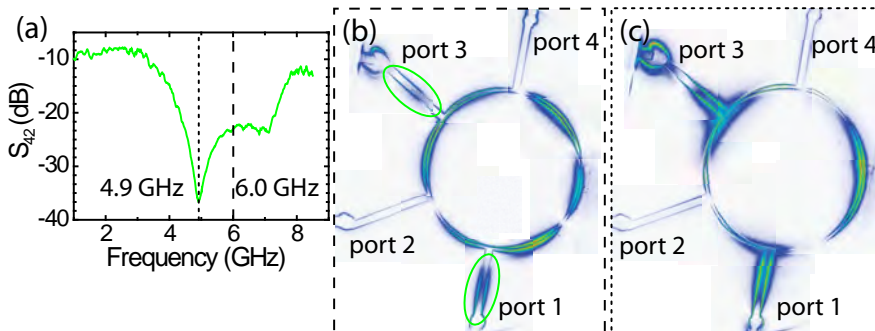


**Figure 3:** LTLSM microscopy of the hybrid ring. (a) Integral  $S_{42}$ -isolation measured at 4.2 K with a network vector analyzer attached to the LTLSM apparatus. (b) LTLSM data taken at 6 GHz (“hump”-frequency; color code: transmission magnitude). (c) LTLSM data taken at 4.93 GHz (maximum isolation).

sample [see Fig. 3(a)] clearly shows the combination of a “hump” and a shifted minimum at 4.93 GHz. In Fig. 3(b), the spatially resolved transmission magnitude at the “hump”-frequency is displayed. First, we notice maxima in the feed lines indicating standing waves caused by reflections at the connectors. Second, the electric field maxima and minima on the ring are

With a signal of frequency  $f_0$  incident at port two, the interference in the ring is expected to lead to three maxima (two of them located at ports one and three) and three minima (two of them located at ports two and four) for an ideal device. However, the transmission  $S_{42}$  of our sample

shifted from their expected positions. Nevertheless, there remains a significant isolation between ports two and four because the shift is relatively small. Third, when changing the excitation frequency to the isolation maximum at 4.93 GHz, the ideal interference pattern is restored in the ring as shown in Fig. 3(c). We note that there is still a significant signal in the feed lines due to the reflections from the connectors.

In conclusion, we have fabricated superconducting  $180^\circ$  hybrid ring couplers on both sapphire and silicon substrates. In a 2 GHz-band centered at 6 GHz, the devices show an almost ideal coupling of  $-3.5 \pm 0.5$  dB and an isolation of at least  $-15$  dB. The observed imperfections are clearly attributed to remaining reflections at the contacts between the superconducting on-chip feed lines and the normal conducting microwave connectors, demonstrating the importance of proper mounting. The performance of our hybrid rings is suitable for further experiments with propagating quantum microwaves.

## References

- [1] A. Wallraff, D. Schuster, A. Blais, L. Frunzio, R.-S. Huang, J. Majer, S. Kumar, S. Girvin, and R. Schoelkopf, *Nature* **431**, 162 (2004).
- [2] M. Hofheinz, H. Wang, M. Ansmann, R. C. Bialczak, E. Lucero, M. Neeley, A. D. O'Connell, D. Sank, J. Wenner, J. M. Martinis, and A. N. Cleland, *Nature* **459**, 546 (2009).
- [3] M. Mariani, M. J. Storcz, F. K. Wilhelm, W. D. Oliver, A. Emmert, A. Marx, R. Gross, H. Christ, and E. Solano, arXiv:cond-mat/0509737 (2005).
- [4] E. P. Menzel, F. Deppe, M. Mariani, M. A. Caballero, A. Baust, T. Niemczyk, E. Hoffmann, A. Marx, E. Solano, and R. Gross, *Phys. Rev. Lett.* **105**, 100401 (2010).
- [5] M. Mariani, E. P. Menzel, F. Deppe, M. A. Caballero, A. Baust, T. Niemczyk, E. Hoffmann, E. Solano, A. Marx, and R. Gross, *Phys. Rev. Lett.* **105**, 133601 (2010).
- [6] E. Hoffmann, F. Deppe, T. Niemczyk, T. Wirth, E. P. Menzel, G. Wild, H. Huebl, M. Mariani, T. Weis, A. Lukashenko, A. P. Zhuravel, A. V. Ustinov, A. Marx, and R. Gross, *Appl. Phys. Lett.* **97**, 222508 (2010).
- [7] A. Zhuravel, A. Sivakov, O. Turutanov, A. Omelyanchouk, S. M. Anlage, A. Lukashenko, A. Ustinov, and D. Abramov, *Fiz. Nizk. Temp.* **32**, 775 (2006).

## Absence of Both Ferromagnetism and $p$ -type Conductivity in (Li,Ni)-Codoped ZnO Thin Films

D. Venkateshvaran, M. Althammer, S.T.B. Goennenwein, M. Opel, R. Gross<sup>1</sup>  
S.E. Kumar, M. S. Ramachandra Rao<sup>2,3</sup>

In the past years, the research on zinc oxide (ZnO) underwent an astonishing revival. This was accompanied by a rapid expansion of the field towards magnetism on the one hand and device physics for (opto-/spin-)electronic applications on the other. Although its properties have been extensively studied for more than 50 years, the application of ZnO in semiconducting electronics is prevented because of the difficult control of its electric properties. On the one hand, ZnO crystals are natively always  $n$ -type. Stable  $p$ -doping is difficult to achieve and has been a matter of extensive debate and research until today. Both group-I (replacing Zn) and group-V elements (replacing O) are discussed as acceptors for this wide bandgap semiconductor. On the other hand, the possibility to realize ZnO-based dilute magnetic semiconductors by transition metal doping is still a matter of controversy, as pointed out in the annual report of 2007.

Following a recent report [1], we studied the possibility of (Li,Ni)-codoping to establish ferromagnetism together with  $p$ -type conductivity in ZnO. In close collaboration with M.S.R. Rao (IIT Madras, India), we deposited thin films from stoichiometric targets with compositions  $\text{Zn}_{0.98-x}\text{Li}_x\text{Ni}_{0.02}\text{O}$  ( $x = 0, 0.02, 0.05, 0.09$ ) on (0001)-oriented  $\text{Al}_2\text{O}_3$  substrates in  $\text{O}_2$  atmosphere at  $400^\circ\text{C}$  under two different growth conditions: For the first set of samples, we used the parameters which we found optimum for the growth of high-quality, undoped ZnO thin films (laser fluence:  $1\text{ J/cm}^2$ , repetition rate:  $1\text{ Hz}$ , pressure:  $1 \times 10^{-3}\text{ mbar}$ ). For the second set, we applied the parameters reported in Ref. [1] for  $p$ -type conductivity plus ferromagnetism ( $2.7\text{ J/cm}^2$ ,  $10\text{ Hz}$ ,  $3.5 \times 10^{-2}\text{ mbar}$ ). The thin films grown at lower fluence and oxygen pressure show excellent structural quality. For all  $x$  values, the x-ray diffraction diagrams do not indicate any secondary phases nor metallic Ni precipitates. A selection of the data is compiled in Fig. 1. The (0002) and (0004) reflections from the  $\text{Zn}_{0.98-x}\text{Li}_x\text{Ni}_{0.02}\text{O}$  thin films are clearly visible with an intensity close to the (0006) and (00012) reflections from the  $\text{Al}_2\text{O}_3$  substrate. The epitaxial films show a nearly perfect in-plane orientation as demonstrated by  $\phi$ -scans of the (10 $\bar{1}$ 1) reflections [see inset in Fig. 1(a)] which appear every  $60^\circ$ . Moreover, the films display a low mosaic spread as

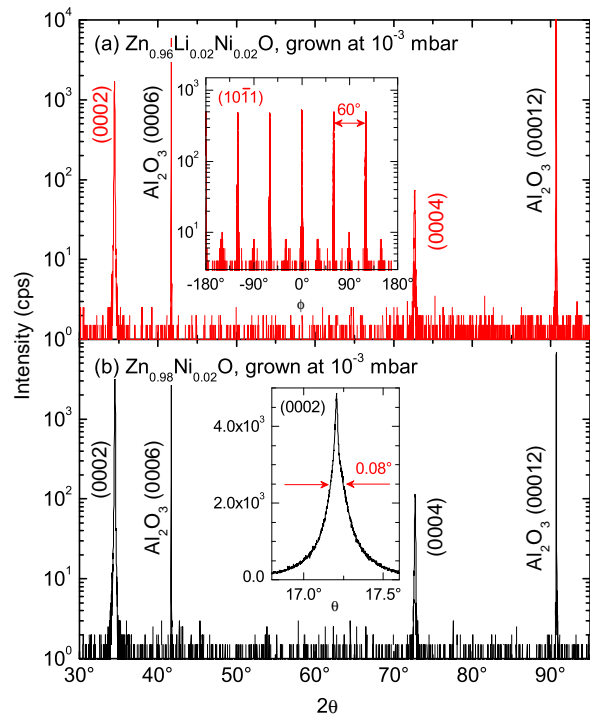


**Figure 1:** X-ray diffraction diagrams at room temperature from thin films of  $\text{Zn}_{0.98-x}\text{Li}_x\text{Ni}_{0.02}\text{O}$ , deposited on  $\text{Al}_2\text{O}_3$  substrates in  $\text{O}_2$  atmosphere at  $10^{-3}\text{ mbar}$  using our optimum WMI growth parameters, with (a)  $x = 2\%$  and (b)  $x = 0$ . The insets show (a) a  $\phi$ -scan of the (10 $\bar{1}$ 1) reflection and (b) a rocking curve of the (0002) reflection.

<sup>1</sup>This work is supported by the German Research Foundation via the priority program SPP 1285.

<sup>2</sup>Materials Science Research Centre, Indian Institute of Technology Madras, Chennai, India

<sup>3</sup>We acknowledge financial support by DAAD.

indicated by a narrow full width at half maximum (FWHM) of the rocking curves of the (0002) reflections down to  $0.08^\circ$  [see inset in Fig. 1(b)]. The films grown at higher fluence and oxygen pressure [1], however, display a lower structural quality (not shown here). Their FWHM of the rocking curve of the same reflection is by a factor of 4 larger indicating a higher mosaic spread, and the intensities of the film reflections are by one order of magnitude below those of the first set of samples.

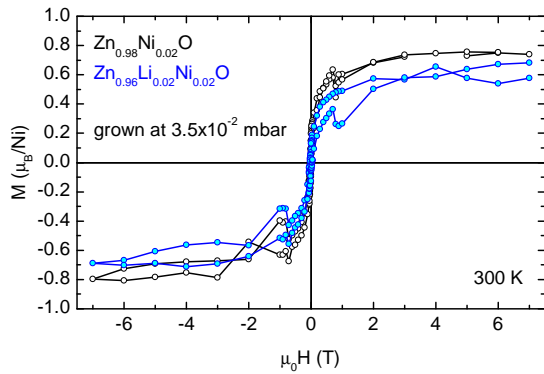


**Figure 2:** Room-temperature SQUID magnetization measurements from thin films of  $\text{Zn}_{0.98-x}\text{Li}_x\text{Ni}_{0.02}\text{O}$ , deposited in an  $\text{O}_2$  atmosphere of  $3.5 \times 10^{-2}$  mbar using the growth parameters reported in Ref. [1].

( $2 \mu_B$ ). This is a strong indication that, again, nanometer-sized metallic Ni precipitates are responsible for the observed room-temperature magnetism in these samples. Further magnetic characterization of the  $\text{Zn}_{0.98-x}\text{Li}_x\text{Ni}_{0.02}\text{O}$  thin films is in progress.

To clarify the issue of  $p$ -type conductivity and unambiguously identify the sign of the charge carriers, we performed thermopower measurements to determine the Seebeck coefficient  $S$  rather than Hall effect measurements. The latter are difficult to interpret if more than one conduction band is involved, or for hopping conductivity. For all  $\text{Zn}_{0.98-x}\text{Li}_x\text{Ni}_{0.02}\text{O}$  thin film samples studied here, regardless of their different growth parameters, we found  $S < 0$  at room temperature indicating  $n$ -type conductivity (cf. Fig. 3). Within experimental error,  $S$  ranges between  $-400 \mu\text{V}/\text{K}$  and  $-900 \mu\text{V}/\text{K}$  with smaller absolute values corresponding to lower Li concentrations.

In summary, we could not confirm  $p$ -type conductivity nor ferromagnetism in any of the investigated (Li,Ni)-substituted ZnO thin films.

## References

- [1] E. S. Kumar, S. Venkatesh, and M. S. R. Rao, Appl. Phys. Lett. **96**, 232504 (2010).
- [2] M. Opel, K.-W. Nielsen, S. Bauer, S. Goennenwein, R. Gross, J. Cezar, D. Schmeisser, J. Simon, and W. Mader, Eur. Phys. J. B **63**, 437 (2008).
- [3] A. Ney, M. Opel, T. Kaspar, V. Ney, S. Ye, K. Ollefs, T. Kammermeier, S. Bauer, K.-W. Nielsen, S. Goennenwein, M. Engelhard, S. Zhou, K. Potzger, J. Simon, W. Mader, S. Heald, J. Cezar, F. Wilhelm, A. Rogalev, R. Gross, and S. Chambers, New J. Phys. **12**, 013020 (2010).

The magnetic properties of the first sample set grown at low fluence/oxygen pressure are still under investigation. The  $M(H)$  loops of the second sample set grown at high fluence/oxygen pressure [1] show an “S”-shaped behavior at room temperature (cf. Fig. 2) which is reminiscent of our previous results for superparamagnetic  $\text{Zn}_{0.95}\text{Co}_{0.05}\text{O}$  [2, 3]. Again, comparing  $M(T)$  measurements after field cooling and zero-field cooling provides evidence for blocking behavior. The saturation magnetic moment at 7 T does not increase significantly when cooling from 300 K to 5 K. Interestingly, its value is around  $0.7 \mu_B$  per Ni (with  $\mu_B$  representing the Bohr magneton) and, hence, very close to the bulk value of metallic Ni ( $0.6 \mu_B$ ), but far from that of  $\text{Ni}^{2+}$  ions

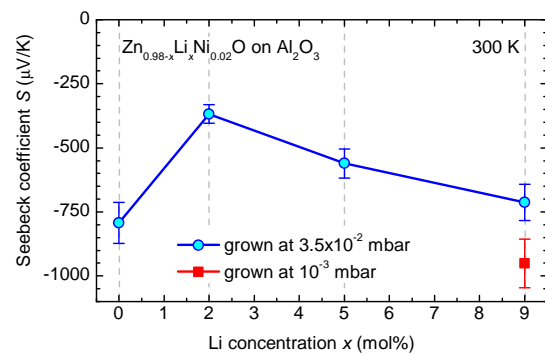


**Figure 3:** Seebeck coefficients at room temperature from thin films of  $\text{Zn}_{0.98-x}\text{Li}_x\text{Ni}_{0.02}\text{O}$ , deposited in  $\text{O}_2$  atmosphere using two different sets of growth parameters.

## Magnetic Microstructure and Magnetotransport in $\text{Co}_2\text{FeAl}$ Heusler Compound Thin Films

M. Weiler, F. D. Czeschka, R. Gross, S. T. B. Goennenwein<sup>1</sup>  
 I.-M. Imort, G. Reiss, A. Thomas<sup>2,3</sup>  
 G. Woltersdorf<sup>4</sup>

Cobalt-based Heusler compounds are an interesting class of materials for spintronic applications due to their predicted 100% spin-polarization [1] and their Curie temperature well in excess of room temperature [2]. Furthermore, tunneling magnetoresistance (TMR)-ratios exceeding 1000% have been reported [3], making Heusler-based devices attractive for magnetic data storage applications. However, while the TMR properties have been vigorously investigated, much less is known about the magnetic microstructure and its impact on the magnetotransport properties of Heusler thin films. This is all the more surprising as the modeling of magnetoresistive effects such as TMR, giant magnetoresistance, anisotropic magnetoresistance [4] or the angle dependent magnetoresistance [5] are usually based on the assumption of a macrospin, i.e., a magnetic single domain state.

We carried out simultaneous magnetotransport and spatially resolved magneto optical Kerr effect (MOKE) measurements in  $\text{Co}_2\text{FeAl}$  Heusler thin films at room temperature. The thin films were prepared by DC- and RF-sputtering on a MgO (001) substrate at a base pressure of  $1 \times 10^{-7}$  mbar. We here focus on a sample consisting of 5 nm MgO, 50 nm  $\text{Co}_2\text{FeAl}$  and 1.8 nm MgO annealed for one hour at 500 °C. The sample was patterned into the Hall bar geometry shown in Fig. 1 by optical lithography and Ar ion beam etching. As discussed in more detail in the contribution by M. Althammer *et al.* (p. 65), the sample shows dominantly cubic magnetic anisotropy in the film plane, with easy axes (e.a.) along the crystalline [110] and  $[\bar{1}10]$  directions which are parallel and perpendicular to the main Hall bar (along y and x), respectively.

The MOKE images shown in Fig. 2 were recorded in the longitudinal MOKE configuration, schematically depicted in Fig. 1. S-polarized light ( $\lambda = 455$  nm) is used to illuminate the sample and the p-polarized component of the reflected light is imaged with a CCD-camera. This MOKE setup allows for a lateral spatial resolution of  $\approx 10$   $\mu\text{m}$ . Prior to the image acquisition, we prepared the sample in a magnetically saturated state by applying  $\mu_0 H = -30$  mT along x and iteratively adjusted the analyzer A and polarizer P to obtain minimal total intensity on the CCD. The analyzer was subsequently rotated  $1^\circ$  out of extinction for the measurement.

Sweeping the magnetic field up to  $\mu_0 H = +30$  mT and back to  $\mu_0 H = -30$  mT, MOKE images were recorded at consecutive field points. To obtain magnetic contrast, a reference image

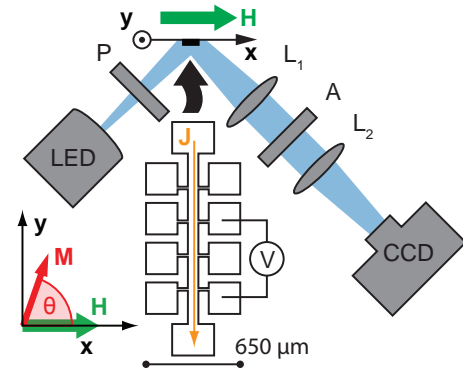


**Figure 1:** Sketch of the MOKE setup and the sample. The MOKE signal is spatially resolved with a CCD-camera and the magnetoresistance is recorded in a four point measurement between the indicated contact pads.  $\ominus$  denotes the magnetization  $\mathbf{M}$  orientation with respect to the x axis.

<sup>1</sup>Financial support via the German Research Foundation, Project No. GO 944/3-1, and the German Excellence Initiative via the Nanosystems Initiative Munich (NIM) is gratefully acknowledged.

<sup>2</sup>Fakultät für Physik, Universität Bielefeld, Bielefeld, Germany

<sup>3</sup>I.-M.I. and A.T. are supported by a MIWF junior researcher grant.

<sup>4</sup>Department of Physics, Universität Regensburg, Regensburg, Germany

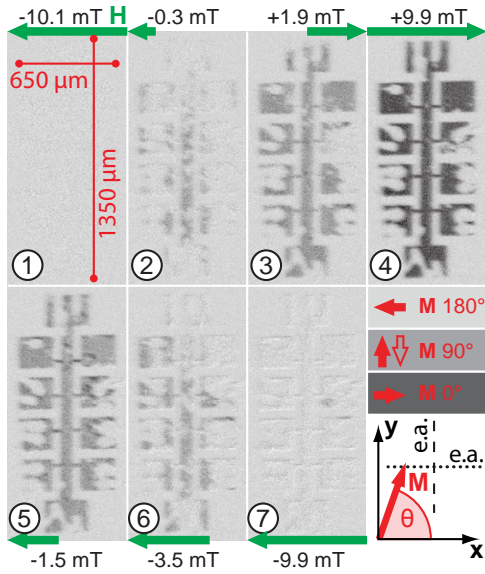


**Figure 2:** Selected spatially resolved MOKE images. The shading represents the  $\mathbf{M}$ -orientation in each domain, as indicated in the lower right.

Figure 3(a) shows the normalized MOKE intensity obtained upon integrating the MOKE signal within the entire Hall bar region. The two-step shape characteristic for cubic magnetic anisotropy is clearly evident. The magnetic fields at which the MOKE images of Fig. 2 were recorded are indicated by red crosses, such that the spatially resolved domain contrast of Fig. 2 can be directly compared to the integral magnetization loop in Fig. 3(a). For comparison of our MOKE and magnetotransport data, we also integrated the MOKE intensity in a region of interest (ROI) corresponding to the region probed by magnetotransport. The resulting  $I(H)$  is shown in Fig. 3(b). It again clearly exhibits the dual switching behavior indicative of cubic magnetic anisotropy. To extract an effective, average magnetization direction from the MOKE images, we calculate the mean magnetization direction  $\bar{\mathbf{M}}$  in the ROI as a function of  $\mu_0 H$ , assuming that  $\bar{\mathbf{M}}$  is parallel to  $\mathbf{H}$  for  $\mu_0 |H| = 30$  mT. More precisely, we take the  $\bar{\mathbf{M}}$  orientation to be  $\Theta_- = 180^\circ$  for  $\mu_0 H = -30$  mT and  $\Theta_+ = 0^\circ$  for  $\mu_0 H = +30$  mT. This is a valid assumption as the integral MOKE loops displayed in Fig. 3 exhibit hysteresis closure at approx.  $\pm 5$  mT. With the normalized MOKE intensity  $I(H)$  in the ROI as shown in Fig. 3(b), we can now calculate  $\Theta(H) = \arccos[I(H)]$  [6]. The resulting  $\Theta(H)$  is shown in Fig. 4(a). The double switching behavior is again clearly visible, with  $\Theta \approx 90^\circ$  at small absolute values of  $\mu_0 H$ . Hence, we observe  $\bar{\mathbf{M}}$  switching from  $\bar{\mathbf{M}} \parallel -x$  (first e.a., parallel to  $\mathbf{H}$ ) to  $\bar{\mathbf{M}} \parallel y$  (second e.a., perpendicular to  $\mathbf{H}$ ) and subsequent switching to  $\bar{\mathbf{M}} \parallel \mathbf{H}$  again. Note that the L-MOKE measurement geometry is sensitive only to the projection of  $\bar{\mathbf{M}}$  on  $\mathbf{H} \parallel x$ , therefore it is not

recorded in saturation is subtracted from each image. A selection of the resulting difference images is displayed in Fig. 2. At  $-10.1$  mT [image (1)] the sample is still in the magnetically saturated single-domain state so that no magnetic contrast is visible. Upon increasing the external magnetic field strength, domains start to nucleate and propagate [images (2) and (3)]. In image (3) most parts of the Hall bar show identical grey shading, corresponding to  $\mathbf{M}$  along  $y$ , except for the aluminum bond wires visible as white patches on the contact pads. By further increasing  $\mu_0 H$ , the magnetic contrast can be increased once again as visible in the change of the Hall bar shading from grey in image (3) to dark grey in image (4). Dark grey hereby corresponds to  $\mathbf{M} \parallel x$ . This two-step magnetic switching behavior (antiparallel, perpendicular, parallel to  $x$ , see the lower right of Fig. 2) is characteristic for cubic anisotropy. Similar domain states are observed in the magnetic field downsweep [images (5) to (7)].

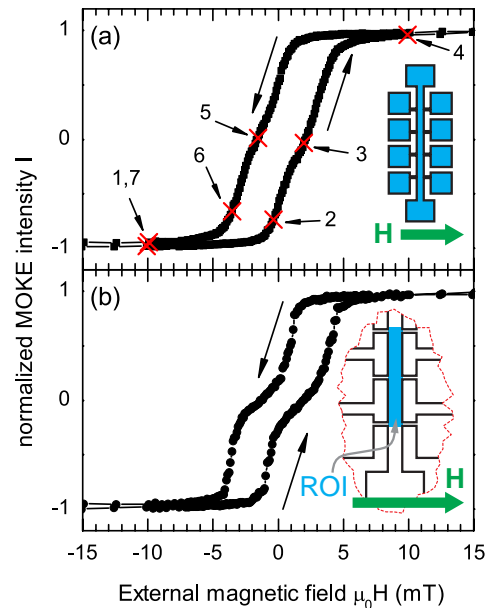


**Figure 3:** (a) MOKE intensity  $I$  integrated over the entire Hall bar and normalized to  $[-1, 1]$  as a function of  $\mu_0 H$ . The numbers correspond to the MOKE images shown in Fig. 2. (b) Normalized  $I(H)$  integrated over the indicated ROI.

possible to discriminate between the energetically degenerate  $\bar{\mathbf{M}}$  orientations  $\Theta = 90^\circ$  and  $\Theta = 270^\circ$ .

Having determined  $\Theta(H)$  we can now calculate the magnetoresistance  $\rho(H)$  expected in the macrospin model and compare it to four point longitudinal magnetotransport data acquired simultaneously to the MOKE images. The magnetotransport measurements were carried out with the contact geometry sketched in Fig. 1 and a current  $J = 5$  mA. The results are shown by the red triangles in Fig. 4(b). The resistivity changes from  $\rho_\perp = 734.1$  n $\Omega$ m at  $\mu_0 H = -30$  mT (negative saturation,  $\mathbf{M} \parallel -\mathbf{x}$ ) to  $\rho_\parallel = 733.2$  n $\Omega$ m at  $\mu_0 H = 2$  mT ( $\mathbf{M} \parallel \mathbf{y}$ ) in the magnetic field upsweep. In the following, we take  $\rho_\perp$  and  $\rho_\parallel$  as the resistivity for  $\bar{\mathbf{M}}$  perpendicular and parallel to  $\mathbf{J}$ , respectively. We calculate the AMR from the effective macrospin  $\bar{\mathbf{M}}$  [cf. Fig. 4(a)] using [7]

$$\rho(H) = \rho_\perp + (\rho_\parallel - \rho_\perp) \cos^2 [\Theta(H) + \Phi] ,$$

where  $\Phi = 270^\circ$  is the angle between the current direction  $\mathbf{J}$  and the x-axis. The result is depicted by the open circles in Fig. 4(b) and shows excellent agreement with the experimental magnetotransport data. This shows that, in  $\text{Co}_2\text{FeAl}$  Heusler compounds, it is possible to model the AMR using a simple macrospin model that neglects the domain wall resistance, although microscopically a complex domain pattern is observed (cf. Fig. 2).

In conclusion, we compared magnetic microstructure and magnetotransport properties in  $\text{Co}_2\text{FeAl}$  Heusler compounds by simultaneously recording spatially resolved magneto optical Kerr effect and magnetotransport data. An effective magnetization orientation (macrospin) corresponding to the spatially averaged microscopic  $\mathbf{M}$  configuration in the region probed by magnetotransport was extracted from the MOKE images. We found that the magnetotransport properties can be quantitatively reproduced assuming that this macrospin determines the magnetoresistance. This shows that the contribution of domain walls to the magnetoresistance is negligible, and opens the path for further investigations of Heusler compound thin films using macrospin-based magnetotransport techniques.

## References

- [1] H. C. Kandpal, G. H. Fecher, and C. Felser, *J. Phys. D: Appl. Phys.* **40**, 1507 (2007).
- [2] S. Trudel, O. Gaier, J. Hamrle, and B. Hillebrands, *J. Phys. D: Appl. Phys.* **43**, 193001 (2010).
- [3] T. Ishikawa, H.-x. Liu, T. Taira, K.-i. Matsuda, T. Uemura, and M. Yamamoto, *Appl. Phys. Lett.* **95**, 232512 (2009).
- [4] W. Thomson, *Proc. R. Soc. Lond.* **8**, 546 (1857).
- [5] W. Limmer, M. Glunk, J. Daeubler, T. Hummel, W. Schoch, R. Sauer, C. Bihler, H. Huebl, M. S. Brandt, and S. T. B. Goennenwein, *Phys. Rev. B* **74**, 205205 (2006).
- [6] W. Gil, D. Görlitz, M. Horisberger, and J. Kötzler, *Phys. Rev. B* **72**, 134401 (2005).
- [7] T. McGuire and R. Potter, *IEEE Trans. Magn.* **11**, 1018 (1975).

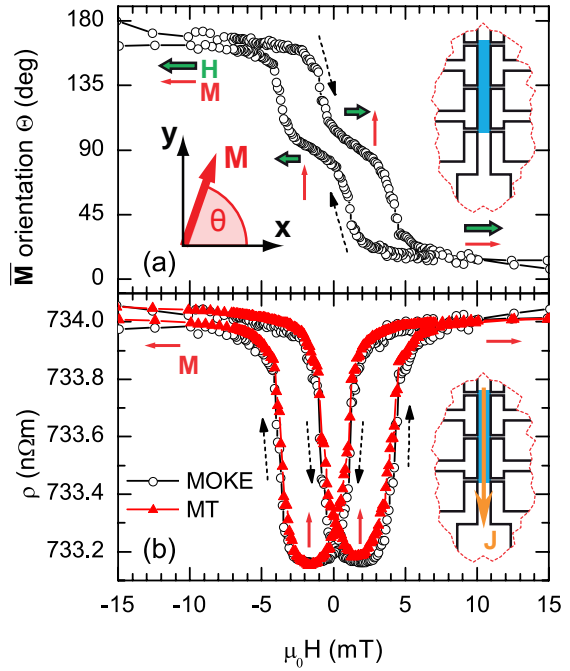


**Figure 4:** (a)  $\bar{\mathbf{M}}$  orientation  $\Theta(H)$  calculated from the integral MOKE intensity in the indicated region of interest. (b) The AMR calculated from  $\Theta(H)$  perfectly traces the experimentally observed  $R(H)$ .

## Magnetoresistance and Crystalline Symmetry in Heusler Compounds

M. Althammer, A. Krupp, M. Opel, R. Gross, S. T. B. Goennenwein<sup>1</sup>  
I.-M. Imort, G. Reiss, A. Thomas<sup>2,3</sup>

In the annual report 2007, we showed that the magnetic anisotropy properties of conductive ferromagnets can be quantitatively determined via anisotropic magnetoresistance (AMR) measurements. The measurement protocol used hereby relies on resistance measurements as a function of the *orientation* of an externally applied magnetic field  $\mathbf{H}$ , for several, constant magnetic field magnitudes  $H$ , respectively. The name angle-dependent magnetoresistance (ADMR) was thus coined for this novel magnetic characterization technique.

The ADMR approach enables the study of the fundamental magnetic properties of single magnetic micro- or nanostructures, since electronic transport experiments at the nano-scale are well established. To date, however, the viability and the power of ADMR has primarily been demonstrated in (Ga,Mn)As thin films, as the magnetoresistive effects in this ferromagnetic semiconductor are comparatively large. In the past year, we have performed systematic ADMR measurements in the ferromagnetic Heusler compound  $\text{Co}_2\text{FeAl}$ , following up on an early report that the AMR in thin  $\text{Fe}_3\text{Si}$  films can be modeled if the effect of crystalline symmetry is taken into account. One important result of our experiments, discussed in more detail in the contribution by M. Weiler *et al.* (see p. 62), is that magnetic domain walls do not significantly contribute to the magnetoresistance of Heusler compounds. This is a prerequisite for ADMR experiments, since the ADMR formalism hinges on the assumption of a macrospin, i.e., of a single (average) magnetization throughout the entire ferromagnetic sample. The second important outcome of our experiments is that the ADMR approach yields a consistent and quantitative description of the AMR in all  $\text{Co}_2\text{FeAl}$  thin films investigated, suggesting that all conductive, ferromagnetic Heusler compounds can be described in this framework.

For the sake of simplicity, we here focus on the 50 nm thick  $\text{Co}_2\text{FeAl}$  thin film sample also discussed in the contribution by M. Weiler *et al.* (see p. 62). For the ADMR experiments, the sample was inserted into an Oxford split coil magnet cryostat system, such that it could be rotated with respect to  $\mathbf{H}$ . As shown in Fig. 1, we typically studied three different rotation planes: (1)  $\mathbf{H}$  in the film plane, i.e., perpendicular to the film surface normal  $\mathbf{n}$ , (2)  $\mathbf{H}$  rotating in a plane perpendicular to the current direction  $\mathbf{j}$ , and (3)  $\mathbf{H}$  rotating in a plane perpendicular to  $\mathbf{t} = \mathbf{n} \times \mathbf{j}$ . We recorded both the resistivity  $\rho_{\text{long}}$  along  $\mathbf{j}$ , as well as  $\rho_{\text{trans}}$  along  $\mathbf{t}$ , as a function of the respective magnetic field orientation  $\alpha$ . As evident from Fig. 1, the  $\rho_{\text{long}}(\alpha)$  and  $\rho_{\text{trans}}(\alpha)$  traces are qualitatively different for the different rotation planes and field magnitudes  $H$ . We model the AMR following the ansatz of Birss *et al.* [1–3]. In this approach, the resistivity tensor is expanded in a power series in the magnetization orientation  $\mathbf{m}$ , taking into account the Onsager relations and the intrinsic symmetry of the magnetic crystal (the von Neumann principle). Considering that the  $\text{Co}_2\text{FeAl}$  thin films investigated here have tetragonal crystal symmetry owing to epitaxial coherency strain, and that  $\mathbf{j}$  is along the in-plane  $[110]$  direction, this yields:

$$\rho_{\text{long}} = \rho_0 + \rho_1 m_j^2 + \rho_2 m_n^2 \quad (1)$$

$$\rho_{\text{trans}} = \rho_6 m_n + \rho_7 m_j m_t. \quad (2)$$

The  $\mathbf{m}$  components ( $m_j$ ,  $m_t$ ,  $m_n$ ) along ( $\mathbf{j}$ ,  $\mathbf{t}$ ,  $\mathbf{n}$ ) are calculated in a Stoner-Wohlfarth approach, assuming that  $\mathbf{m}$  points along a direction of minimal free energy  $F_{\text{tot}}$ . Using

<sup>1</sup>Financial support by the German Research Foundation, Project No. GO 944/3-1, is gratefully acknowledged.

<sup>2</sup>Fakultät für Physik, Universität Bielefeld, Bielefeld, Germany

<sup>3</sup>I.-M.I. and A.T. are supported by a MIWF junior researcher grant.

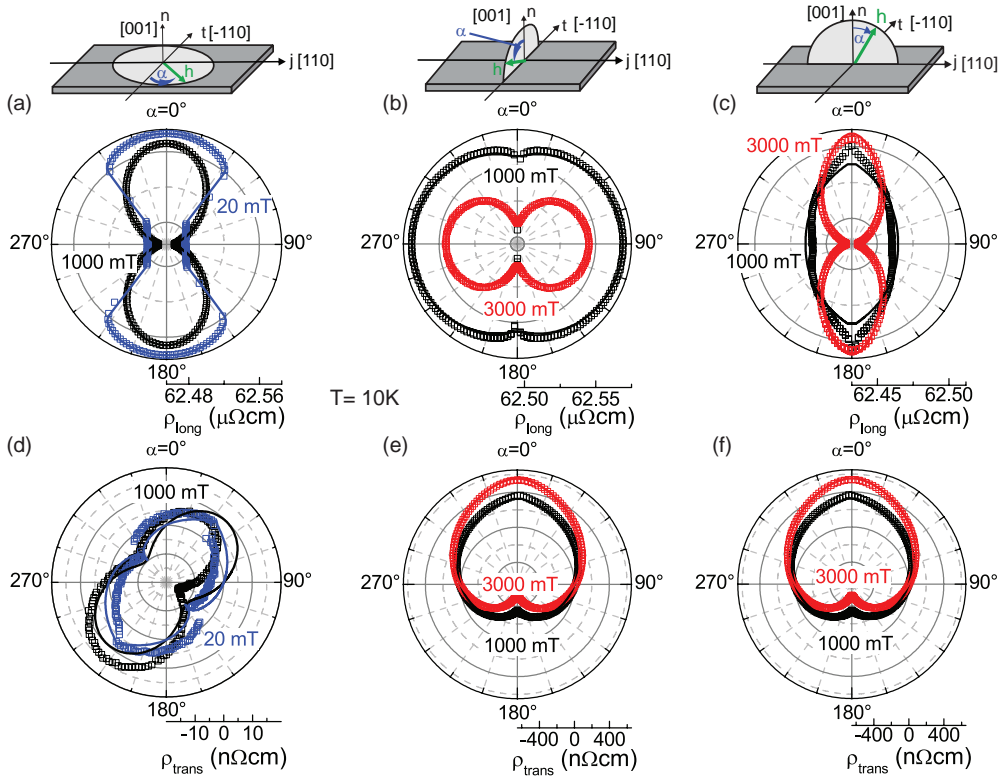


**Figure 1:** Angle dependent magnetoresistance measurements of a 50 nm thin  $\text{Co}_2\text{FeAl}$  film at  $T=10\text{K}$ . (a),(b),(c) depict the measured (symbols) and simulated (lines) longitudinal resistivity as a function of the magnetic field orientation, in the measurement geometries shown above. (d),(e),(f) show the corresponding transverse resistivity, with the experimental data again represented by symbols, while the lines depict the calculated  $\rho_{\text{trans}}$ .

$F_{\text{tot}}/M = -\mu_0 H(\mathbf{m}\mathbf{h}) + B_c(m_x^4 + m_y^4 + m_z^4) + B_{110}\frac{1}{2}(m_x + m_y)^2 + B_{001}m_z^2$ , with the cubic anisotropy field  $B_c = 7\text{ mT}$ , the uniaxial anisotropy fields  $B_{110} = -2.7\text{ mT}$  and  $B_{001} = 820\text{ mT}$ , and  $\rho_0 = 62.6\ \mu\Omega$ ,  $\rho_1 = -52.2\ \text{n}\Omega$ ,  $\rho_2 = -36.2\ \text{n}\Omega$ ,  $\rho_6 = 55.1\ \text{n}\Omega$ ,  $\rho_7 = -19.5\ \text{n}\Omega$ , Eqns. (1) and (2) yield  $\rho_{\text{long}}(\alpha)$  and  $\rho_{\text{trans}}(\alpha)$  shown by the full lines in Fig. 1. The calculated ADMR traces faithfully reproduce the experimental ones. Such an excellent agreement between model and experiment was observed not only for  $T = 10\text{K}$ , but for all temperatures  $5\text{K} \leq T \leq 300\text{K}$  and in all  $\text{Co}_2\text{FeAl}$  films with thicknesses  $20\text{ nm} \leq d \leq 100\text{ nm}$  investigated. Note also that we always found  $\rho_1 < 0$ , which means that  $\rho_{\text{long}}$  is smaller for  $\mathbf{j} \parallel \mathbf{m}$  than for  $\mathbf{j} \perp \mathbf{m}$ . This has also been observed in  $\text{Fe}_3\text{Si}$  [2], and is usually expressed as  $\rho_{\parallel} < \rho_{\perp}$ . This is in contrast to  $\rho_{\parallel} > \rho_{\perp}$  in most ferromagnetic metals, and needs to be considered in microscopic AMR models for Heusler compounds.

In summary, we found that crystalline symmetry characteristically affects the anisotropic magnetoresistance of the Heusler compound  $\text{Co}_2\text{FeAl}$ . As domain walls do not significantly contribute to the magnetoresistance, the magnetic anisotropy can be determined from angle-dependent magnetoresistance measurements. Thus, electric transport experiments give access to a wealth of information on the magnetic properties of ferromagnetic Heusler compounds.

## References

- [1] R. R. Birss, *Symmetry and Magnetism* (North-Holland, Amsterdam, 1964).
- [2] P. K. Muduli, K.-J. Friedland, J. Herfort, H.-P. Schönerr, and K. H. Ploog, *Phys. Rev. B* **72**, 104430 (2005).
- [3] W. Limmer, J. Daeubler, L. Dreher, M. Glunk, W. Schoch, S. Schwaiger, and R. Sauer, *Phys. Rev. B* **77**, 205210 (2008).

## Intercalation and Dynamics of Hydrated Fe<sup>2+</sup> in Vermiculites from Santa Olalla and Ojén

A. Lurf

F. E. Wagner<sup>1</sup>

J. Poyato, J.L. Pérez-Rodríguez<sup>2</sup>

Vermiculites and smectites loaded with Fe<sup>3+</sup> have attracted attention because of their potential application as catalysts, although the uptake of Fe<sup>3+</sup> into the interlayer space of phyllosilicates is a delicate process because the Fe<sup>3+</sup> ions can be maintained in the monomeric hydrated form that is best for ion exchange only at the pH values of the aqueous solution below 1.5, which can lead to a deterioration of the phyllosilicates.

Whereas the insertion of Fe<sup>2+</sup> should be much easier (because of the lower acidity of the hexaquo complex of Fe<sup>2+</sup> and the concomitant lower tendency towards polymerization), the uptake of Fe<sup>2+</sup> into the interlayer space of phyllosilicates has been investigated only recently. In the work presented here we have studied the alteration of vermiculites from Santa Olalla and Ojén (Andalusia, Spain) by exposure to hydrous solutions of Fe<sup>2+</sup> mainly by means of Mössbauer spectroscopy. This method allows one to distinguish the different Fe sites present in the solid and the oxidation state of iron on the different lattice sites.

In Fig. 1 we show the room temperature and the 4.2 K Mössbauer spectra of the Fe<sup>2+</sup> exchanged Santa Olalla vermiculite. The corresponding spectra of the Ojén vermiculite look almost similar. The 4.2 K spectra differ substantially from those of the starting materials. In the spectra of both Fe<sup>2+</sup> forms one observes strong additional Fe<sup>2+</sup> component with a quadrupole splitting that is substantially larger than that of the structural Fe<sup>2+</sup>, and an intensity of about 50% of the spectral area in the Santa Olalla vermiculite and of about 40% in that from Ojén. This component is attributed to intercalated Fe<sup>2+</sup> (i-Fe<sup>2+</sup>). Its absence in the RT spectra can be explained by a strong decrease of the Lamb-Mössbauer *f*-factor (*f*-factor) of this component with increasing temperature, as has been observed previously in smectites. The component of intercalated Fe<sup>2+</sup> that is dominant in the 4.2 K spectra

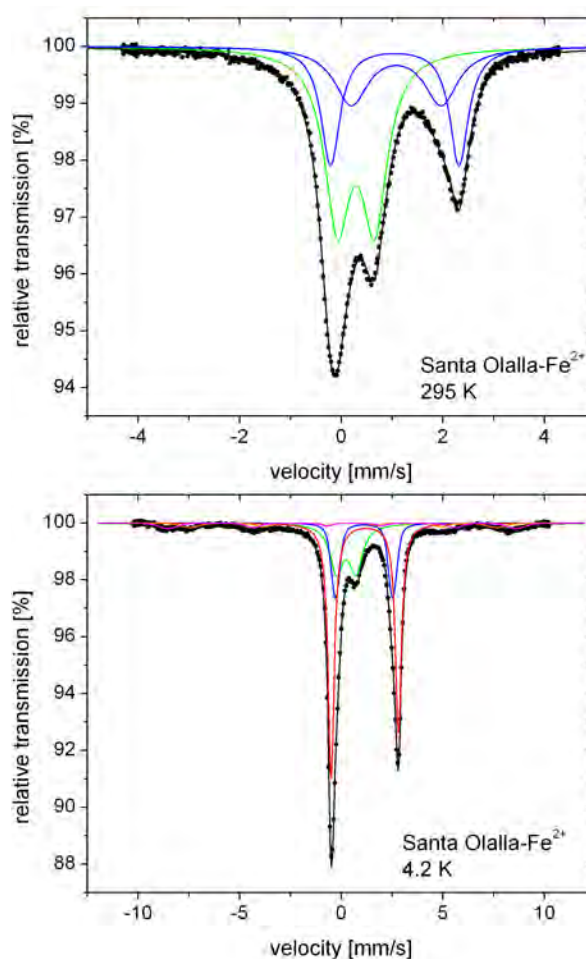


**Figure 1:** Mössbauer spectra taken at room temperature (top) and 4.2 K (bottom) of the Fe<sup>2+</sup> intercalated Santa Olalla vermiculite.

<sup>1</sup>Physik-Department, Technische Universität München, Garching, Germany

<sup>2</sup>Instituto de Ciencia de Materiales de Sevilla, Consejo Superior de Investigaciones Científicas-Universidad de Sevilla, Sevilla, Spain

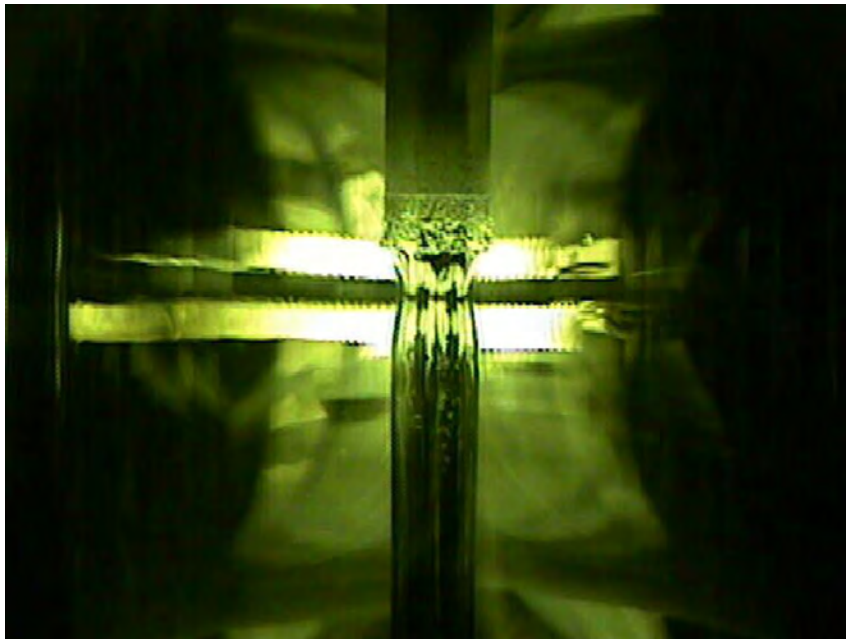
of the iron exchanged samples was fitted by a Lorentzian quadrupole doublet, which had to be allowed to have asymmetrical intensities with the right line being weaker than the left one. This asymmetry could be due to texture effects, but since none of the other components exhibits similar asymmetries, it is most probably due to the anisotropy of the  $f$ -factor indicating that the vibrational motion of the intercalated  $\text{Fe}^{2+}$  is strongly anisotropic. With the plausible assumption that the vibrational amplitudes are larger in the basal plane of the phyllosilicates than perpendicular to it, the observed asymmetry can be explained if the sign of the electric field gradient and hence the electric quadrupole interaction is negative.

In order to obtain a more detailed picture of the temperature dependence of the Mössbauer patterns, spectra were also taken between 4.2 K and about 280 K. For both iron exchanged vermiculites the  $\text{Fe}^{2+}$  component was found to decrease monotonically in this temperature range to become virtually invisible at 300 K. The intensity of the intercalated  $\text{Fe}^{2+}$  component decreases by a factor of 15 between 4.2 K and 284 K, where it is just barely discernible in the Mössbauer pattern. The intensity of the spectrum of a thin ( $2.3 \text{ mg/cm}^2$ )  $\text{Fe}_2\text{O}_3$  absorber measured under the same circumstances as the  $\text{Fe}^{2+}$  vermiculites decreases only by a factor of 1.3 between 4.2 and 250 K, which includes the decrease of the  $f$ -factor of the source. The intensity of the structural  $\text{Fe}^{2+}$  (o- $\text{Fe}^{2+}$ ) component decreases hardly at all, which may be an artefact of the fitting procedure arising from the incomplete separation of the structural and the intercalated  $\text{Fe}^{2+}$  in the Mössbauer patterns, which causes some uncertainty in the relative intensities. The electric quadrupole splitting of the i- $\text{Fe}^{2+}$  decreases from 3.36 mm/s at 4.2 K to 3.00 mm/s at 284 K, while the isomer shift increases slightly from 1.15 mm/s to 1.20 mm/s, presumably because of a slightly different temperature dependence of the second order Doppler shifts of the source and the absorber. The intensity of the  $\text{Fe}^{3+}$  component increases by a factor of 1.56 when the temperature is lowered from 284 to 40 K, more strongly than that of the structural  $\text{Fe}^{2+}$  and of  $\text{Fe}_2\text{O}_3$ . The observed quadrupole splitting for the intercalated  $\text{Fe}^{2+}$  site is in good agreement with the values given by Helson et al. and Charlet and Tournassat and assigned to the  $\text{Fe}^{2+}$  hexaquo complex  $[\text{Fe}(\text{H}_2\text{O})_6]^{2+}$ .

The intensities of the individual components in the spectra of the  $\text{Fe}^{2+}$  exchanged vermiculites can be compared with those calculated from the chemical formulae, assuming that the interlayer  $\text{Mg}^{2+}$  present in the original vermiculites was replaced completely by  $\text{Fe}^{2+}$ . At a first glance, the expected and observed amount of intercalated  $\text{Fe}^{2+}$  agree very well for  $\text{Fe}^{2+}$  Santa Olalla vermiculite, indicating a complete ion exchange, whereas for the  $\text{Fe}^{2+}$  Ojén vermiculite the experimental value for i- $\text{Fe}^{2+}$  is substantially higher than the expected one. An explanation for the unexpectedly high amount of intercalated  $\text{Fe}^{2+}$  could be that some iron left the octahedral sheet. This is not uncommon, since it is known that structural iron can be lost after reduction. The most striking effect is a change in the  $\text{Fe}^{2+}/\text{Fe}^{3+}$  ratio within the octahedral sheet in both vermiculites, i.e., a substantial increase of the amount of structural  $\text{Fe}^{2+}$  and a concomitant decrease of the amount of structural  $\text{Fe}^{3+}$ . The reduction of structural  $\text{Fe}^{3+}$  to  $\text{Fe}^{2+}$  is connected with an increase of the layer charge and would lead, consequently, to a change of the cation exchange capacity.

In the present case, only the intercalated  $\text{Fe}^{2+}$  or the  $\text{Fe}^{2+}$  in the aqueous solution can act as the reducing agent. If the intercalated  $\text{Fe}^{2+}$  is the reducing agent, one would expect  $\text{Fe}^{3+}$  to form in the interlayer space. This could indeed be the case since the temperature dependence of the  $\text{Fe}^{3+}$  component in the Mössbauer spectra indicates the presence of an intercalated  $\text{Fe}^{3+}$  species that is more weakly bound than the structural  $\text{Fe}^{3+}$ .

# Materials, Thin Film and Nanotechnology, Experimental Techniques



Growth of a  $\text{Pr}_{2-x}\text{Ce}_x\text{CuO}_4$  single crystal by the traveling solvent floating zone method in a four-mirror image furnace.



## A Cryogen-Free $^4\text{He}$ -JT-Stage: Retrofit of our Cryogen-Free Dilution Refrigerator.

K. Uhlig

**Introduction.** Usually, in cryogen-free  $^3\text{He}$ / $^4\text{He}$  dilution refrigerators (DR) there is no 1 K-stage ("pot") to condense the back-streaming  $^3\text{He}$ . Instead, after being pre-cooled by a two-staged pulse tube refrigerator (PTR) [1], the  $^3\text{He}$  is condensed in a counterflow heat exchanger where the latent heat of vaporization is transferred to the cold  $^3\text{He}$  pumped from the still of the DR [2]. Currently, all commercial manufacturers of "dry" DRs use this method. In recent work, we have demonstrated that by carefully utilizing the refrigeration capacities of the PTR, the counter-flow heat exchanger can be left out and the condensation of the  $^3\text{He}$  is taken over by the 2<sup>nd</sup> stage of the PTR [3]. Either way, there is only one flow circuit in these DRs.

There are experimental applications, however, where high cooling capacities are required at a temperature near 1 K to cool electronic components or to heat sink cables. For applications where the cooling capacity of the still ( $T \approx 0.7\text{ K}$ ) is not sufficient, an additional cooling stage would be desirable [4]. In our cryogen-free cryostat, a  $^4\text{He}$ -JT-circuit was installed and tested; operating temperatures of the cooling circuit were near 1 K [5]. So far, the new 1 K-stage was run alone without the DR in operation. The next experimental step will be to combine the 1 K-circuit with the DR-circuit in the cryostat.

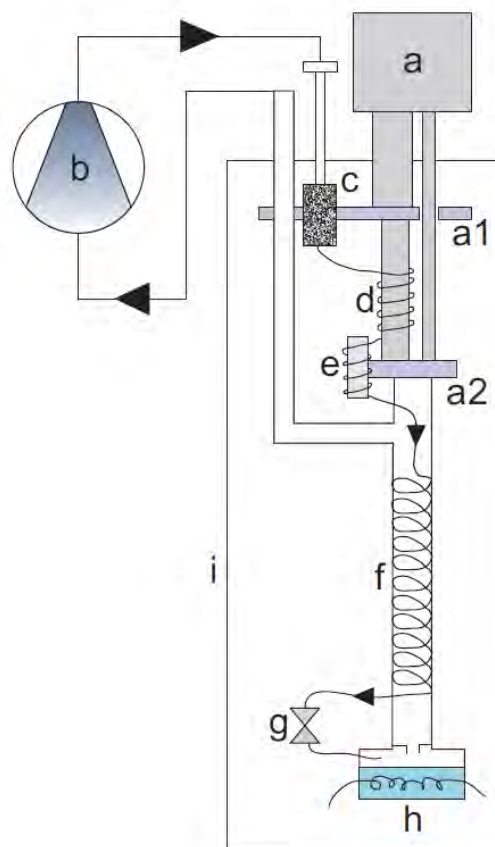


**Figure 1:** Layout of the  $^4\text{He}$ -JT-stage. a-PTR; a1 - 1<sup>st</sup> stage; a2-2<sup>nd</sup> stage; b-pumps (see text); c-charcoal trap; d-heat exchanger at 2<sup>nd</sup> regenerator; e-heat exchanger; f-counterflow heat exchanger; g-flow restriction; h-vessel with heater; i-bucket.

**Setup and results.** In Fig. 1 the layout of the new JT-stage is depicted. The  $^4\text{He}$  flow enters the cryostat through a charcoal trap which is anchored at the 1<sup>st</sup> stage of the PTR ( $T \approx 50\text{ K}$ ). Next, the gas stream is further cooled in a heat exchanger which consists of a capillary that is soldered to the outside of the 2<sup>nd</sup> regenerator of the PTR. Here the large heat capacity of the cold helium gas of the PTR is used to cool the small helium stream of the JT refrigerator to  $T \approx 4\text{ K}$  without noticeably affecting the cooling capacity of 2<sup>nd</sup> stage of the PTR [6]. There, the helium flow is liquefied and the liquid cooled to  $2.5\text{ K} < T < 3\text{ K}$ , depending on the flow rate. After the 2<sup>nd</sup> stage of the PTR the liquid helium flows through a counter-flow heat exchanger; here it is further cooled before it is expanded in a flow restriction. Two different types of heat exchangers have been tested [7]. It turned out that our "classic" model made from a structure of capillaries was very efficient.

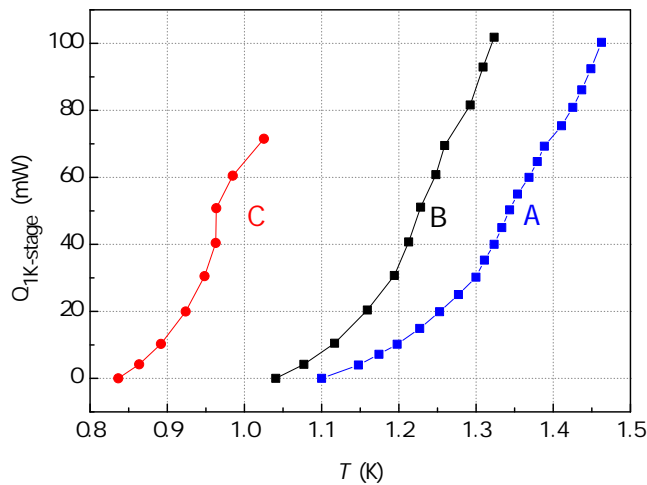


**Figure 2:** Refrigeration capacity of the 1 K-stage. A: Circuit with 2 rotary pumps ( $66 \text{ m}^3/\text{h}$ ); B: Circuit with 3 rotary pumps ( $100 \text{ m}^3/\text{h}$ ); C: Turbo pumps and rotary pumps in operation. For details see text.

In Fig. 2 the refrigeration capacity of the 1 K-stage is given for three different combinations of our pumping system. In "A" the circuit was run with two of our rotary pumps in parallel (total pumping speed:  $66 \text{ m}^3/\text{h}$ ). Here, the lowest temperature was 1.1 K, and a maximum cooling capacity of 100 mW was reached at 1.46 K.

In "B" a third rotary pump (combined pumping speed:  $100 \text{ m}^3/\text{h}$ ) was added to the flow circuit, leading to a base temperature of 1.05 K and a highest cooling capacity of 100 mW at 1.32 K. In "C" we used two turbo pumps in parallel (Varian T-V 551), backed by the rotary pumps; the base temperature was 0.83 K, and the highest cooling capacity of 70 mW was reached at 1.03 K. Higher cooling capacities could not be achieved because the maximum flow of the turbo pumps was reached.

In summary, the cooling capacity of the additional 1 K-stage exceeds the one of the still of an average size DR by a factor of 10. In the 1 K-stage presented here, the amount of  $^4\text{He}$  in the circuit remains constant; so the liquid level in the cold vessel can be controlled and kept constant, whereas in the "pot" of a traditional DR the liquid level cannot be controlled as the vessel fills up with superfluid helium; then the liquid level is mostly governed by the heat leak of the superfluid film between the liquid in the vessel and the helium dewar and a major part of the cooling power of the pot is wasted.

In summary, the cooling capacity of the additional 1 K-stage exceeds the one of the still of an average size DR by a factor of 10. In the 1 K-stage presented here, the amount of  $^4\text{He}$  in the circuit remains constant; so the liquid level in the cold vessel can be controlled and kept constant, whereas in the "pot" of a traditional DR the liquid level cannot be controlled as the vessel fills up with superfluid helium; then the liquid level is mostly governed by the heat leak of the superfluid film between the liquid in the vessel and the helium dewar and a major part of the cooling power of the pot is wasted.

**Outlook.** In Fig. 3 the flow scheme of the DR with the built-in  $^4\text{He}$ -JT-stage is depicted. The dilution unit has a cooling capacity at the mixing chamber of  $700 \mu\text{W}$  at a temperature of 100 mK; its base temperature is below 10 mK.

1. Here, the DR and the 1 K-stage can be operated independently from each other, and so the full cooling capacity of the 1 K-stage is available.
2. Alternatively, the 1 K-stage can be utilized to condense the back-streaming  $^3\text{He}$  of the DR. Then the counterflow heat exchanger of the dilution unit can be saved.
3. Another option would be to leave out the counterflow heat exchanger of the 1 K-stage. This would lead to a smaller cooling capacity of the 1 K-stage, but would also mean a simpler (and perhaps shorter) construction. This situation is shown in Fig. 3.

Most commercial DRs are equipped with quite powerful PTRs with power consumptions of over 9 kW. In our cryostat a small PTR (4.7 kW) is used to demonstrate that a PTR with low power consumption (and a low level of vibration) is sufficient to precool a powerful mK-cryocooler.

Finally, the 1 K-stage could be advantageous in combination with an ADR (adiabatic demagnetization refrigerator). Cryogen-free ADRs have been commercially available for quite some time. With skyrocketing prices of  $^3\text{He}$  for DRs, ADRs become more and more competitive. With these ADRs, the demag stage is pre-cooled by the PTR to  $\approx 3 \text{ K}$ ; with the installation of a

1 K-stage the pre-cooling conditions can be improved by a factor of 2 to 4 with modest outlay, and thus lower demag temperatures or higher heat capacities after the demag are obtained. Also, paramagnetic salts other than the ones used so far (with lower ordering temperature) become viable.

Several measures were taken in the course of last year to upgrade our cryogen-free cryostat.

1. The main pumping line of the DR was replaced to allow for higher  $^3\text{He}$  throughputs (the inner diameter of the pumping line is now 210 mm).
2. New turbo pumps were installed. Vibration attenuators will be tested soon.
3. The PTR was equipped with 2 heat exchangers at the regenerator. The soldering was done at the WMI.
4. The motor/valve unit of the PTR was separated from the pulse tubes to reduce vibrations. This chore was done by the manufacturer in the US [8].
5. The filters of the PTR were replaced after 20,000 hours of running. Filters were purchased from the manufacturer and installed at the WMI.
6. A new control panel was designed and installed for the 1 K-stage (WMI machine shop).
7. A filling height sensor (cylindrical capacitor) for the still of the DR was designed, mounted and tested. Now the helium level in the still can be monitored precisely during an experiment.

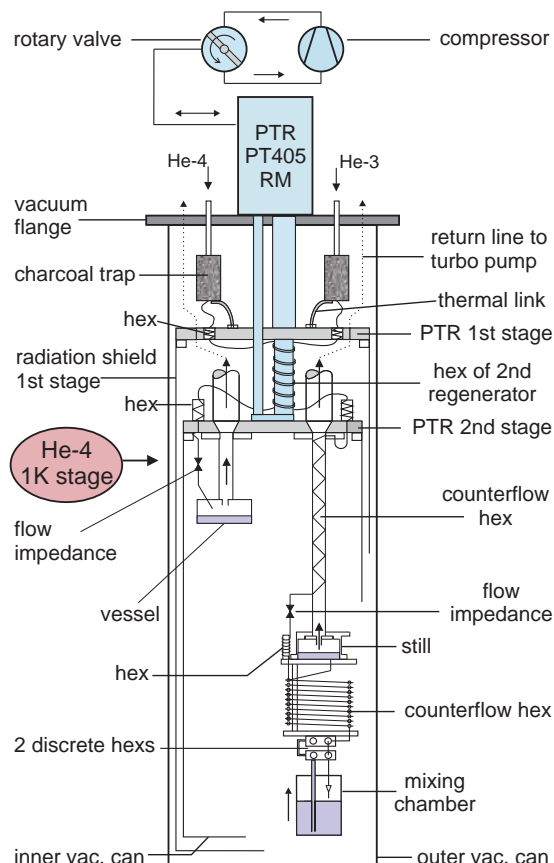


**Figure 3:** Present setup of the dry fridge. On the left side of the refrigerator the 1 K-stage is placed; it has no counterflow heat exchanger in its present design. The dilution unit is on the right side of the cryostat.

We look forward to putting the cryostat with the DR/1 K-stage into operation in the months to come.

## References

- [1] R. Radebaugh, Development of the Pulse Tube Refrigerator as an Efficient and Reliable Cryocooler, Technical report, NIST, Boulder, CO 80303, USA (2000).
- [2] K. Uhlig, *Adv. Cryo. Eng.* **53B**, 1287 (2007).
- [3] K. Uhlig, *Cryogenics* **48**, 511 (2008).
- [4] A. Marx, private communication.
- [5] K. Uhlig, *Cryocoolers* **16** (2010), to be published.
- [6] K. Uhlig, *Cryogenics* **48**, 138 (2008).
- [7] K. Uhlig, *Adv. Cryo. Eng.* **55A**, 641 (2009).
- [8] Cryomech Inc., Syracuse, N.Y.

## Susceptibility Measurements in a Diamond Anvil Pressure Cell

R. Roßner, H.-M. Eiter, A. Baum, A. Erb, R. Hackl<sup>1</sup>

The combination of susceptibility and Raman measurements in a high pressure diamond anvil cell (DAC) is a very promising experimental tool which can provide new insight into the competition of different electronically ordered phases. In high temperature superconductors for instance, it is still an open question whether a suppression of the competing electronic order can enhance  $T_c$ . Recently an unusual two-step enhancement of  $T_c$  was found in Bi2223 at high pressure [1].

The existing DAC, which was used already for Raman experiments on LaTe<sub>3</sub> [2], was now supplemented with a setup for susceptibility measurements. Detecting the susceptibility inside a DAC is an experimentally challenging task due to the small sample size of about  $100 \times 100 \times 25 \mu\text{m}^3$ , a very low filling factor of less than  $10^{-4}$  and a big temperature dependent background signal of the cell, the diamonds and particularly the metal gasket [3 in Fig. 1 (a)].

In Fig. 1 (a) the principle of operation of our homemade DAC is illustrated. High pressure is generated by applying force on a piston (1). The ratio of areas transforms a moderate pressure at the piston to hydrostatic pressures up to 20 GPa or 200 kbar in the volume enclosed by the tips of the diamonds (2) and the gasket (3). Part (b) shows the coils used for the susceptibility measurements. The coil in the center encloses one diamond and the sample. The combination of this

coil and the empty one forms a gradiometer to compensate for the local background signal. Each of the two coils consists of a field and a pickup coil. Figure 1 (c) shows the block diagram of the electronics used for the measurement [3].

The new setup was tested with an underdoped YBa<sub>2</sub>Cu<sub>3</sub>O<sub>6.7</sub> sample. The crystal was annealed at high temperature with the appropriate oxygen partial pressure [4] in a procedure described elsewhere [5]. A  $T_c$  of 67 K, corresponding to a doping level  $p \approx 0.12$  [6], was determined first in a macro setup [7]. For this doping level the pressure dependence of  $T_c$  is large [8].

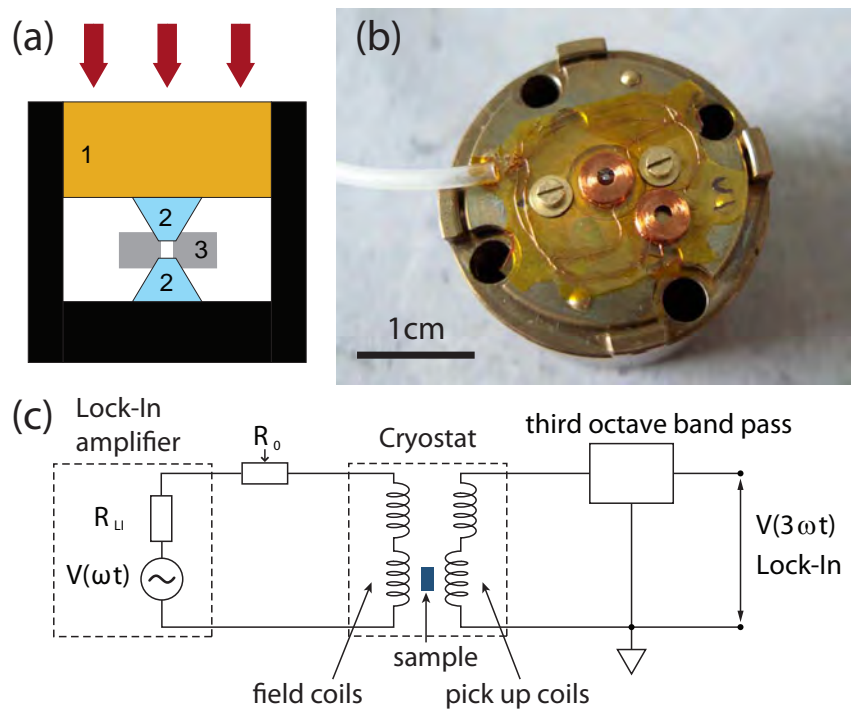
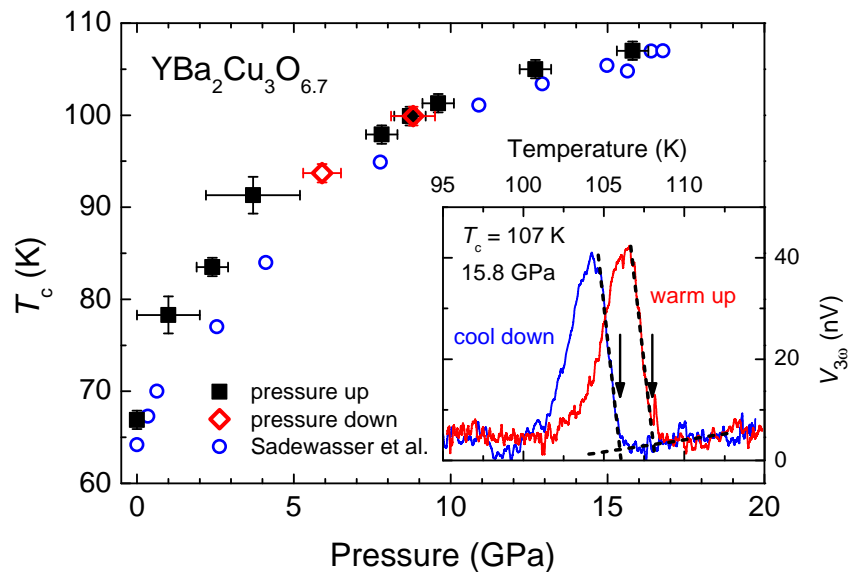


Figure 1: Experimental setup: (a) principle of operation of the DAC; (b) coils for the susceptibility measurement; (c) block diagram of the electronic setup

<sup>1</sup>This work is supported by the German Research Foundation under Grant No. Ha 2071/5.

In Fig. 2 the dependence of  $T_c$  on the applied pressure is plotted. The inset shows the voltage detected at the third harmonic frequency  $3\omega$  of the exciting field for a pressure of 15.8 GPa. During the temperature sweeps [see inset of Fig. 2] it is essential to keep the pressure constant. From the raw data a linear temperature dependent background was subtracted. The signal to noise ratio is better than 10, and the superconducting transition can be clearly detected.  $T_c$  corresponds to the temperature, where the extrapolation of the high temperature flank of the peak and the background intersect, as illustrated by dashed lines and arrows. The curves recorded for cooling and heating are offset by about 2.5 K for a temperature variation rate in the range of 0.3 to 0.5 K/min. The hysteresis is due to the distance between the sample and the thermometer. The temperatures indicated in the main plot correspond to the average  $T_c$  value of cooling and heating run. Without an applied pressure  $T_c = 67$  K is reproduced. Below 2 GPa,  $T_c$  changes at a rate of approximately 10 K/GPa. Above 8 GPa the slope reduces to 1 – 2 K/GPa. The critical temperature seems to saturate at about 110 K.  $T_c$  changes reversibly with pressure. Included in the figure are also data of a similarly doped YBCO sample with a  $T_c$  of 64.2 K at zero pressure [8], which thus has a comparable pressure dependence.



**Figure 2:** Dependence of the superconducting transition temperature  $T_c$  of  $\text{YBa}_2\text{Cu}_3\text{O}_{6.7}$  on applied pressure. The inset shows the susceptibility measurements for a pressure of 15.8 GPa.  $T_c$  (arrows) corresponds to the temperature, where the extrapolation of the high temperature flank of the peak and the background intersect (dashed lines). Due to a temperature gradient between the thermometer and the sample, there is an offset of  $\approx 2.5$  K between warming and cooling. The temperatures indicated in the main plot correspond to the average value of these two runs. The circles are results of Sadewasser et al. [8].

## References

- [1] X.-J. Chen, V. V. Struzhkin, Y. Yu, A. F. Goncharov, C.-T. Lin, H.-K. Mao, and R. J. Hemley, *Nature* **466**, 950 (2010).
- [2] M. Lavagnini, H.-M. Eiter, L. Tassini, B. Muschler, R. Hackl, R. Monnier, J.-H. Chu, I. R. Fisher, and L. Degiorgi, *Phys. Rev. B* **81**, 081101R (2010).
- [3] R. Roßner, *Untersuchung von korrelierten Elektronensystemen unter hohem Druck*, Diploma thesis, WMI (2010).
- [4] T. B. Lindemer, J. F. Hunley, J. E. Gates, A. L. Sutton, J. Brynstad, and C. R. Hubbard, *J. Am. Ceram. Soc.* **72**, 1775 (1989).
- [5] T. Buttler, *Optimierung, Charakterisierung und Untersuchung hochgeordneter Y-123 Einkristalle*, Diploma thesis, WMI (2009).
- [6] R. Liang, D. A. Bonn, and W. N. Hardy, *Phys. Rev. B* **73**, 180505 (2006).
- [7] F. Venturini, *Raman Scattering Study of Electronic Correlations in Cuprates: Observation of an Unconventional Metal-Insulator Transition*, Ph.D. thesis, WMI (2003).
- [8] S. Sadewasser, J. S. Schilling, A. P. Paulikas, and B. W. Veal, *Phys. Rev. B* **61**, 741 (2000).

## Broadband Microwave Spectroscopy of Magnetic Thin Films

*H. Huebl, C. Zollitsch, F. Hocke, M. Weiler, M. Althammer, S. T. B. Goennenwein<sup>1</sup>*

Ferromagnetic resonance (FMR) is a sensitive tool for the investigation of the magnetic anisotropy and magnetization dynamics in ferromagnetic films. In particular, FMR also gives access to magnetization damping, i.e., to an important quality criterion of magnetic thin films. For magnetization damping measurements in magnetic thin films, broadband microwave spectroscopy is typically applied. As the microscopic magnetization damping mechanisms often involve the emission of magnons and relaxation via phonons [1], studies of the damping as a function of temperature are an obvious goal. Surprisingly, however, no damping experiments below 1 K have been performed to date.

In order to enable damping studies down to a few millikelvin, we have set up a broadband FMR measurement apparatus in a dilution refrigerator. In the last year, we incorporated microwave coaxial lines to perform broadband microwave spectroscopy into an existing dilution unit compatible with a superconducting solenoid magnet. In this setup, FMR experiments down to temperatures of approx. 50 mK are possible. Figure 1 shows the inside of the inner vacuum cylinder with microwave attenuators at the 4 K flange, at the still (approx. 0.8 K) and at the mixing chamber to ensure that the inner conductor of the microwave coax lines equilibrate thermally with the mixing chamber temperature. The high-frequency lines equipped with SMA connectors allow spectroscopy in the frequency range from DC to about 20 GHz. We use vector network analysis to measure the complex transmission amplitude  $S_{21}$  of the complete system.

As a proof of principle experiment we investigated a cobalt thin film deposited via electron beam evaporation on an intrinsic silicon substrate. The Co film is 50 nm thick and mounted in flip-chip configuration on a coplanar waveguide (CPW) made from gold, also on intrinsic silicon (cf. Fig. 2). The magnetic field component of the microwave radiation propagating in the CPW induces in combination with an externally applied static magnetic field  $\mu_0 H$ , allows to drive the ferromagnetic film into ferromagnetic resonance. The FMR resonance frequency  $\omega/(2\pi)$  is determined by

$$\frac{\omega}{\gamma} = \frac{1}{M^2 \sin^2 \Theta} \left[ \frac{\partial^2 F}{\partial \Theta^2} \frac{\partial^2 F}{\partial \Phi^2} - \left( \frac{\partial^2 F}{\partial \Theta \partial \Phi} \right)^2 \right], \quad (1)$$

where  $\Theta$  and  $\Phi$  the equilibrium orientation of the magnetization  $M$  [2]. The magnetic properties of the thin film are summarized by the free energy  $F$ , which includes the Zeeman interaction and the demagnetization term. FMR microwave spectroscopy

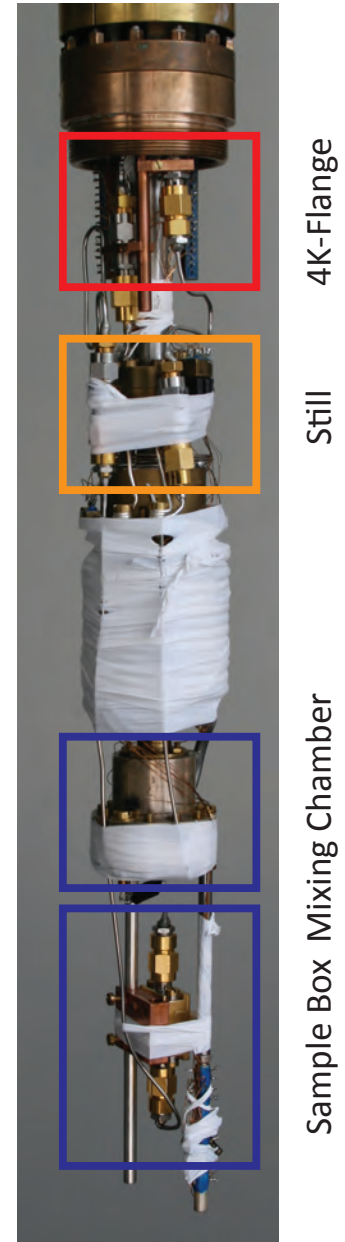


**Figure 1:** Modified dilution unit for microwave spectroscopy in magnetic fields.

<sup>1</sup>This project is supported by the German Research Foundation via SFB 631 and the German Excellence Initiative via the Nanosystems Initiative Munich (NIM).

based on (1) is well established at the Walther-Meissner-Institute, and used routinely to characterize FMR films from room temperature to 4 K. Furthermore, microwave spectroscopy in the aW regime is a standard technique in the area of qubit-microwave cavity spectroscopy.

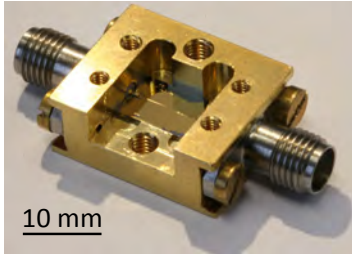


**Figure 2:** Picture of the sample holder with the microwave coplanar waveguide manufactured on a silicon substrate.

The microwave transmission amplitude is initially dominated by the attenuation of the attenuators, the microwave lines and the coplanar waveguide. Nevertheless those contributions show no magnetic field dependence and can therefore be subtracted. In particular, we calculate for each frequency and magnetic field the magnitude of the transmission parameter  $\text{abs}(S_{21}(f, \mu_0 H))$  and subtract the average of the transmission parameter  $\text{abs}(S_{21}(f, \overline{\mu_0 H}))$ , which results in a false color plot as shown in Fig. 3. We find a pronounced V-shaped resonance structure symmetric in the magnetic field for frequencies above 6 GHz, as expected for cobalt with the magnetic field applied in the film plane. This V-shaped FMR signature can be detected down to excitation powers of 100 fW showing the excellent sensitivity of the spectrometer, even though only room temperature electronics are used to analyze the microwave signals.

The successful demonstration of FMR spectroscopy down to 50 mK opens the way for further experiments. We currently work to address the following subjects: (i) How small ferromagnetic structures can be investigated with our setup? In this context, we plan to lithographically define transition metal samples directly on the center strip of the CPW. (ii) We will extend the setup for the application of out-of-plane magnetic fields in order to investigate the damping properties of magnetic films while suppressing two-magnon scattering processes and line broadening due to the film orientation [3]. (iii) Obviously, the study of modern magnetic materials, such as Heusler compounds, or oxide ferro- and antiferromagnets, opens an exciting perspective on the fundamental physics of magnetization damping.

The microwave transmission amplitude is initially dominated by the attenuation of the attenuators, the microwave lines and the coplanar waveguide. Nevertheless those contributions show no magnetic field dependence and can therefore be subtracted. In particular, we calculate for each frequency and magnetic field the magnitude of the transmission parameter  $\text{abs}(S_{21}(f, \mu_0 H))$  and subtract the average of the transmission parameter  $\text{abs}(S_{21}(f, \overline{\mu_0 H}))$ , which results in a false color plot as shown in Fig. 3. We find a pronounced V-shaped resonance structure symmetric in the magnetic field for frequencies above 6 GHz, as expected for cobalt with the magnetic field applied in the film plane. This V-shaped FMR signature can be detected

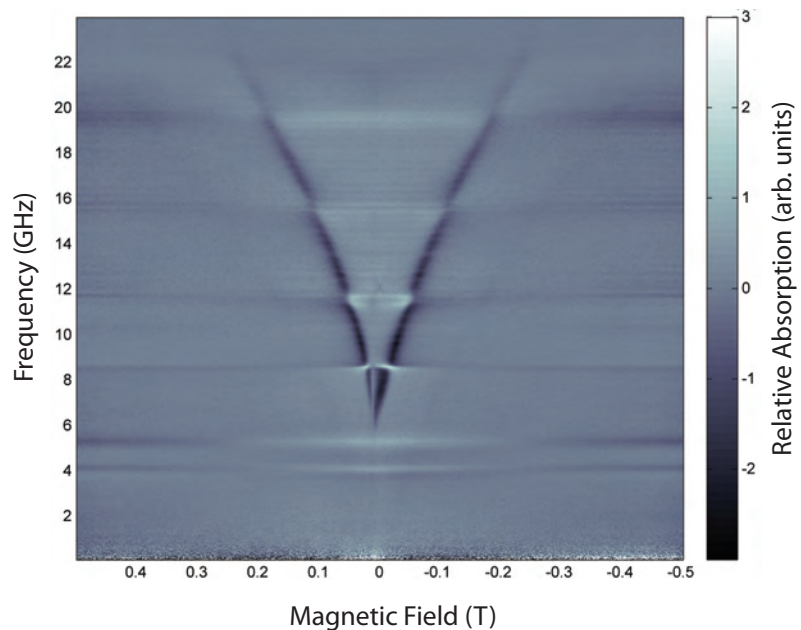


**Figure 3:** Background subtracted microwave transmission as function of the applied magnetic field for a 50 nmthick cobalt film on an intrinsic silicon substrate. The pronounced V-shape absorption is attributed to ferromagnetic resonance in the cobalt thin film.

## References

- [1] M. Sparks, *Ferromagnetic-Relaxation Theory* (McGraw-Hill, New York, 1964).
- [2] S. V. Vonsovskii, *Ferromagnetic Resonance* (Israel Programm for Scientific Translations, Jerusalem, 1964).
- [3] J. A. C. Bland and B. Heinrich, *Ultrathin Magnetic Structures III: Fundamentals of Nanomagnetism* (Springer, Berlin, 2005).

## Colloidal Graphite Oxide, its Purification, Phase Transfer and Electrokinetic Properties

A. Lerf

P. Feicht, J. Breu<sup>1</sup>

Recently, the Nobel Prize in physics was awarded to Andre Geim and Konstantin Novoselov for their research on graphene, a single atomic layer of graphite. At that time - expressed in simplified terms - they used an adhesive tape to get graphene [1]. For application of graphene new techniques for large-scale production have been developed, including the preparation of graphene oxide (GO) and its subsequent reduction. The most common preparation methods for GO were developed by Brodie [2], Staudenmaier and Hummers/Offemann. In the first two methods  $\text{KClO}_3$ /fuming  $\text{HNO}_3$  mixtures are used for oxidation and in the latter  $\text{H}_2\text{SO}_4$ ,  $\text{HNO}_3$  and  $\text{KMnO}_4$ . The biggest advantage of the Hummers method is the saving of time. While one spends about four weeks time for four oxidation cycles with Brodie's method, it takes only two days synthesizing GO with the one of Hummers/Offemann [3]. However, the purification is a big issue, as a lot of manganese remains in the GO structure. Even with the following dialysis, needing about two weeks, the content of manganese is still high. Therefore, we developed a phase-transfer reaction with an alkylamine from the as-prepared, undialyzed GO (GOAM) into various organic solvents by what the amount of all metal ions could be decreased to an average of 20% compared to the dialyzed GO (see Fig. 1).

A typical procedure is as follows: 1 mL GO (1 mg/mL) is mixed with 0.5 mg dodecylamine in about 0.3 mL EtOH resulting in a light brown aggregation. When adding diethylether the aggregates can be redispersed in the organic solvent and then separated from the water. For a thorough removal of the water the organic phase should be filtered and washed with ethanol. Subsequently, different organic solvents (butanone, pyridine, acetonitrile, dimethylformamide, ethylacetate, tetrahydrofuran, chloroform, dichloromethane, xylene, styrene) can be added.

In a final step, if the content of a little water is acceptable, one can remove the diethylether by distillation under reduced pressure. The resulting GO can reach concentrations up to 3 mg/mL. These colloidal dispersions are stable for weeks. Müllen et al. developed a similar procedure using quaternary ammonium salts [4]. Experimental parameters, such as pH value, weight ratio between graphene oxide sheets and surfactant, and solvent, have a critical influence on the transfer efficiency. The best conditions were found to be at a pH value around 9, a weight ratio between GO and didodecyldimethylammoniumbromide of around 3:1 and with chloroform. It is not possible to redisperse the GO in other solvents with this method.

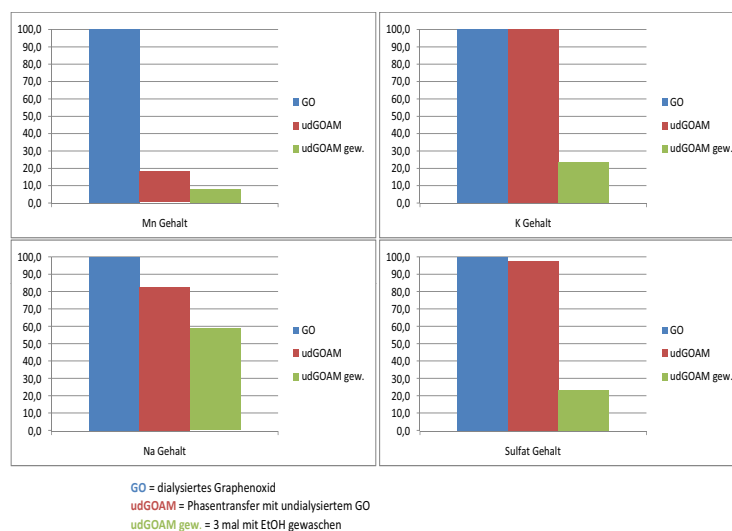


**Figure 1:** Content of cations after dialysis (GO) and phase transfer (udGOAM).

<sup>1</sup>Institut für Anorganische Chemie, Universität Bayreuth, Germany

For characterization of the colloidal dispersion Zeta potential measurements were made with GO in water (see Fig. 2). At the starting pH 3 the potential is  $-140$  mV and it quickly decreases by adding  $0.05$  M NaOH to about  $-380$  mV. Reaching a pH value of  $12.8$  the potential increases to a value near zero. The decrease at  $\text{pH} < 7$  is connected with the deprotonation of the carboxyl groups at the edges of the GO layers. From the small amount

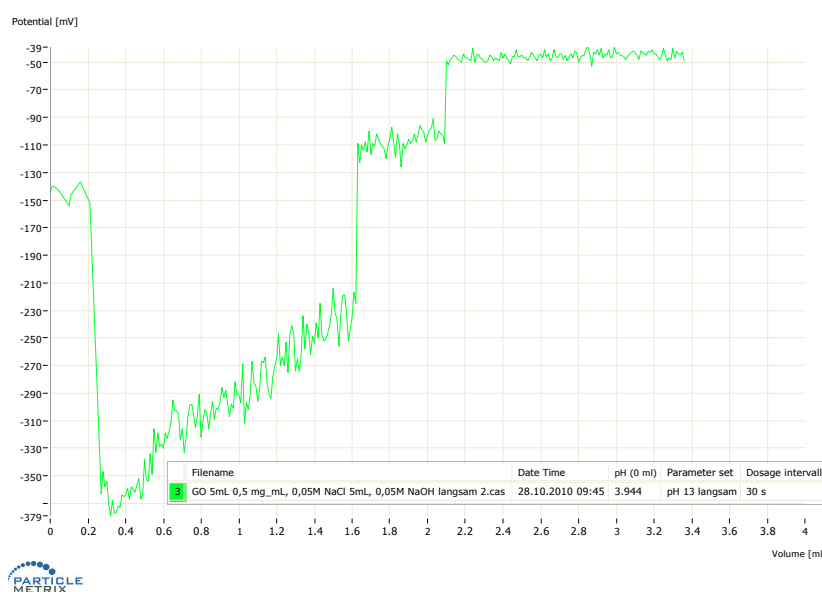


Figure 2: Zeta-Potential of GO as function of the added base

( $0.24$  mg NaOH per  $1$  mg GO) of a diluted base needed for this big change one can conclude that the number of of these functional groups is pretty small. Another experiment emphasizing this hypothesis is the flocculation of the colloidal GO dispersion with bi- or trivalent ions. Only a very small amount is needed. Therefore, it looks like that the major part of the electrostatic stability of the GO dispersions is due to these functional groups at the edge of the layers. The sudden increase of the Zeta-potential at  $\text{pH} 13$  can probably be associated with the removal of carboxyl groups by reaction of the base with various functional groups like epoxides, hydroxides and lactones [5]. Since the dispersion turns black at such a high pH, it seems likely that some areas could have been rearomatized. But these colloids are still stable for months. Apparently, a complete oxidation of graphite is not necessary to get stable colloids. It is probably sufficient having carboxyl groups at the edges. But then it is no GO in terms of Boehm with various functional oxygen groups randomly spread over the layer [6]. However, since GO is an insulator rearomatization is required for many applications, that are dealing with electrical conductivity. The most common reducing agent is hydrazine. In order to replace it with less poisonous substances some other reducers, such as  $\text{NaBH}_4$ , heat and even sugars, have successfully been tested. With an AFM needle one can precisely reduce GO and get nano-scaled conductive paths for computer chips. It is also possible to depose  $\text{MnO}_2$  on the surface of reduced GO for supercapacitor electrodes [7]. In the near future, we will make experiments optimizing the synthesis of such nanocomposites.

## References

- [1] K. S. Novoselov, A. K. Geim, S. V. Morozov, D. Jiang, Y. Zhang, S. V. Dubonos, I. Grigorieva, and A. A. Firsov, *Science* **306**, 666 (2004).
- [2] B. Brodie, *Ann. Chim. Phys.* **59**, 466 (1860).
- [3] W. S. Hummers and R. E. Offeman, *J. Amer. Chem. Soc.* **80**, 1339 (1958).
- [4] Y. Y. Liang, D. Q. Wu, X. L. Feng, and K. Müllen, *Adv. Mater.* **21**, 1679 (2009).
- [5] J. Yan, Z. Fan, T. Wei, W. Quian, M. Zhang, and F. Wei, *Carbon* **48**, 3825 (2010).
- [6] H. P. Boehm, *Carbon* **32**, 759 (1994).
- [7] W. Scholz and H. P. Boehm, *Z. Anorg. Allg. Chem.* **369**, 327 (1969).



# Experimental Facilities





## The WMI Quantum Laboratory: Installation of New Laboratory Space for Sensitive Quantum Experiments

*H. Huebl, L. Osslander, T. Brenninger, A. Marx, R. Gross*<sup>1</sup>

Due to the financial downturn in 2008/2009 the German Federal Government launched an economic stimulus package (Konjunkturpaket II). Within this package, a variety of projects in the public sector were supported. In addition to projects aiming at the improvement of urban and rural infrastructure, a particular focus was on the development of the science and education sector.

The Walther-Meißner-Institute obtained financial funding from this stimulus package, in order to establish new laboratory space particularly suited for the study of quantum systems at low temperatures. This so-called “WMI Quantum Laboratory” was set up in a so far unused part of the building. The low temperature experiments require the operation of dilution refrigerators, imposing a large room height. This was realized by  $1.6 \times 1.2 \text{ m}^2$  wide and 2.3 m deep pits in the floor of three new laboratory rooms. Furthermore, cooling water and air-conditioning is required to ensure that the extremely sensitive experiments can be performed under constant environmental parameters.



**Figure 1:** Structural work in the basement of the Walther-Meißner-Institute (north-west-corner) in January 2010. Using a suitable digger, the gravel previously filling parts of the basement was removed. The picture is taken in southern direction from the north wall of the building.

During the construction work, about  $170 \text{ m}^3$  of gravel was removed from the basement with a suitable digger operating inside the building (cf. Fig. 1). Afterwards, a concrete platform was established and windows were cut into the sidewall. One of the laboratories in almost final stage is shown in Fig. 2, with windows, doorframes and heating system installed.

After the construction began in November 2009 with structural work, interior work started in May 2010 and currently comes to an end. Finally, from December 2010 to January 2011 the installation of water cooling and air-conditioning as well as the electrical installation are scheduled. Thus, the new WMI Quantum Laboratory will be operational for scientific experiments in spring 2011.



**Figure 2:** Status of the interior work in November 2010. The floor, the windows, the pit in the floor (closed with wooden planks) and the electric lighting is finished. The photo is taken in south-eastern direction from a point similar as in Fig. 1.

<sup>1</sup>This project is financially supported by German Federal Government via the Konjunkturpaket II.

## IT Infrastructure Upgrade at the WMI

*F.D. Czeschka, M. Weiler, D. Guratzsch, M. Opel<sup>1</sup>*

In 2010, the IT server infrastructure at WMI was updated, particularly with respect to reliability and efficiency of the main data processing systems. The work was done in close cooperation with Peter Vogl and his “DrVis” team. As the first step, the five existing network servers for user authentication (domain controller), data storage/printing (file/print server), sharing documents (sharepoint server), providing a gateway to the “Münchener Wissenschaftsnetz (MWN)” (firewall server), and email services (exchange server) were upgraded to the most recent software applications and operating systems (OS) versions. By keeping the server infrastructure up to date, the users are provided with a set of new features to enhance and facilitate IT usage. Furthermore, the updated server software greatly reduces the vulnerability to external threats such as viruses or unwanted email (spam).

Moreover, the existing servers were *virtualized* so that different servers with different OS and configurations can share the same hardware. Former physical servers were converted to *virtual hosts* (Fig. 1). On each of them, several virtualized servers (virtual guests) are installed. Hence, identical hardware is shared by a number of virtual guests. Using virtualization, it is possible to run one virtual server per task, greatly facilitating maintenance and reducing the impact of a server OS failure on the offered network services. Furthermore, this allows for a more efficient load balance of the existing hardware. The WMI now operates eight virtual hosts. They provide enough resources for all in all 19 virtual guests each performing a single dedicated task. In addition to the basic ones mentioned above that are necessary for a computer network, they are used for user administration, hosting SQL and other databases, distributing software and OS updates, distributing up-to-date antivirus software, network routing, and providing software collections for automatic network installation. Each virtual guest is represented by only one single *virtual hard drive* (vhd) file under the virtual host OS. This offers the possibility to easily migrate the virtual guest to different hardware by simply copying the vhd file from one virtual host to another. It can even be done while the virtual hosts are running and, hence, any virtual guest can be transferred without affecting any other virtual servers. This allows for convenient hardware maintenance on a virtual host, which can be carried out without any server downtime as all virtual hosts can be temporarily moved to a different hardware.

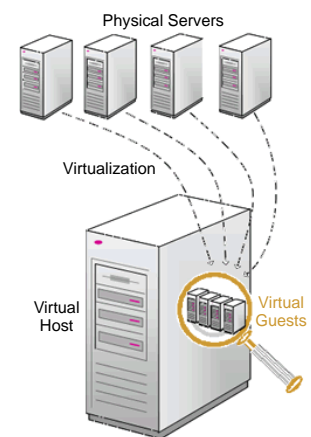


**Figure 1:** Server virtualization. If four virtual guests are installed on one virtual host, the number of physical servers needed is reduced from 4 to 1.

To further protect the servers from network attacks, we divided the WMI physical network into two independent virtual local area networks (VLANs) with their own IP address ranges, one for the servers and one for the client computers. They are connected via a router which, again, is a virtual guest server and provides three network interfaces: (i) server-VLAN, (ii) client-VLAN, and (iii) connection to the wide area network (MWN) via a gateway/firewall. This router also offers virtual private network (VPN) connections to the WMI network from home or anywhere outside, enabling, e.g., the possibility to remote-control lab equipment.

In summary, this IT infrastructure upgrade 2010 enables a smooth workflow at WMI together with a significantly enhanced security standard.

<sup>1</sup>In collaboration with the initiative “Windows für Wissenschaft” (Prof. Dr. Peter Vogl), DrVis Software GbR, and infoWAN Datenkommunikation GmbH.

## Overview of Key Experimental Facilities and Infrastructure

In the following basic information on the key experimental facilities and components of the technical infrastructure installed at the Walther-Meißner-Institute (WMI) is given.

### UHV-Laser-MBE

The WMI operates a UHV-Laser-Molecular Beam Epitaxy (L-MBE) system for the growth of complex oxide heterostructures. The system has been designed to meet the special requirements of oxide epitaxy. The UHV cluster tool consists of the following main components:

- central transfer chamber;
- load-lock chamber with heater system for substrate annealing;
- laser deposition chamber with in-situ reflection high energy electron diffraction (RHEED) system, laser substrate heating system, and atomic oxygen/nitrogen source, the RHEED system has been modified to allow for the operation at high oxygen partial pressure up to 0.5 mbar;
- surface characterization chamber with UHV scanning force microscope (Omicron);
- metallization chamber with a four heart electron gun system and a liquid nitrogen cooled sample stage. The sample holder can be tilt for shadow evaporation;
- KrF excimer laser.

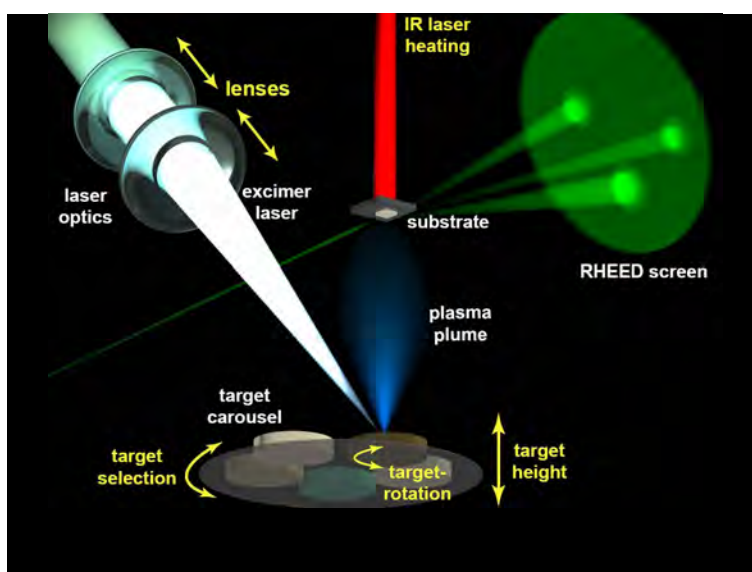
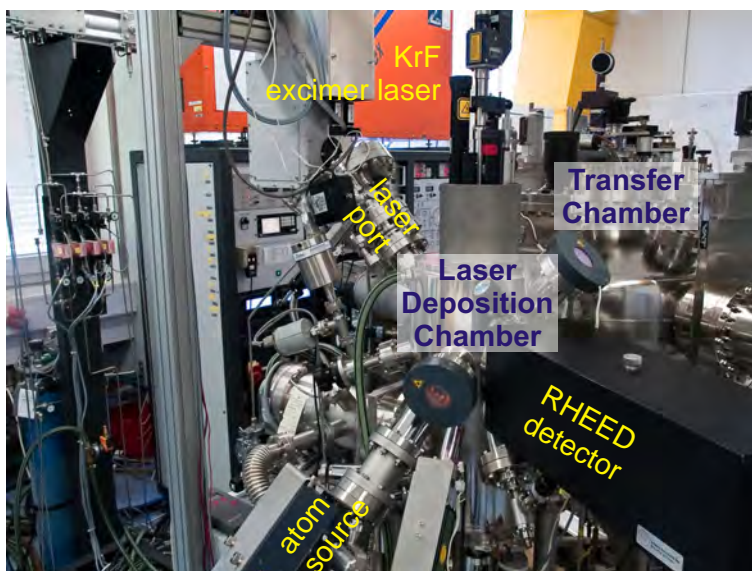
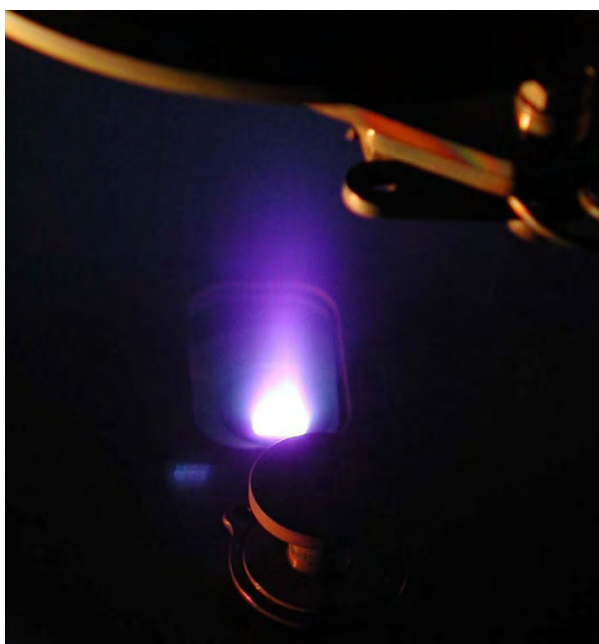


Figure 1: Top: UHV-Laser-Molecular Beam Epitaxy System. Bottom: Principle of the deposition process.

The system is used for the growth of complex oxide heterostructures consisting of superconducting, magnetic, dielectric, and semiconducting materials such as the high-temperature superconductors, the doped manganites, the double perovskites, magnetite, zinc oxide, etc..

The original laser molecular beam epitaxy system (laser-MBE) designed already in 1995/96 until now has been permanently upgraded and modified. In particular, the substrate heating system and the temperature control unit was changed from a resistive radiation heater to an infrared laser heating system (see Fig. 3, left) including a pyrometer for determining the sample temperature. In addition, a source for atomic oxygen and nitrogen has been added. The main advantage of the new heating system is that only the substrate is heated while the surrounding parts are hardly affected (Fig. 3, right). In this way one can achieve an essentially better vacuum at temperatures well above 1000°C. The achievable substrate temperature is limited by the melting point and the size of the substrate material (approx. 1410°C for a  $5 \times 5 \text{ mm}^2$  silicon substrate). The laser heating system has already been successfully used for removing the amorphous silicon oxide layer from the surface of silicon substrates at 1150°C. This is required for the epitaxial growth of oxide thin films on this substrate.



**Figure 2:** Pulsed Laser Deposition (PLD): When the pulse of the UV laser (KrF excimer laser, 248 nm) hits the target, the target material is ablated and the so-called laser “plume” containing highly excited atoms and molecules is formed.

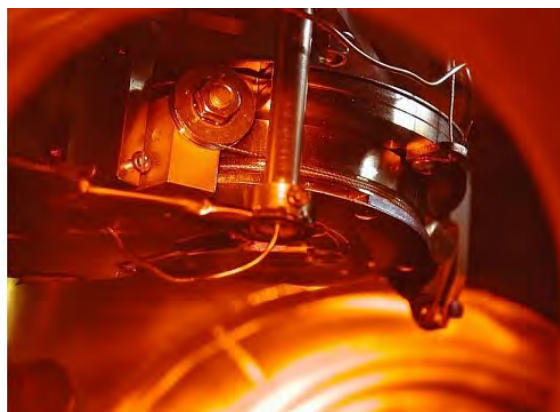
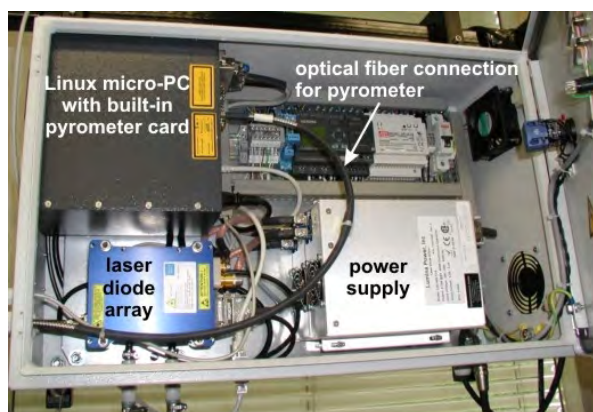


**Figure 3:** Components of the laser heating system: The substrate is heated using an IR diode laser head that is located in a separate box far away from the deposition chamber (left). The laser light is brought to the substrate (right) via an optical fiber.

## Single Crystal Growth and Synthesis of Bulk Materials

Transition metal oxides are of great interest due to their various interesting physical properties (e.g. high temperature superconductivity, colossal magnetoresistance, ferroelectricity, nonlinear optical properties etc.) and their high potential for applications. Therefore, the WMI operates a laboratory for the synthesis of bulk materials and single crystals of transition metal oxides. Besides various chamber- and tube furnaces a four-mirror image furnace is used in the crystal growth of various oxide systems. With this furnace crystals of many different compounds of the high temperature superconductors and various other transition metal oxides have been grown as single crystals using the traveling solvent floating zone technique. The furnace consists basically of 4 elliptical mirrors with a common focus on the sample rod and with halogen lamps in their other focus. By irradiation of the focused light the sample rod is locally heated and eventually molten. The molten zone can be moved up and down along the entire sample rod under simultaneous rotation. Due to the anisotropic growth velocity a preferential growth of those grains with the fastest growth velocity along the pulling direction is obtained and the formerly polycrystalline rod is transformed into a single crystal. Single crystal growth can be performed with this furnace at maximum temperatures up to 2200°C in the pressure range from  $10^{-5}$  mbar up to 10 bar and in oxidizing, reducing as well as inert atmosphere.



**Figure 4:** The four-mirror image furnace installed at the crystal laboratory of the WMI. Crystals can be grown by the floating zone and traveling solvent floating zone technique at temperatures up to 2200°C and pressures up to 10 bar.

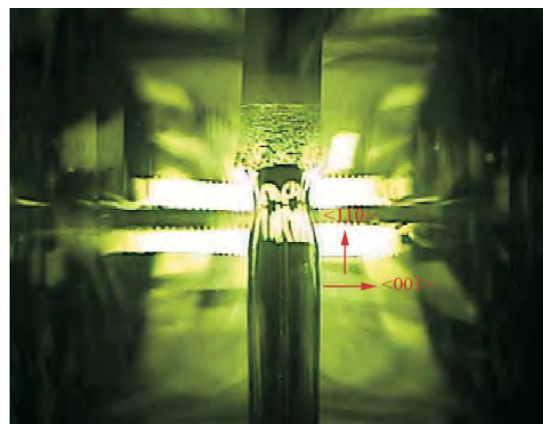
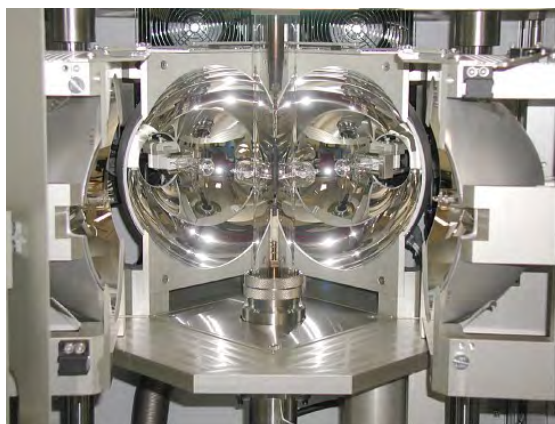


**Figure 5:** Left: Central part of the image furnace with the four elliptical mirrors. In the center one can see the quartz tube with the poly-crystalline rod. Right: View on the molten zone of  $\text{Pr}_{2-x}\text{Ce}_x\text{CuO}_4$  (melting point: 1280°C) obtained by a CCD camera.

## The X-ray diffraction systems

For x-ray analysis the Walther-Meissner-Institute operates two X-ray diffractometers (Bruker D8 Advance and D8 Discover). The two-circle system is used for powder diffraction. In this system the samples can be heated in oxygen atmosphere up to 1600°C. It is equipped with a Göbel mirror and an area detector to save measuring time. The second system is a high resolution four-circle diffractometer that can be used for reciprocal space mappings. It is equipped with a Göbel mirror and an asymmetric two-fold monochromator and allows for the texture analysis of thin film superlattices and single crystalline materials. In both systems measurements can be carried out fully computer controlled.



Figure 6: The two-circle X-ray diffractometer Bruker D8 Advance.

Beyond these two Bruker x-ray systems a Laue camera for single crystal analysis and a Debye-Scherrer camera are available.

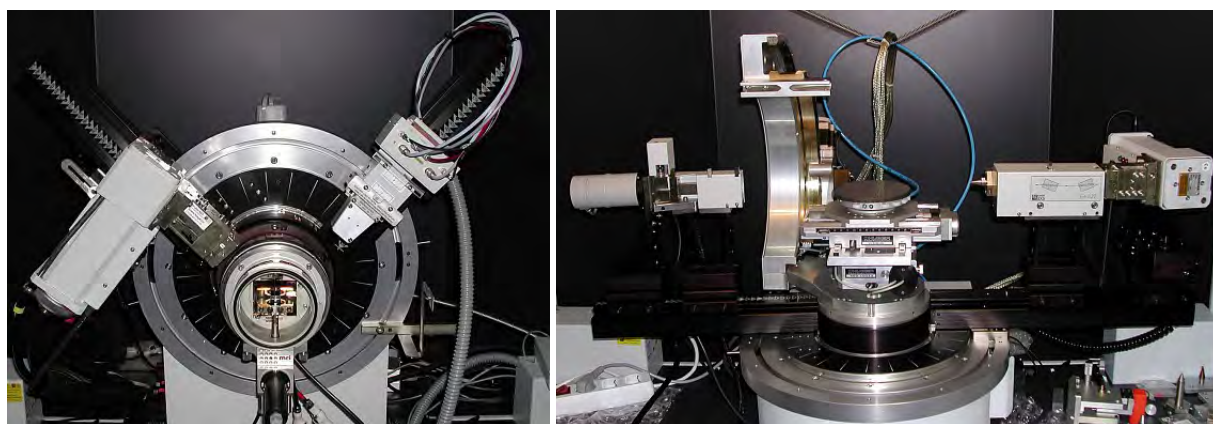


Figure 7: Left: High temperature sample holder of the D8 Advance system. Right: Four-circle high resolution X-ray diffractometer Bruker D8 Discover.



Figure 8: Quantum Design SQUID magnetometer.

### The SQUID-magnetometer

For the analysis of the magnetic properties of materials, a Quantum Design SQUID magnetometer system as shown in Fig. 8 is used at the WMI. The SQUID magnetometer allows for measurements in the temperature regime from 1.5 to 400 K and provides excellent sensitivity particularly in the low field regime. Due to the excellent sensitivity of the system, thin film samples with a very small sample volume can be analyzed. In a special inset, samples can be measured up to temperatures well above room temperature (up to 500°C). For this option the sample volume has to be reduced.

The SQUID magnetometer is equipped with a superconducting solenoid allowing for a maximum field of 7 T. At present, the magnetometer is used for the characterization of magnetic materials (both in bulk and thin film form). Examples are the doped manganites, magnetite, the double perovskites, magnetic semiconductors, or multiferroics.

### The High Field Laboratory

Transport and thermodynamic properties of samples are often studied as a function of applied magnetic field. For such measurements several superconducting magnets are available at the WMI. Two of them (8/10 and 15/17 Tesla magnet system) are located in the high magnetic field laboratory in the basement of the WMI. The magnet systems are lowered below the ground level to facilitate the access

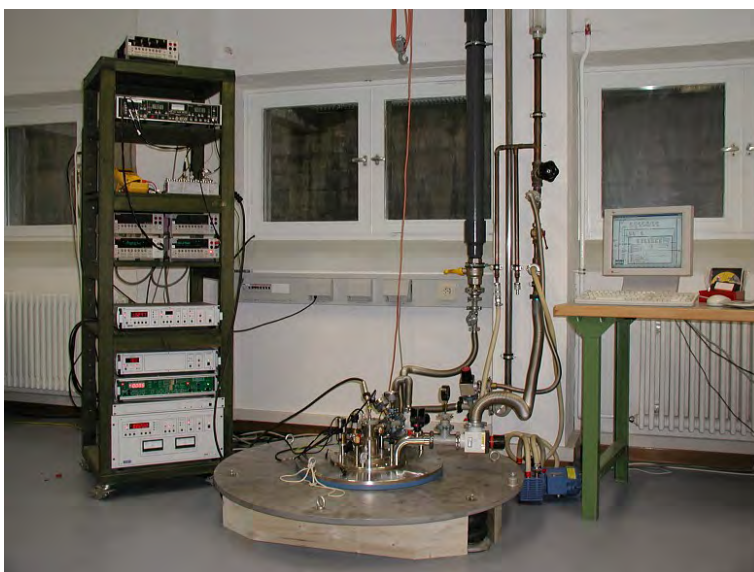


Figure 9: High field laboratory with Oxford 17 T magnet system.

to the top flange and the change of the sample sticks. The magnet systems are decoupled from the building to avoid noise due to mechanical vibrations. A variety of sample holders can be mounted allowing for e.g. sample rotation during the measurement. For standard sample holders the accessible temperature regime is  $1.5 \text{ K} < T < 300 \text{ K}$ . However, also  $^3\text{He}/^4\text{He}$  dilution refrigerator inserts ( $T > 20 \text{ mK}$ ) or high temperature units ( $T < 700 \text{ K}$ ) can be mounted. All measurements are fully computer controlled (by the use of the LabView software tool) allowing for remote control and almost continuous measurements.



**Figure 10:** Top: Part of the clean room facility with optical lithography equipment and clean room benches. Bottom: Resist coater and hot plates.

### The Clean Room Facility

For the fabrication of nanostructures and superconducting as well as spintronic devices the WMI operates a class 1000 clean room facility with an area of about  $50\text{ m}^2$ . This clean room facility has been put into operation at the WMI within the year 2001. The clean room is subdivided into two parts for optical lithography and electron beam lithography, respectively. The clean room facility is equipped with the standard tools for optical lithography such as resist coaters, hot plates, wet benches, a Karl Süss MJB3 mask aligner and an optical projection lithography system. The technical infrastructure for the clean room is located in the basement of the WMI directly below the clean room area.

Since 2005 the clean room also is equipped with a reactive ion etching system, Plasmalab 80 Plus with ICP plasma source (Oxford Instruments Plasma Technology).

### Electron Beam Lithography

The Electron Beam Lithography System is installed in one part of the clean room facility. It consists of a Philips XL 30 SFEG scanning electron microscope (SEM) with a Raith Elphy Plus electron beam lithography system and a laser interferometer table for precise stitching of writing fields.

The SEM is equipped with a hot field emitter and typically provides a beam diameter of less than 1.5 nm at  $\geq 10$  keV or about 2.5 nm at 1 keV. The lithography unit allows the fabrication of nanostructures down to about 10 nm. We have realized the controlled fabrication of metallic strip patterns with a strip width of about 20 nm. The electron beam lithography is used for the fabrication of nanostructures in metallic and oxide systems required for the study of quantum effects in mesoscopic samples.

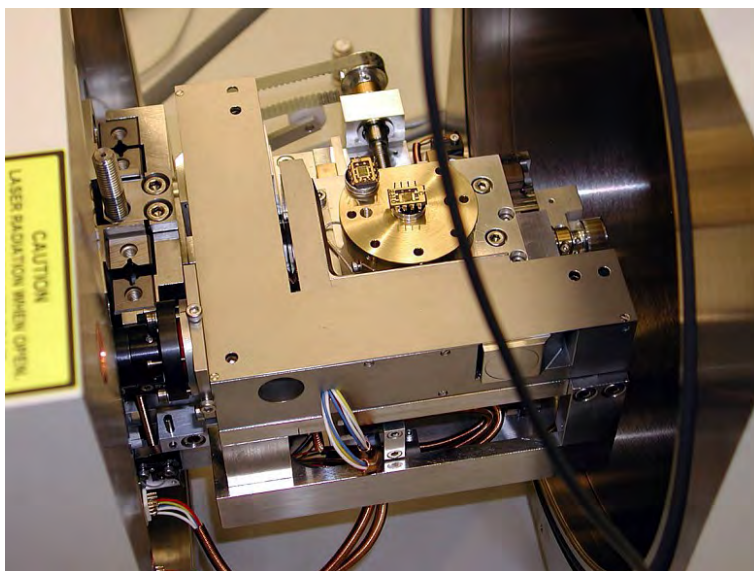
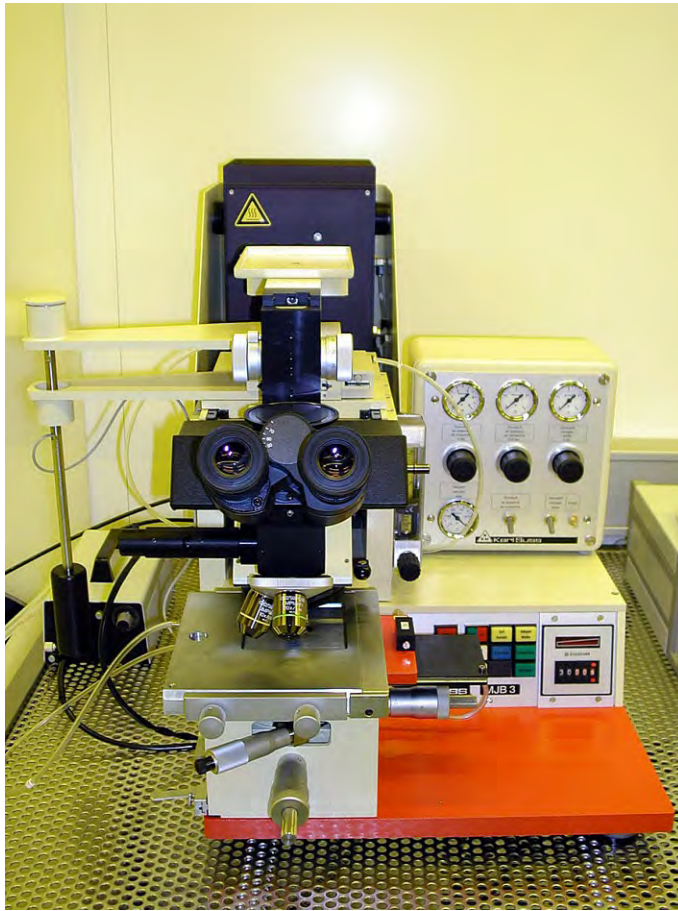


**Figure 11:** Top: Philips XL 30 SFEG Scanning Electron Microscope with Raith Elphy Plus Lithography System. Bottom: Raith Laser Stage.



### Optical Lithography

For optical lithography a Karl Süss MJB 3 maskaligner or an optical microscope based projection system are used. The maskaligner is operating in the 1 : 1 soft or hard contact mode and is using chromium metal masks. In the projection system the mask pattern is demagnified by a factor of 5 to 100. Therefore, cheap foil masks can be used. With both systems microstructures with a lateral dimension down to  $1\mu\text{m}$  can be fabricated.



**Figure 12:** Top: Süss MJB 3 maskaligner for optical lithography. Bottom: Optical projection lithography based on an optical microscope.

### Low and Ultra-low Temperature Facilities

The WMI operates several low and ultra-low temperature facilities that have been developed and fabricated in-house.

The lowest temperature is achieved by the nuclear demagnetization cryostat "Bayerische Millimühle 2". This ultra-low temperature facility consists of an in-house built dilution refrigerator and originally of two nuclear demagnetization stages. The first of those is based on a hyperfine enhanced van Vleck paramagnet  $\text{PrNi}_5$  (0.9 mole), the second, which has been removed a few years ago, was based on purified copper (0.2 mole). The lowest temperature reached with this system was slightly below  $30 \mu\text{K}$  in the copper nuclear spin system. At the moment, the first stage can be cooled to below  $400 \mu\text{K}$  and, due to the large heat capacity of  $\text{PrNi}_5$ , it stays below the mixing chamber temperature (5 mK) for nearly 3 weeks. In this cryostat three measuring sites are provided, two in a magnetic field compensated region and one in the center of an 8 T magnet. They are suitable for specific heat measurements, for capacitive torque- and SQUID magnetometry, as well as for transport measurements (electrical und thermal conductivity). The cryostat is also equipped with a pressure cell for liquid and solid  $^3\text{He}$ , which at the moment is used for nuclear spin resonance measurements below 1 mK.

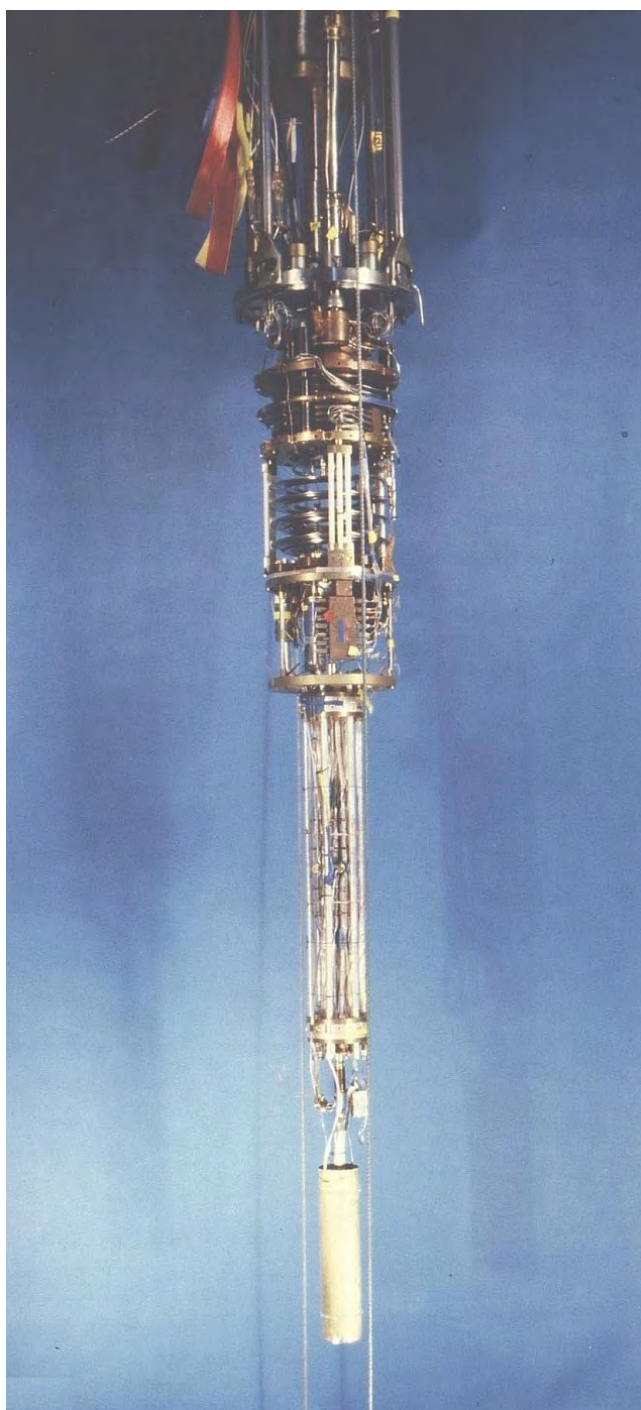


**Figure 13:** The dilution refrigerator and the nuclear demagnetization stage of the nuclear demagnetization cryostat "Bayerische Millimühle 2".

Some years ago, at the WMI, we have constructed the first dilution refrigerator with pulse tube pre-cooling for ultra-low temperature experiments. This type of refrigerator works without cryo-liquids, and thus is a lot more practical, more economical and more reliable than cryostats with liquid helium pre-cooling. These days, all major cryo-engineering firms are offering commercial versions of this milli-Kelvin cooler, and these so-called "dry" refrigerators outsell conventional refrigerators by a wide margin. The general construction concept of most manufacturers is unchanged from our original prototype, where the refrigerator consists of three basic components. The first cooling stage is a commercial pulse tube cryocooler which reaches a base temperature of 2.5 K. The second stage is a Joule-Thomson stage, and the last stage is a dilution refrigeration stage, where the lowest temperature of the cryostat is about 0.01 K (Fig. 14).



**Figure 14:** The "dry" dilution refrigerator of the WMI.



**Figure 15:** Low-temperature unit of a WMI dilution refrigerator ready to go into a cryostat.

The first cooling stage is a commercial pulse tube cryocooler which reaches a base temperature of 2.5 K. The second stage is a Joule-Thomson stage, and the last stage is a dilution refrigeration stage, where the lowest temperature of the cryostat is about 0.01 K (Fig. 14).

In many low temperature applications high refrigeration capacities are required. Our design allows for a high circulation rate of  $^3\text{He}$  which in the end determines the cooling power of a dilution refrigerator. Presently our "dry" fridge reaches a refrigeration capacity of  $700 \mu\text{W}$  at a temperature of the mixing chamber of 0.1 K, seven times the cooling power of the WMI nuclear demagnetization cryostat. Goals of our present work are a further increase of cooling power and a lower base temperature of the dry dilution refrigerator.



**Figure 16:** Two mixing chamber mounting plates with silver sponges. Those are needed to overcome the thermal resistance (Kapitza resistance) between the liquid  $^3\text{He}$  and the mounting plate of the mixing chamber. To fabricate the mounting of the sponge (square pins embedded in the sponge) a spark erosion technique has been employed.

A smaller version of our cryogen-free fridge has become commercially available at VeriCold Technologies, Ismaning. It has a refrigeration capacity of  $250 \mu\text{W}$  at a mixing chamber temperature of 0.1 K (Fig.15).

The WMI also develops and fabricates dilution refrigerator inserts for temperatures down to about 20 mK. The inserts fit into all cryogenic systems (e.g. superconducting magnets) having a two inch bore. They allow fast sample change and rapid cool down cycles of less than five hours.

The dilution refrigerator inserts are engineered and fabricated in-house and are also provided to other low temperature laboratories for ultra low temperature experiments.

## Low Temperature Scanning Tunneling Microscope with Ultra-High-Vacuum Characterization and Preparation Facilities

The low temperature scanning tunneling microscope allows investigation of low dimensional systems such as self-organized molecules, superconductors, magnetic and hetero-structure surfaces. The LT-STM is integrated into an ultra-high vacuum (UHV) chamber together with a variety of analytical as well as preparation tools. A newly added Quartz-Crystal-Microbalance allows quantitative controlling of evaporation processes. Monitoring is possible from island growth up to a film thickness of hundreds of atomic layers. The Hermann-group operates the LT-STM and the here listed preparation facilities in laboratory 028 at the WMI. B. A. Hermann is junior Principle Investigator of the excellence cluster Nanosystems Initiative Munich (NIM) and member of the Center for Nano Science (CeNS).

### The Low Temperature Scanning Tunneling Microscope

The LT-STM (see figure 17 a) is designed for easy handling under UHV as well as low temperature conditions. We control the Omicron STM by an electronics of the RHK company (see figure 17 b).

Following, the technical features are listed:

- In-situ sample and tip exchange (manipulator see Figure 18 a).
- Vibration isolation ensured by a spring suspension system with eddy current damping and pneumatic damping legs.
- Variable temperatures from 5 K (pumped 2 K) up to room temperature ( $\approx 300$  K).
- Fast system cool-down (5 K within  $\approx 6$  hours).
- Sample pre-cooling to 50 K on the manipulator stage.
- Fast sample cool-down (5 K within  $\approx 2$  hours).
- On-line optical access and on-line four terminal transport measurements.
- Up to 6 samples can be stored at low temperature (77 K).

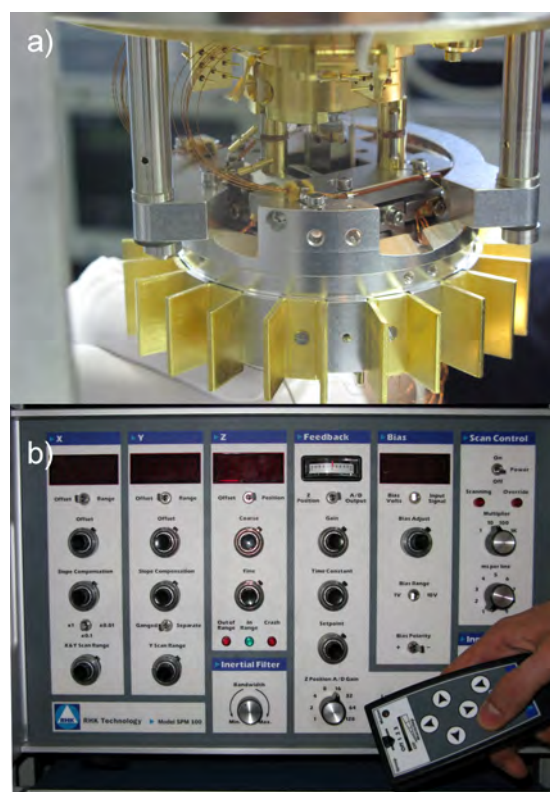


**Figure 17:** a) Inner view on the STM displaying part of the damping system, various cables and the scanning head (barely visible in the middle above the well). b) Photograph of our RHK scan electronic.

### Preparation and Characterization Facilities

In addition to the LT-STM analysis chamber a second UHV chamber allows for sample preparation and characterization under UHV-conditions. Substrates can be prepared by an argon sputter gun and thermal annealing. A three crucible evaporator allows the deposition of

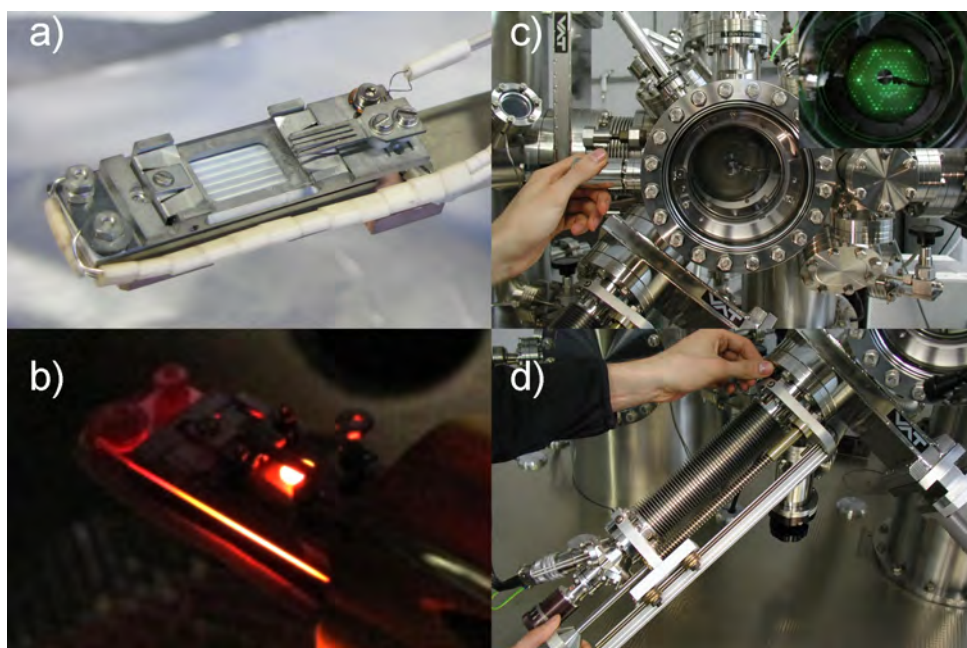


**Figure 18:** a) Close up on the manipulator for sample handling in the UHV chamber. b) Manipulator with Si-sample at 510°C under UHV conditions. The body of the manipulator is cooled to prevent damage. c) LEED spectrometer; inset LEED-diffraction image of the Si [111]  $7 \times 7$  reconstruction. d) Photograph of the evaporator.

molecules onto the surface; the deposition process is controlled by a quartz crystal microbalance. For sample characterization low-energy-electron-diffraction (LEED) and quadrupole mass spectrometry are available.

**Argon Sputter Gun:** Inside the preparation chamber clean single crystalline substrates are prepared by ion-sputtering and subsequent thermal annealing, which can be controlled by a three-grid low energy electron diffractometer (LEED) (see below) in a vacuum of  $10^{-11}$  mbar.

**Sample Heating/Cooling Stage:** On the manipulator (see figure 18 a) samples can be prepared by direct current and indirect heating (see figure 18 b). Sample temperatures of up to 1073 K can be realized and the sample can be cooled to 50 K before transferring to the STM.

**Low Energy Electron Diffraction (LEED):** The surface ordering of (reconstructed) substrate/single crystal surfaces or molecular ad-layers can be analyzed by low energy electron diffraction (see figure 18 c).

**Evaporator for Organic Material:** A microprocessor controlled evaporator allows deposition of up to three different organic materials at the same time (see figure 18 d). Crucibles are refilled without breaking the vacuum of the main chamber.

**Quartz-Crystal-Microbalance:** For controlling the evaporation process and quantitative measurements of the number of adsorbed layers on/coverage of the substrate during evaporation a quartz-crystal-microbalance was recently added. Growth rates of 0.01 nm/s corresponding to a frequency change of 0.03 Hz/s can be monitored.

**Quadrupole Mass Spectrometer:** Samples are additionally characterized by desorption spectroscopy with a quadrupole mass spectrometer. The desorbing molecules are ionized in a crossbeam ion source and accelerated in the quadrupole mass spectrometer, which either uses a Faraday cup or secondary electron multiplier (SEM) as detector with a mass resolution up to 2048 u.

Multiple additional vacuum ports allow further extensions of the Omicron STM in the future.

**Tip etching facility (ex situ):** The standard procedure for preparing STM tips - suitable for

STM measurements - is cutting a PtIr-wire with scissors. Other tip materials (e.g. Tungsten, Gold, Niobium, . . .) have to be etched in order to form the necessary tip radii. A newly constructed tip etching facility allows for more tip materials than PtIr opening up the possibility of usage of e.g. superconducting tips.

### Magnetic Field Low Temperature Ultra-High-Vacuum (UHV) Scanning Tunneling Microscope (STM)

Built under the guidance of B. A. Hermann in the group of Prof. Dr. H.-J. Güntherodt in Basel, the system was transferred and put into operation in 2006; it complements the Omicron LT-STM operated at the WMI in Munich. The high stability of the instrument, the magnetic field as well as temperatures as low as 2.7 K allow the investigation of high temperature superconductors (HTSC) and organic superconductors. In a collaboration with A. Erb, R. Hackl as well as M. Kartsovnik and W. Biberacher, the group of B. A. Hermann currently investigates high-temperature superconductors and  $ET_2Cu(NCS)_2$ .

The STM is optimized for low temperature tunneling imaging and spectroscopy in high magnetic fields under UHV-conditions (see figure 19). A home-built electronics allows tunneling spectroscopy at points along lines, in grids and in a high density modus.



**Figure 19:** The current setup of the instrument: visible is the cryostat with microscope inside, as well as parts of the control electronics.

#### Technical Features of the STM:

- Imaging resolution:  
0.01 nm in  $x - y$ -direction and  
0.005 nm in  $z$ -direction.
- Current-voltage spectroscopy ( $I - V$ )  
(voltage resolution: 0.05 meV).
- Current-distance curves ( $I - d$ ).
- Maximum scan size:  $1 \mu\text{m} \times 1 \mu\text{m}$  at 4.2 K.
- Superconducting magnet up to 4 T with  
persistent switch.
- Vibration damping through spring sus-  
pension.
- Temperature range from room tempera-  
ture down to liquid helium temperature  
at 4.2 K (pumped 2.7 K).
- Cryostat with LHe durability of one week  
(without thermal load).

## Publications

- Circuit quantum electrodynamics in the ultrastrong-coupling regime**  
T. Niemczyk, F. Deppe, H. Huebl, E. P. Menzel, F. Hocke, M. J. Schwarz, J. J. Garcia-Ripoll, D. Zueco, T. Hümmer, E. Solano, A. Marx, R. Gross  
[Nature Physics 6, 772–776 \(2010\)](#).
- Single-shot readout of an electron spin in silicon**  
A. Morello, J.J. Pla, F.A. Zwannenburg, K.W. Chan, K.Y. Tan, H. Hübl, M. Möttönen, C.D. Nugroho, C. Yang, J.A. van Donkelaar, A.D.C. Alves, D.N. Jamieson, C.C. Escott, L.C.L. Hollenberg, R.G. Clark, A.S. Dzurak  
[Nature 467, 687–691 \(2010\)](#).
- Magnetic breakdown in the electron-doped cuprate superconductor  $\text{Nd}_{2-x}\text{Ce}_x\text{CuO}_4$ : the reconstructed Fermi surface survives in the strongly overdoped regime**  
T. Helm, M.V. Kartsovnik, I. Sheikin, M. Bartkowiak, F. Wolff-Fabris, N. Bittner, W. Biberacher, M. Lambacher, A. Erb, J. Wosnitzer, R. Gross,  
[Phys. Rev. Lett. 105, 247002 \(2010\)](#).
- Dual-path state reconstruction scheme for propagating quantum microwaves and detector noise tomography**  
E. P. Menzel, F. Deppe, M. Mariani, M. Á. Araque Caballero, A. Baust, T. Niemczyk, E. Hoffmann, A. Marx, E. Solano, R. Gross  
[Phys. Rev. Lett. 105, 100401 \(2010\)](#).
- Planck Spectroscopy and the Quantum Noise of Microwave Beam Splitters**  
M. Mariani, E.P. Menzel, M.A. Araque Caballero, A. Baust, F. Deppe, T. Niemczyk, E. Hoffmann, A. Marx, E. Solano, R. Gross  
[Phys. Rev. Lett. 105, 133601 \(2010\)](#).
- Spin-dependent recombination between phosphorus donors in silicon and Si/SiO<sub>2</sub> interface states investigated with pulsed electrically detected electron double resonance**  
F. Hoehne, H. Hübl, B. Galler, M. Stutzmann, M.S. Brandt,  
[Phys. Rev. Lett. 104, 046402 \(2010\)](#).
- Femtosecond Response of Quasiparticles and Phonons in Superconducting  $\text{YBa}_2\text{Cu}_3\text{O}_{7-\delta}$  Studied by Wideband Terahertz Spectroscopy**  
A. Pashkin, M. Porer, M. Beyer, K. W. Kim, A. Dubroka, C. Bernhard, X. Yao, Y. Dagan, R. Hackl, A. Erb, J. Demsar, R. Huber, and A. Leitenstorfer  
[Phys. Rev. Lett. 105, 067001 \(2010\)](#).
- Droplet-like Fermi surfaces in the anti-ferromagnetic phase of  $\text{EuFe}_2\text{As}_2$ , an Fe-pnictide superconductor parent compound**  
S. de Jong, E. van Heumen, S. Thirupathiah, R. Huisman, F. Massee, J. B. Goedkoop, R. Ovsyanikov, J. Fink, H. A. Duerr, A. Gloskovskii, H.S. Jeevan, P. Gegenwart, A. Erb, L. Patthey, M. Shi, R. Follath, A. Varykhalov, M. S. Golden  
[Europhys. Lett. 89, 27007 \(2010\)](#).
- Molecular Jigsaw: Pattern Diversity Encoded by Elementary Geometrical Features**  
C. Rohr, M. Balb Gamba, K. Gruber, E. C. Constable, E. Frey, T. Franosch, and B. A. Hermann  
[Nano Letters 10 \(3\), 833–837 \(2010\)](#).
- Electric field controlled manipulation of the magnetization in Ni/BaTiO<sub>3</sub> hybrid structures**  
S. Geprägs, A. Brandlmaier, M. Opel, R. Gross, S.T.B. Goennenwein  
[Appl. Phys. Lett. 96, 142509 \(2010\)](#).
- A Superconducting 180° Hybrid Ring Coupler for Circuit Quantum Electrodynamics**  
E. Hoffmann, F. Deppe, T. Niemczyk, T. Wirth, E. P. Menzel, G. Wild, H. Hübl, M. Mariani, T. Weißl, A. Lukashenko, A. P. Zhuravel, A. V. Ustinov, A. Marx, and R. Gross  
[Appl. Phys. Lett. 97, 222508 \(2010\)](#).
- Electron spin resonance of  $\text{Zn}_{1-x}\text{Mg}_x\text{O}$  thin films grown by plasma-assisted molecular beam**

- epitaxy**  
T.A. Wassner, B. Laumer, M. Althammer, S.T.B. Gönnenwein, M. Stutzmann, M. Eickhoff, M.S. Brandt,  
[Appl. Phys. Lett. 97, 092102 \(2010\)](#).
13. **Mesoscopic shelving readout of superconducting qubits in circuit quantum electrodynamics**  
B.G.U. Englert, G. Mangano, M. Mariani, R. Gross, J. Siewert, and E. Solano,  
[Phys. Rev. B 81, 134514 \(2010\)](#).
  14. **Two-resonator Circuit QED: Dissipative Theory**  
Georg M. Reuther, David Zueco, Frank Deppe, Elisabeth Hoffmann, Edwin P. Menzel, Thomas Weißl, Matteo Mariani, Sigmund Kohler, Achim Marx, Enrique Solano, Rudolf Gross, Peter Hänggi  
[Phys. Rev. B 81, 144510 \(2010\)](#).
  15. **Temperature-pressure phase diagram and electronic properties of the organic metal  $\kappa$ -(BETS)<sub>2</sub>Mn[N(CN)<sub>2</sub>]<sub>3</sub>**  
V.N. Zverev, M.K. Kartsovnik, W. Biberacher, S.S. Khasanov, R.P. Shibaeva, L. Quahab, L. Toupet, N.D. Kushch, E.B. Yagubskii, E. Canadell,  
[Phys. Rev. B 82, 155123 \(2010\)](#).
  16. **Molecular self-organization: Predicting the pattern diversity and lowest energy state of competing ordering motifs**  
B.A. Hermann, C. Rohr, M. Balbás Gamba, A. Malecki, M.S. Malarek, E. Frey, T. Franosch,  
[Phys. Rev. B 82, 165451 \(2010\)](#).
  17. **Pinpointing Gap Minima in Ba(Fe<sub>0.94</sub>Co<sub>0.06</sub>)<sub>2</sub>As<sub>2</sub> via Band Structure Calculations and Electronic Raman Scattering**  
I. I. Mazin, T. P. Devereaux, J. G. Analytis, Jiun-Haw Chu, I. R. Fisher, B. Muschler, R. Hackl  
[Phys. Rev. B 82, 180502 \(2010\)](#).
  18. **Electron tunnel rates in a donor-silicon single electron transistor hybrid**  
Hans Huebl, Christopher D. Nugroho, Andrea Morello, Christopher C. Escott, Mark A. Eriksson, Changyi Yang, David N. Jamieson, Robert G. Clark, and Andrew S. Dzurak  
[Phys. Rev. B 81, 235318 \(2010\)](#).
  19. **Raman scattering evidence for a cascade evolution of the charge-density-wave collective amplitude mode**  
M. Lavagnini, H.-M. Eiter, L. Tassini, B. Muschler, R. Hackl, R. Monnier, J.-H. Chu, I. R. Fisher, and L. Degiori  
[Phys. Rev. B 81, 081101 \(2010\)](#).
  20. **Orbital character variation of the Fermi surface and doping dependent changes of the dimensionality in BaFe<sub>2-x</sub>Co<sub>x</sub>As<sub>2</sub> from angle-resolved photoemission spectroscopy**  
S. Thirupathiah, S. de Jong, R. Ovsyannikov, H. A. Dürr, A. Varykhalov, R. Follath, Y. Huang, R. Huisman, M. S. Golden, Yu-Zhong Zhang, H. O. Jeschke, R. Valentí, A. Erb, A. Gloskovskii, and J. Fink  
[Phys. Rev. B 81, 104512 \(2010\)](#).
  21. **Magnetic interference patterns in  $0$ - $\pi$ -SIFS Josephson junctions: Effects of asymmetry between  $0$  and  $\pi$ -regions**  
M. Kemmler, M. Weides, M. Weiler, M. Opel, S. T. B. Goennenwein, A. S. Vasenko, A. A. Golubov, H. Kohlstedt, D. Koelle, R. Kleiner, E. Goldobin  
[Phys. Rev. B 81, 054522 \(2010\)](#).
  22. **Advanced Spectroscopic Synchrotron Techniques to Unravel the Intrinsic Properties of Dilute Magnetic Oxides: the Case of Co:ZnO**  
A. Ney, M. Opel, T.C. Kaspar, V. Ney, S. Ye, K. Ollefs, T. Kammermeier, S. Bauer, K.-W. Nielsen, S. T. B. Goennenwein, M. H. Engelhard, S. Zhou, K. Potzger, J. Simon, W. Mader, S. M. Heald, J. C. Cezar, F. Wilhelm, A. Rogalev, R. Gross and S. A. Chambers  
[New J. Phys. 12, 013020 \(2010\)](#).

23. **Towards a better understanding of superconductivity at high transition temperatures**  
R. Hackl, W. Hanke  
[Eur. Phys. J. Special Topics 188, 3-14 \(2010\).](#)
24. **Quantitative comparison of single- and two-particle properties in the cuprates**  
W. Prestel, F. Venturini, B. Muschler, I. Tütto, R. Hackl, M. Lambacher, A. Erb, Seiki Komiya, Shimpei Ono, Yoichi Ando, D. Inosov, V.B. Zabolotnyy, and S.V. Borisenko  
[Eur. Phys. J. Special Topics 188, 163-171 \(2010\).](#)
25. **Advances in single crystal growth and annealing treatment of electron-doped HTSC**  
Michael Lambacher, Toni Helm, Mark Kartsovnik, Andreas Erb  
[Eur. Phys. J. Special Topics 188, 61-72 \(2010\).](#)
26. **Electron interactions and charge ordering in CuO<sub>2</sub> compounds**  
B. Muschler, W. Prestel, L. Tassini, R. Hackl, M. Lambacher, A. Erb, Seiki Komiya, Yoichi Ando, D.C. Peets, W.N. Hardy, R. Liang, and D.A. Bonn  
[Eur. Phys. J. Special Topics 188, 131-152 \(2010\).](#)
27. **Novel Multifunctional Materials Based on Oxide Thin Films and Artificial Heteroepitaxial Multilayers**  
M. Opel, S. Geprägs, E.P. Menzel, A. Nielsen, D. Reisinger, K.-W. Nielsen, A. Brandlmaier, F.D. Czeschka, M. Althammer, M. Weiler, S.T.B. Goennenwein, J. Simon, M. Svete, Wentao Yu, S.-M. Hühne, W. Mader, R. Gross  
[Phys. Status Solidi A , 1-20 \(2010\).](#)
28. **A systematic study of optical and Raman spectra of peapod-based DWNTs**  
B. Botka, Á. Pekker, Á. Botos, K. Kamarás, R. Hackl,  
[Phys. Stat. Sol. B 247, 2843 - 2846 \(2010\).](#)
29. **Infrared and Raman investigation of carbon nanotube-polyallylamine hybrid systems**  
Hajnalka-Mária Tóháti, Bea Botka, Katalin Németh, Áron Pekker, Rudi Hackl, Katalin Kamarás  
[Phys. Status Solidi b 247, 2884-2886 \(2010\).](#)
30. **An Electron-boson Glue Function Derived from Electronic Raman Scattering**  
B. Muschler, W. Prestel, E. Schachinger, J. P. Carbotte, R. Hackl, Shimpei Ono, and Yoichi Ando  
[J. Phys.: Condens. Matter 22, 375702 \(2010\).](#)
31. **Skymion lattices in metallic and semiconducting B<sub>20</sub> transition metal compounds**  
C. Pfleiderer, T. Adams, A. Bauer, W. Biberacher, B. Binz, F. Birkelbach, P. Böni, C. Franz, R. Georgii, M. Janoschek, F. Jonietz, T. Keller, R. Ritz, S. Mühlbauer, W. Münzer, A. Neubauer, B. Pedersen, and A. Rosch  
[J. Phys.: Condens. Matter 22, 164207 \(2010\).](#)
32. **Advanced techniques for all-electrical spectroscopy on spin caloric phenomena**  
R. Huber, P. Klemm, S. Neusser, B. Botters, A. Wittmann, M. Weiler, S.T.B. Goennenwein, C. Heyn, M. Schneider, P. Böni, D. Grundler  
[Sol. State Com. 150, 492-495 \(2010\).](#)
33. **Voltage-controlled spin mechanics**  
S.T.B. Goennenwein  
[Europhysics News 41 \(4\), 17-20 \(2010\).](#)
34. **Superconductivity**  
R. Gross  
in *Electronic Oxides – Correlation Phenomena, Exotic Phases and Novel Functionalities*, Schriften des Forschungszentrums Jülich, Reihe Schlüsseltechnologien/Key Technologies, Band 13, A11.1 - A11.43 (2010).  
ISSN 1866-1807, ISBN 978-3-89336-609-5
35. **Superconductivity of Calcium C<sub>60</sub> Intercalation Compound Synthesized by Shock-Wave Pressure**  
Yu. A. Ossipyan, N. S. Sidorov, A. V. Palnichenko, O. M. Vyaselev, M. V. Kartsovnik, M. Opel, V.

- V. Avdonin, D. V. Shakhrai, V. E. Fortov  
[Fullerenes, Nanotubes and Carbon Nanostructures 18, 376-380 \(2010\).](#)
36. **Concept of a powerful cryogen-free dilution refrigerator with separate 1 K stage**  
K. Uhlig,  
[Cryocoolers 16, 509 \(2010\).](#)
37. **Improved Design of the Intermediate Stage of a Dry Dilution Refrigerator**  
K. Uhlig,  
Advances in Cryogenic Engineering 55 A, 641 (2010).
38. **Josephson Coupling and Fiske Dynamics in Ferromagnetic Tunnel Junctions**  
G. Wild, Ch. Probst, A. Marx, R. Gross  
Eur. Phys. J. B, in press (2010).
39. **Fermi Surface of the Electron-doped Cuprate Superconductor  $\text{Nd}_{2-x}\text{Ce}_x\text{CuO}_4$  Probed by High-field Magnetotransport**  
M.V. Kartsovnik, T. Helm, C. Putzke, F. Wolff-Fabris, I. Sheikin, S. Lepault, C. Proust, D. Vignolles, N. Bittner, W. Biberacher, A. Erb, J. Wosnitza, R. Gross,  
New J. Phys., in press (2010).
40. **Intercalation and Dynamics of Hydrated  $\text{Fe}^{2+}$  in the Vermiculites from Santa Olalla and Ojén, dedicated to the 75th Birthday from Prof. Dr. R. Schöllhorn**  
A. Lerf, F.E. Wagner, J. Poyato, J.-L. Pérez-Rodríguez,  
J. Sol. State Electrochem., in press (2010).
41. **Electroelastic hyperfine tuning of phosphorus donors in silicon**  
L. Dreher, T.A. Hilker, A. Brandlmaier, S.T.B. Gönnenwein, H. Hübl, M. Stutzmann, M.S. Brandt,  
Phys. Rev. Lett., accepted for publication (2010).
42. **Acoustically driven ferromagnetic resonance**  
Mathias Weiler, Lukas Dreher, Christian Heeg, Hans Huebl, Rudolf Gross, Martin S. Brandt, Sebastian T.B. Goennenwein  
[arXiv:1009.5798v1](#), submitted for publication (2010).
43. **Magnetic microstructure and magnetotransport in  $\text{Co}_2\text{FeAl}$  Heusler compound thin films**  
Mathias Weiler, Franz D. Czeschka, Inga-Mareen Imort, Günter Reiss, Andy Thomas, Georg Woltersdorf, Rudolf Gross, Sebastian T. B. Goennenwein  
[arXiv:1011.1417](#), submitted for publication (2010).
44. **Kinetic theory for response and transport in non-centrosymmetric superconductors**  
Ludwig Klam, Dirk Manske, Dietrich Einzel  
[arXiv:1003.0407](#), submitted for publication (2010).
45. **Scaling behavior of the spin pumping effect in ferromagnet/platinum bilayers**  
F. D. Czeschka, L. Dreher, M. S. Brandt, M. Weiler, M. Althammer, I.-M. Imort, G. Reiss, A. Thomas, W. Schoch, W. Limmer, H. Huebl, R. Gross, and S. T.B. Goennenwein  
[arXiv:1012.3017](#), submitted for publication (2010).
46. **Magnetic Transformations in the Organic Conductor  $\kappa-(\text{BETS})_2\text{Mn}[\text{N}(\text{CN})_2]_3$  at the Metal-Insulator Transition**  
O.M. Vyaselev, M.V. Kartsovnik, W. Biberacher, L.V. Zorina, N.D. Kushch, E.B. Yagubskii,  
[arXiv:1011.5730](#), submitted for publication (2010).
47. **Observation of a first-order phase transition deep within the vortex-solid region of  $\text{YBa}_2\text{Cu}_3\text{O}_7$**   
M. Reibel, S. Weyeneth, A. Erb, A. Schilling,  
Phys. Rev. Lett., submitted for publication (2010).
48. **Unravelling the glue and the competing order in superconducting cuprates**  
S. Caprara, C. Di Castro, B. Muschler, R. Hackl, M. Lambacher, A. Erb, S. Komiya, Y. Ando, M. Grilli,  
[arXiv:1010.0180](#), submitted for publication (2010).

## **Theses, Appointments, Honors and Awards, Membership in Advisory Boards, etc.**

### **Completed and ongoing Ph.D. Theses**

1. **Effizientes Design von Planar-Transformatoren**  
Thomas Florian Goßner, April 2010.
2. **Supraleitende Quantenbits mit Supraleiter-Ferromagnet-Supraleiter Josephson-Kontakten**  
Georg Wild, TU München, seit September 2004.
3. **Spin-Engineering in funktionalen Schichtsystemen aus Übergangsmetalloxiden**  
Stephan Geprägs, TU München, seit Oktober 2004.
4. **Untersuchung der Wechselwirkungspotenziale in Kupratsupraleitern durch quantitativen Vergleich spektroskopischer Resultate**  
Wolfgang Prestel, TU München, seit November 2004.
5. **Kohärente Dynamik und Dekohärenz in supraleitenden Quantenbits**  
Edwin Menzel, TU München, seit Januar 2006.
6. **Quantenelektrodynamik mit supraleitenden Schaltkreisen**  
Thomas Niemczyk, TU München, seit Juli 2006.
7. **Multiferroisches Verhalten und steuerbarer Magnetismus in oxidischen Heterostrukturen**  
Andreas Brandlmaier, TU München, seit Dezember 2006.
8. **Tiefemperatur-Rastersondenmikroskopie an Molekülsystemen und Nanotubes**  
Carsten Rohr, LMU München, seit Januar 2007.
9. **Hybride Nanostrukturen auf der Basis von Materialsystemen mit elektronischen Korrelationen**  
Franz Czeschka, TU München, seit Juli 2007.
10. **(Bio) Sensorik mit Cantileverarrays und Oberflächenkontrolle mittels Rastersondentechniken**  
Kathrin Gruber, LMU München, seit November 2007.
11. **Korrelierte Systeme untersucht mit Tiefemperatur-Rastersondenmikroskopie**  
Johannes Büttner, LMU München, seit Januar 2008.
12. **Magnetotransporteigenschaften von dünnen ferromagnetischen Schichten und Heterostrukturen**  
Mathias Weiler, TU München, seit Februar 2008.
13. **Untersuchung von Kupraten nahe des Einsatzpunktes der Supraleitung**  
Bernhard Muschler, seit Februar 2008.
14. **Multifunktionale magnetische Heterostrukturen**  
Matthias Althammer, TU München, seit April 2008.
15. **Herstellung und Charakterisierung von supraleitenden Schaltkreisen zur Realisierung von gekoppelten supraleitenden Quantenbauelementen**  
Elisabeth Hoffmann, TU München, seit April 2008.
16. **Quantenexperimente mit elektromechanischen Systemen**  
Fredrik Hocke, TU München, seit Mai 2008.
17. **Wechselwirkung zwischen Spin-, Gitter- und Ladungsfreiheitsgraden in korrelierten Metallen ohne Inversionszentrum**  
Hans-Martin Eiter, TU München, seit Oktober 2008.

18. **Untersuchung der Fermi-Fläche von Hochtemperatur-Supraleitern**  
Toni Helm, TU München, seit März 2009.
19. **All Optical Quantum Computing**  
Max Häberlein, TU München, seit Dezember 2009.
20. **Raman-Untersuchungen an stark korrelierten Systemen mit hoher Ortsauflösung**  
Florian Kretschmar, TU München, seit Januar 2010.
21. **Vibrational Investigations of Luminescence Molecules**  
Nitin Chelwani, TU München, seit September 2010.
22. **Light-matter Interaction and Coherent Dynamics of Superconducting Circuit QED Systems**  
Alexander Baust, TU München, seit Oktober 2010.

## Completed and ongoing Diploma, Bachelor, Master Theses

1. **Two-Resonator Circuit-QED: Two Coupled Resonators on a Chip**  
Thomas Michael Weißl, Januar 2010.
2. **Spin Mechanics at Radio Frequencies**  
Christian Heeg, Mai 2010.
3. **Characterization of Flux-driven Josephson Parametric Amplifiers**  
Alexander Baust, August 2010.
4. **Surface Plasmons in Magnetic Multilayers**  
Themistoklis Sidiropoulos, Oktober 2010.
5. **Growth and Characterization of Ferromagnetic Heusler Compounds Thin Films**  
Alexander Krupp, Dezember 2010.
6. **Breitbandspektroskopie ferromagnetischer Mikrostrukturen bei tiefen Temperaturen**  
Martin Radlmeier, Dezember 2010.
7. **Untersuchung von korrelierten Elektronensystemen unter hohem Druck**  
Reinhard Roßner, Dezember 2010.
8. **Pressure-dependent Effective Thermal Conductivity of Perlite and its Application in Long-term Thermal Storage**  
Matthias Demharter, seit September 2010.
9. **Characterization of Josephson Parametric Amplifier Modules with Integrated Magnetic Bias**  
Felix Bilger, seit Oktober 2010.
10. **A Tunable Beam Splitter for Circuit-QED Experiments**  
Karl-Friedrich Wulschner, seit November 2010.
11. **Gradiometric Flux Quantum Bits with Tunable Tunnel Coupling**  
Jan Goetz, seit November 2010.
12. **Interlayer Magnetoresistance of the Quasi-twodimensional Charge Density Wave Superconductor  $\alpha$ -(BEDT-TTF)<sub>2</sub>KHg(SCN)<sub>4</sub> at Low Temperatures**  
Michael Kunz, seit November 2010.
13. **Herstellung und Charakterisierung von ZnO/Fe<sub>3</sub>O<sub>4</sub> Heterostrukturen für die Spininjektion**  
Eva-Maria Karrer-Müller, seit November 2010.
14. **Ferromagnetische Resonanz bei tiefen Temperaturen**  
Christoph Zollitsch, seit November 2010.
15. **Untersuchung der Voraussetzung für Supraleitung in FeAs-Verbindungen**  
Andreas Baum, seit Dezember 2010.

## Honors and Awards

### Rotary Prize “Hofgarten” of the Bavarian Academy of Sciences and Humanities

Dr. Achim Marx of WMI received the *Rotary Prize “Hofgarten” 2010* of the Bavarian Academy of Sciences and Humanities in recognition of his pioneering work on solid state nanostructures and their application in quantum information processing systems. The research work of Dr. Marx resulted in important new scientific findings on the coherent dynamics of solid state nanostructures and the foundations of light-matter interaction. His work received broad international attention and is of particular relevance for the development of novel information and communication systems based on quantum mechanical principles.

The Bavarian Academy annually gives the Rotary Prize “Hofgarten” for the promotion of young scientists in all disciplines. The prize has been presented to Achim Marx on December 4, 2010 by the president of the Academy within an Annual Meeting of the Bavarian Academy of Sciences and Humanities in the Munich Residence.



Achim Marx (right) with the President of the Bavarian Academy (left).

### Appointments, Membership in Advisory Boards, etc.

1. **Rudolf Hackl** was member of the Advisory Board of the Conference "Low Energy Electron Dynamics LEES 2010"
2. **Rudolf Gross** is member of the Scientific Advisory Board of the Leibniz Institute for Solid-State and Materials Research, Dresden.
3. **Rudolf Gross** is member of the Kuratorium of the Physik Journal of the German Physical Society.
4. **Rudolf Gross** is member of the selection committee of the Stern-Gerlach-Medal of the German Physical Society.
5. **Rudolf Gross** is spokesman of the division *Low Temperature Physics* of the Condensed Matter Section of the German Physical Society.
6. **Sebastian Gönnerwein** is associate member of the Cluster of Excellence *Nanosystems Initiative Munich (NIM)*.
7. **Rudolf Gross** member of the Executive Board of the Cluster of Excellence *Nanosystems Initiative Munich (NIM)* and coordinator of the Research Area 1 on *Quantum Nanosystems*.
8. **Werner Biberacher** is member of the Selection Panel EuroMagNet II of the Joint European High Magnetic Field Laboratories.
9. **Dietrich Einzel** is one of the four spokesmen of the scientific staff of the Bavarian Academy of Sciences and Humanities.
10. **Rudolf Gross** is member of the International Advisory Board of the Institute for Nanoscale Physics and Chemistry (INPAC), which has been established by the Katholieke Universiteit Leuven in 2006 in the framework of its Excellence Programme.
11. **Rudolf Gross** is member of the Board of Editors of the European Physical Journal B.
12. **Rudolf Gross** is member of the Board of Editors of Physica C.



## Research Projects and Cooperations

A large number of our research projects are benefiting from the collaboration with external groups in joint research projects, as well as from individual collaborations, exchange programs and visitors. Most collaborations are based on joint projects, which are funded by different research organizations (see list below). A considerable number of collaborations also exists with universities, other research institutions and industry without direct financial support.

### Funded Projects

#### German Research Foundation: Excellence Initiative

##### Cluster of Excellence “Nanosystems Initiative Munich”

1. Project Area A: *Single Electron and Spin Systems*  
R. Gross, S.T.B. Gönnerwein
2. Project Area C: *Quantum Information Nanosystems*  
R. Gross, A. Marx

#### German Research Foundation: Collaborative Research Centers

##### Collaborative Research Center 631: “Solid-State Quantum Information Processing: Physical Concepts and Materials Aspects”

1. Project A3: *Superconducting Quantum Circuits as Basic Elements for Quantum Information Processing*  
R. Gross, A. Marx
2. Project A8: *Cavity Quantum Electrodynamics with Superconducting Devices*  
A. Marx, R. Gross
3. Project S: *Coordination of the Collaborative Research Center*  
R. Gross

##### Transregional Collaborative Research Center TRR 80: “From Electronic Correlations to Functionality”

1. Project A2: *Spatially und Momentum Resolved Raman Studies of Correlated Systems*  
R. Hackl

## German Research Foundation: Research Units

**Research Unit 538:** “Doping Dependence of Phase Transitions and Ordering Phenomena in Cuprate Superconductors”

1. Project: *Single Crystal Growth of p- and n-doped Cuprate Superconductors*  
A. Erb, R. Gross (Az. ER 342/1-1+2, ER 342/1-3)
2. Project: *Raman Studies of Competing Ordering Phenomena in Cuprates*  
R. Hackl, R. Gross (Az. HA 2071/3-1+2, HA 2071/3-3+4)
3. Project: *Coordination of the Research Unit*  
R. Hackl (Az. HA 2071/4-1+2, HA 2071/4-3+4)

## German Research Foundation: Priority Programs

1. Project: *Novel functional layer structures based on artificial heteroepitaxial multilayers of transition metal oxides*  
within the DFG Priority Program 1157 “*Integrated Electroceramic Functional Structures*”  
R. Gross (Az. GR 1132/13-1, GR 1132/13-2 and 1132/13-3)
2. Project: *Spin injection, spin transport and controllable ferromagnetism in transition metal doped ZnO*  
within the DFG Priority Program 1285 “*Halbleiter-Spinelektronik*”  
R. Gross, S.T.B. Gönnerwein, M. Opel (Az. GR 1132/14-1, GR 1132/14-2)
3. Project: *Raman study of electron dynamics and phase transitions in iron-pnictide compounds*  
within the DFG Priority Program 1458 “*High-Temperature Superconductivity in Iron-Pnictides*”  
R. Hackl, R. Gross, B. Büchner, D. Johrendt, C. Honerkamp (Az. HA 2071/7-1)

## German Research Foundation: Research Projects

1. Project: *Doping dependent evolution of the Fermi surface and competing ordering phenomena in superconducting cuprates*  
R. Gross, M. Kartsovnik, A. Erb (Az. GR 1132/15-1)
2. Project: *Interaction between spin, lattice, and charge in non-centrosymmetric correlated metals*  
R. Hackl, R. Gross (Az. HA 2071/5-1)
3. Project: *Effect of pressure, magnetic fields, and crystal quality on the electronic ground states of low-dimensional organic conductors*  
W. Biberacher (Az. 436 RUS 113/926/0-1)
4. Project: *Local Magnetotransport Properties of Thin Ferromagnetic Layers and Heterostructures*  
S.T.B. Gönnerwein (Az. GO 944/3-1)

## European Union

1. Marie Curie Network for Initial Training (ITN): *Circuit and Cavity Quantum Electrodynamics (CCQED)*  
R. Gross, A. Marx, F. Deppe, Grant Agreement No. PITN-GA-2010-264666  
partners: several European Universities and research facilities.
2. Marie Curie Network for Initial Training (ITN): *Cavity-confined Luminophores for Advanced Photonic Materials: A Training Action for Young Researchers (FINELUMEN)*  
R. Hackl, Grant Agreement Number PITN-GA-2008-215399  
partners: several European Universities and research facilities.
3. ERA-Chemistry-network: *Hierarchically organized chemical structures: from molecules to hybrid materials*, project: *Probing Hierarchical Self-Assemblies Relevant for Drug and Vaccine Design by Employing STM*  
B.A. Hermann (project number ERA HE 5162/1-1)
4. COST Action CM0601: *Electron Controlled Chemical Lithography (ECCL)*, project in Working Group 3: *Chemical control by scanning tunneling microscopy*  
B.A. Hermann

## Alexander von Humboldt Foundation

1. Institutspartnerschaft "Kamaras-Hackl"  
R. Hackl (Förderkennzeichen 3-Fokoop-DEU/1009755)

## German Academic Exchange Service

1. German-Indian STAR Scholarship for Technology and Research, collaboration with IIT Madras (Prof. M.S.R. Rao)  
R. Gross

## Ministerio de Educacion y Ciencia, Spanien

1. Intercalación de minerales de la arcilla por medio de tratamiento con ultrasonidos y reacciones de transferencia de electrones. Producción de arcillas funcionalizadas con estructuras complejas jerarquizadas en el espacio interlaminaar.  
J.L. Perez-Rodriguez, A. Lerf (Reference No. : MAT2005-04838)

## International Doctorate Program NanoBioTechnology – IDK-NBT

1. project: *STM on magnetic layers and self-organized magnetic molecules*  
B.A. Hermann, coordination by C. Bräuchle and J. Rädler (IDK-NBT 1506-42501-1)

## Bavaria California Technology Center (BaCaTeC)

1. Collaboration project on *Materials with coupled order parameter under extreme conditions*  
R. Hackl,  
partners: Profs. T.P. Devereaux, I. Fischer, W.L. Mao

## Conferences and Workshops

The Walther-Meißner-Institute has organized/co-organized the following conferences and workshops in 2010:

1. **International Workshop on Properties of High- $T_c$  Superconductors"**  
April 13 - 16, 2010, Munich Residence, Germany.



The workshop was organized by the Research Unit 538 of the German Research Foundation. The meeting was bringing together more than 50 scientists, working on high temperature superconductivity both in theory and experiment.

2. **Course 3 on "Applied Physics and Electronics" of the Ferienakademie 2010**  
September 19 – October 01, 2010, Sarntal, Italy.



The course was held together with Prof. Klaus Mecke from the University of Erlangen/Nuremberg within the Ferienakademie. The Ferienakademie is jointly organized by the Technische Universität München, the University of Erlangen/Nuremberg, and the University of Stuttgart and takes place in the Italian Alps.

3. **Miniworkshop on "Complex Order and Fluctuations",**  
October 21, 2010, Garching, Germany.
4. **DGKK-Workshop on "Intermetallic and Oxide Materials with Spin and Charge Correlations"**  
October 14 - 15, 2010, Garching, Germany.

The workshop was organized by the “Deutsche Gesellschaft für Kristallwachstum und Kristallzüchtung (DGKK)” at the Walther-Meißner-Institute.



## Collaborations

Other collaborations without direct project funding involve:

- Stanford University, Stanford, USA (Prof. T.P. Devereaux, M. Greven, Z.-X. Shen, I. Fisher)
- Institute for Quantum Computing, University of Waterloo, Waterloo, ON, Canada (Prof. Dr. F.K. Wilhelm)
- Departamento de Química Física, Universidad del País Vasco - Euskal Herriko Unibertsitatea, Bilbao, Spain (Prof. E. Solano)
- Green Innovation Research Laboratories, NEC Corporation, Japan (Dr. Y. Nakamura, Dr. J.S. Tsai, Dr. K. Inomata, Dr. T. Yamamoto)
- NTT Basic Research Laboratories, Japan (Dr. K. Semba)
- Instituto de Ciencia de Materiales de Sevilla, Spain (Prof. J. Poyato, Prof. J.L. Perez-Rodriguez)
- Research Institute for Solid State Physics and Optics, Hungarian Academy of Sciences, Budapest, Hungary (Prof. K. Kamaras and Prof. I. Túttő, Dr. J. Balogh)
- University of Rome “La Sapienza”, Rome, Italy (Prof. S. Caprara, Prof. C. Di Castro and Prof. M. Grilli)
- Hungarian Academy of Sciences, Budapest University of Technology and Economics, Budapest, Hungary (Dr. A. Virosztek, Prof. A. Zawadowski, G. Mihály)
- Central Research Institute of the Electric Power Industry, Tokyo, Japan (Dr. S. Ono and Dr. Y. Ando)
- University of Fribourg (Prof. C. Bernhard)
- University of Basel, Institute of Inorganic Chemistry, Switzerland (Prof. E. Constable, Prof. C. Housecroft)
- University of Basel, Institute of Physics, Switzerland (Prof. H.-J. Güntherodt)
- European Synchrotron Radiation Facility (ESRF), Grenoble (Dr. H. Müller, Dr. J. Crigin-ski Cezar, Dr. D. Mannix)
- LEPES, CNRS, Grenoble (Dr. J. Dumas and Prof. C. Schlenker)
- Materials Science Research Centre, IIT Madras, India (Prof. M.S. Ramachandra Rao)
- High Magnetic Field Laboratory, Toulouse (C. Proust, D. Vignolles)
- ETH-Zurich, Switzerland (Profs. L. Degiorgi, R. Monnier, Dr. M. Lavagnini)
- Chalmers University of Technology Gothenburg, Sweden (Prof. P. Delsing)
- Universidad del País Vasco, San Sebastian, Spain (Prof. A. Rubio)
- MINT Center, University of Alabama (Prof. A. Gupta)
- Materials Physics Laboratory, Helsinki University of Technology, Finland (Dr. Tero Heikkilä)
- Department of Condensed Matter Physics, The Weizmann Institute of Science, Israel (Dr. Moshe Schechter)
- Kavli Institute of NanoScience, Delft University of Technology, Delft, The Netherlands (Prof. T.M. Klapwijk)
- Institute for Experimental Physics, Slovakian Academy of Sciences, Kosice (Prof. K. Flachbart)
- High-Magnetic-Field Laboratory, Grenoble, France (Dr. I. Sheikin)

- B. Verkin Institute for Low Temperature Research and Engineering, Kharkov, Ukraine (Prof. V.G. Peschansky)
- Landau Institute for Theoretical Physics, Chernogolovka, Russia (Dr. P. Grigoriev)
- Russian Academy of Sciences, Chernogolovka, Russia (N. Kushch, A. Palnichenko)
- High Magnetic Field Laboratory, Dresden (M. Bartkowiak, J. Wosnitza)
- University of Bonn, Germany (Prof. W. Mader)
- IFW Dresden, Germany (Prof. B. Büchner, Prof. J. Fink, Dr. S.V. Borisenko, Dr. M. Knupfer)
- Max-Planck-Institut für Festkörperforschung, Stuttgart, Germany (Prof. B. Keimer)
- University of Tübingen, Germany (Prof. R. Kleiner, Prof. D. Kölle)
- University of Würzburg, Germany (Prof. W. Hanke, Prof. F. Assaad, Prof. C. Honerkamp, Dr. M. Potthoff)
- University of Augsburg, Germany (Dr. S. Kohler, Prof. Dr. P. Hänggi)
- University of Hamburg, Germany (Dr. G. Meier, Prof. W. Wurth)
- Abt. Halbleiterphysik, University of Ulm, Germany (Dr. W. Limmer)
- RWTH Aachen, Germany (Dr. B. Beschoten)
- Georg-August-Universität Göttingen (Prof. M. Müzenberg)
- Institut für Experimentelle und Angewandte Physik, Universität Regensburg (Prof. Christian Back, Dr. Georg Woltersdorf, Dr. Dominique Bougeard)
- Universität Duisburg-Essen, Germany (Dr. A. Ney)
- Universität Bielefeld, Germany (Dr. A. Thomas)
- University of British Columbia, Vancouver, Canada (Prof. D. Bonn, Prof. A. Damascelli)
- Max-Planck-Institut für Chemische Physik fester Stoffe, Dresden, Germany (Prof. F. Steglich)
- Walter Schottky Institut, TU München, Germany (Prof. G. Abstreiter, Prof. J. Finley, Dr. M. Brandt, Prof. A. Holleitner)
- Ludwig-Maximilians-Universität München, Germany (Prof. J.P. Kotthaus, Prof. J. von Delft, Prof. E. Frey, Prof. T. Franosch, Prof. J. Rädler, Dr. F. Marquardt, Dr. B. Nickel)
- Ludwig-Maximilians-Universität München, Department Chemie (Prof. Hubert Ebert, Dr. Diemo Ködderitzsch)
- Lehrstuhl E10, Physik Department, TU München, Germany (Prof. D. Grundler)
- Institut für Festkörperforschung, Forschungszentrum Jülich, Germany (Dr. Rainer Bruchhaus)
- University of Birmingham, UK (Prof. E.M. Forgan)
- Paul Scherrer Institute, ETH Zürich (Prof. Joel Mesot)
- University of Geneva, Switzerland (O. Fischer)
- Royal Holloway University, London UK (Prof. J. Saunders)
- University of Liverpool, UK (Dr. J. Goff)
- CNRS Grenoble, France (Prof. H. Godfrin)
- University of Florida, USA (Prof. D. Adams, Prof. Y. Takano)
- Universidad de Zaragoza, Spain (Prof. L. Morellon, Prof. J.M. de Teresa)
- EPFL Lausanne, Switzerland (Prof. H. Ronnov)
- University of New South Wales, Sydney, Australia (M. Simmons, A. Morello)
- McMaster University, Hamilton, Canada (Prof. J.P. Carbotte)
- Technische Universität Graz, Austria (Dr. E. Schachinger)

- Universität Konstanz (Prof. A. Leitenstorfer, Dr. J. Demsar, Dr. A. Pashkin)
- BMW Group, Munich, Germany (Dr. J. Schnagl)
- Siemens AG, CT MM 2, Munich, Germany (Dr. R. Matz)
- Attocube, Munich, Germany
- Concentris GmbH, Basel, Switzerland
- BASF AG, Mannheim, Germany
- THEVA Dünnschichttechnik, Ismaning, Germany (Dr. W. Prusseit)

## Research visits

Extended visits of members of the Walther-Meißner-Institute at other research laboratories:

1. **Matthias Opel**  
Universidad de Zaragoza, Spain  
16. 05. - 18. 05. 2010
2. **Rudolf Hackl**  
Stanford University, Stanford USA  
09. 03. - 03. 04. 2010
3. **Rudolf Hackl**  
Hungarian Academy of Sciences and University of Technology and Economics, Budapest, Hungary  
19. 09. - 02. 10. 2010
4. **Anton Lerf**  
Instituto de Ciencia de Materiales de Sevilla, Spain  
15. 05. - 01. 06. 2010
5. **Toni Helm**  
High Magnetic Field Laboratory, Dresden  
31. 01. - 13. 02. 2010, 24. 05. - 05. 06. 2010
6. **Mark Kartsovnik, Werner Biberacher**  
High Magnetic Field Laboratory, Toulouse, France  
25. - 30. 04. 2010
7. **Mark Kartsovnik, Toni Helm**  
High Magnetic Field Laboratory Grenoble, France  
25. 07. - 02. 08. 2010
8. **Mark Kartsovnik, Toni Helm**  
High Magnetic Field Laboratory, Dresden  
17. - 30. 10. 2010



## Conference Talks and Seminar Lectures

### Bea Botka

1. **Tip enhanced Raman spectroscopy**  
Biannual Meeting of the EU Marie Curie Project, Parma, Italy.  
08. 04. 2010
2. **A systematic study of optical and Raman spectra of peapod-based DWNTs**  
International Krutyn Summer School 2010, Krutyn, Poland.  
17. 06. 2010

### Franz Czeschka

1. **Giant magnetic anisotropy changes in  $\text{Sr}_2\text{CrReO}_6$  thin films on  $\text{BaTiO}_3$**   
International Conference on Superconductivity and Magnetism, Antalya, Turkey.  
29. 04. 2010

### Frank Deppe

1. **Superconducting flux qubits, resonators, and propagating quantum microwaves**  
Solid-State Systems for Quantum Information Processing, Bilbao, Spain.  
09. - 11. 02. 2010
2. **Superconducting flux qubits, resonators, and propagating quantum microwaves**  
Workshop on Quantum Physics using Superconducting Artificial Atoms and Nanomechanics, Atsugi, Japan.  
04. - 05. 03. 2010
3. **Selection rules for multiphoton excitations in a qubit-resonator system**  
APS March Meeting 2010, Portland, USA.  
15. - 19. 03. 2010
4. **Selection rules for multiphoton excitations in a qubit-resonator system**  
Spring Meeting of the German Physical Society, Regensburg, Germany.  
21. - 26. 03. 2010
5. **Strong and ultrastrong coupling in circuit quantum electrodynamics with superconducting flux qubits**  
Solid Fall Workshop, Munich, Germany.  
07. - 08. 10. 2010
6. **Superconducting Flux Quantum Circuits: Ultrastrong Coupling and Propagating Quantum Microwaves**  
3. Physikalisches Institut der Universität Stuttgart, Germany.  
30. 11. 2010
7. **Superconducting flux quantum circuits: Symmetry breaking, ultrastrong coupling, and propagating quantum microwaves**  
Theoretische Physik I, Universität Augsburg, Germany.  
09. 12. 2010

### Hans-Martin Eiter

1. **Raman scattering evidence for a cascade-like evolution of the charge-density-wave collective amplitude mode**  
Spring Meeting of the German Physical Society, Regensburg, Germany.  
21. - 26. 03. 2010

2. **Recent Results in DyTe<sub>3</sub> and ErTe<sub>3</sub>**  
Miniworkshop on Complex Order and Fluctuations, Garching, Germany.  
21. 07. 2010

### Sebastian Gönnerwein

1. **Voltage-Controlled Spin Mechanics**  
Seminar "Physik nanostrukturierter Systeme", Ludwig-Maximilians-Universität, Munich, Germany.  
17. 05. 2010
2. **Voltage-Controlled Spin Mechanics**  
Seminar des Instituts für Festkörperphysik, Karlsruhe Institute of Technology (KIT), Karlsruhe, Germany.  
06. 05. 2010
3. **Voltage-Controlled Spin Mechanics**  
invited talk, International Conference on Nanoscale Magnetism, Gebze, Turkey.  
30. 09. 2010

### Rudolf Gross

1. **Complex Oxide Heterostructures: Tuning Materials Properties and Functionalities by Strain**  
invited talk, International Workshop on "Functionality of Oxide Interfaces and Multiferroic Materials", Kloster Irsee, Germany.  
March 01 – 05, 2010
2. **Superconductivity**  
tutorial lecture, 41<sup>th</sup> IFF Spring School on "Electronic Oxides – Correlation Phenomena, Exotic Phases and Novel Functionalities", Forschungszentrum Jülich, Germany.  
March 08 – 19, 2010
3. **Strain Engineering of Materials Properties and Functionalities in Complex Oxide Heterostructures**  
invited talk, 452<sup>nd</sup> WE-Heraeus-Seminar on "Strain in Transition Metal Oxides – Tuning Magnetic and Electric Functionalities", Bad Honnef, Germany.  
March 15 – 17, 2010
4. **Revealing the Fermi Surface Evolution in Electron Doped Cuprates by High-Field Magnetotransport**  
invited talk, International Conference on "Superconductivity in Reduced Dimensions", Salzburg, Austria.  
May 4 – 8, 2010
5. **Superconducting Quantum Circuits**  
Physikalisches Kolloquium, Karlsruher Institut für Technologie, Germany.  
June 06, 2010
6. **Functional Oxides for Electronics**  
invited talk, International Conference on "Materials Science and Engineering", Darmstadt, Germany.  
August 24 – 26, 2010
7. **Progress and Future Trends in Single Electron and Spin Nanosystems**  
invited talk, NIM-GP Summer Retreat 2010, Herrsching, Germany.  
September 08 – 10, 2010
8. **Solid State Nanostructures for Quantum Electronics**  
invited talk, International Symposium on "Frontiers of the Nanoelectronics", Munich, Germany.  
September 08 – 09, 2010

9. **Fermi Surface Evolution in Electron Doped Cuprate Superconductors Revealed by High-Field Magnetotransport**  
invited talk, 11<sup>th</sup> Japanese-German Symposium on “New Quantum States and Phenomena in Condensed Matter”, Hiroshima, Japan.  
September 13 – 16, 2010
10. **Playing Quantum Games with Superconducting Circuits**  
invited talk, Workshop on “Common Perspectives of Mesoscopic Systems and Quantum Gases”, Schloss Reinsburg, Germany.  
November 28 – December 2, 2010

## Rudolf Hackl

1. **The Janus face of electrons in superconductors with high transition temperature**  
Kavli Institute for Theoretical Physics (KITP) UCSB, Santa Barbara, USA.  
11. 02. 2010
2. **What can we learn about and from the energy gap in superconductors?**  
25. Workshop on Novel Materials and Superconductors, Planneralp, Donnersbach, Austria.  
21. 02. 2010
3. **Electron dynamics in  $\text{Ba}(\text{Fe}_{1-x}\text{Co}_x)_2\text{As}_2$**   
TIPS meeting at Stanford University, Stanford, USA.  
11. 03. 2010
4. **Electron dynamics in  $\text{Ba}(\text{Fe}_{1-x}\text{Co}_x)_2\text{As}_2$**   
APS March Meeting, Portland, USA.  
19. 03. 2010
5. **Electron dynamics in  $\text{Ba}(\text{Fe}_{1-x}\text{Co}_x)_2\text{As}_2$**   
Colloquium talk at the UCSD, CA, USA.  
31. 03. 2010
6. **Electron dynamics in  $\text{Ba}(\text{Fe}_{1-x}\text{Co}_x)_2\text{As}_2$**   
LEES 2010, Les Diablerets, Switzerland.  
17. 07. 2010
7. **Raman scattering with momentum and high spatial resolution**  
International School on Microscopic and Spectroscopic Characterization of Multidimensional Materials, Budapest, Hungary.  
22. 09. 2010
8. **Perspektive der Physik**  
Carl-Friedrich von Siemens Stiftung, Munich, Germany.  
14. 10. 2010
9. **Light scattering in unconventional metals and superconductors**  
Erwin Schrödinger Institut für Theoretische Physik, Wien, Austria.  
05. 11. 2010
10. **Electronic interactions in superconductors with high transition temperature**  
Technische Universität Graz, Austria.  
22. 11. 2010

## Toni Helm

1. **Probing the Fermi Surface of an Electron-Doped Cuprate Superconductor by High-Field Magnetotransport**  
International Conference on Superconductivity and Magnetism, Antalya, Turkey.  
25. - 30. 04. 2010

## Elisabeth Hoffmann

1. **A superconducting  $180^\circ$  hybrid ring coupler for circuit quantum electrodynamics**  
Tagung "Kryoelektronische Bauelemente", Berlin, Germany.  
03. - 05. 10. 2010

## Hans Hübl

1. **Donor Spins in Silicon: Spin Control and Single Spin Readout**  
Fakultät für Physik, Ludwig-Maximilians-Universität München, Germany.  
29. 11. 2010
2. **Donor Spins in Silicon: Spin Control and Single Spin Readout**  
Fakultät für Physik, Universität Dortmund, Germany.  
06. 12. 2010

## Mark Kartsovnik

1. **Fermi surface evolution in an electron-doped cuprate superconductor revealed by high-field magnetotransport**  
Spring Meeting of the German Physical Society, Regensburg, Germany.  
21. - 26. 03. 2010
2. **Revealing the Fermi surface of electron-doped cuprate superconductors by high-field magnetotransport**  
Workshop "Properties on High-Temperature Superconductors", Munich, Germany.  
13. - 16. 04. 2010
3. **Quantum and semiclassical magnetoresistance oscillations probing the Fermi surface of electron-doped cuprate superconductors**  
2<sup>nd</sup> EuroMagNET Summer School, Ameland, The Netherlands.  
05. - 11. 09. 2010
4. **Doping-dependent high-field magnetotransport and Fermi surface of an electron-doped cuprate superconductor**  
Physical Phenomena at High Magnetic Fields, Tallahassee, USA.  
04. - 08. 12. 2010

## Florian Kretzschmar

1. **Carrier and spin dynamics in  $\text{BaFe}_2\text{As}_2$**   
Miniworkshop on Complex Order and Fluctuations, Garching, Germany.  
21. 07. 2010

## Anton Lerf

1. **Internally and externally triggered redox reactions in two Spanish vermiculites**  
Instituto de Ciencia de Materiales de Sevilla, Spain.  
15. 05. - 01. 06. 2010

## Achim Marx

1. **Superconducting Flux Qubits in Circuit QED and Detection of Weak Microwave Signals**  
Spring Meeting of the German Physical Society, Regensburg, Germany.  
21. - 26. 03. 2010

## Edwin Menzel

1. **Dual-path measurements of propagating microwave signals at the quantum level for circuit QED**  
APS March Meeting 2010, Portland, Oregon, USA  
17. 03. 2010

2. **Dual-path measurements of propagating microwave signals at the quantum level for circuit QED**  
Spring Meeting of the German Physical Society, Regensburg, Germany.  
21. - 26. 03. 2010
3. **A flux-driven Josephson parametric amplifier for experiments with propagating quantum microwaves**  
Solid Fall Workshop, Munich, Germany.  
07. - 08. 10. 2010

### Bernhard Muschler

1. **Doping dependence of the electronic properties of the iron arsenides**  
25. Workshop on Novel Materials and Superconductors, Plannersalm, Donnersbach, Austria.  
21. 02. 2010
2. **Band and momentum dependent electron dynamics in superconducting  $\text{Ba}(\text{Fe}_{1-x}\text{Co}_x)_2\text{As}_2$**   
Spring Meeting of the German Physical Society, Regensburg, Germany.  
21. - 26. 03. 2010
3. **Carrier dynamics in Co-doped FeAs**  
Miniworkshop on Complex Order and Fluctuations, Garching, Germany.  
21. 07. 2010

### Tomasz Niemczyk

1. **Strong coupling of two flux qubits to a coplanar waveguide resonator**  
Spring Meeting of the German Physical Society, Regensburg, Germany.  
21. - 26. 03. 2010
2. **Circuit QED with superconducting flux qubits**  
Doktoranden-Workshop über Festkörperbasierte Quanteninformationsverarbeitung, Wildschönau, Austria.  
08. - 10. 03. 2010

### Matthias Opel

1.  **$\text{Fe}_3\text{O}_4$  an ZnO thin films for multifunctional heterostructures**  
Max-Planck-Institut für Mikrostrukturphysik, Halle/Saale, Germany.  
21. 01. 2010
2. **Multifunctional materials based on oxide thin films and heterostructures**  
JARA-FIT Seminar, Forschungszentrum Jülich, Germany.  
02. 06. 2010
3. **Giant Magnetic Anisotropy Changes in  $\text{Sr}_2\text{CrReO}_6$  Thin Films on  $\text{BaTiO}_3$**   
Villa Conference on Complex Oxide Heterostructures, Santorini, Greece.  
16. 06. 2010
4. **Multifunctional materials based on oxide thin films and heterostructures**  
Université Paris-Sud, Palaiseau, France.  
01. 07. 2010
5. **Controllable magnetism in metal oxide films and hybrid systems**  
Seminar des DFG-Transregio TRR 80, Institut für Physik, Augsburg, Germany.  
14. 12. 2010

### Carsten Rohr

1. **Pattern Diversity Encoded by Elementary Geometrical Features**  
ECOSS27, Groningen, Niederlande  
29. 08. - 03. 09. 2010

**Manuel Schwarz****1. Gradiometric Superconducting Flux Qubit with Tunable Gap**

Doktoranden-Workshop über Festkörperbasierte Quanteninformationsverarbeitung, Wildschönau, Austria.

08. - 10. 03. 2010

**Mathias Weiler****1. Spin mechanics with surface acoustic waves**

International Conference of Superconductivity and Magnetism, Antalya, Turkey.

20. - 25. 04. 2010

## Lectures, Seminars, Courses and other Scientific Activities

Several members of Walther-Meißner-Institut give lectures and seminars at the Technische Universität München.

### Lectures

#### Dietrich Einzel

- |            |  |
|------------|--|
| WS 2009/10 | <ul style="list-style-type: none"> <li>• Mathematische Methoden der Physik I (Mathematical Methods of Physics I)</li> <li>• Übungen zu Mathematische Methoden der Physik I (Mathematical Methods of Physics I, Problem Sessions)</li> <li>• WMI-Seminar über aktuelle Fragen der Tieftemperatur-Festkörperphysik (WMI Seminar on Current Topics of Low Temperature Solid State Physics, with R. Gross, S.T.B. Gönnerwein, A. Marx, M. Opel, R. Hackl)</li> </ul>   |
| SS 2010    | <ul style="list-style-type: none"> <li>• Mathematische Methoden der Physik II (Mathematical Methods of Physics II)</li> <li>• Übungen zu Mathematische Methoden der Physik II (Mathematical Methods of Physics II, Problem Sessions)</li> <li>• WMI-Seminar über aktuelle Fragen der Tieftemperatur-Festkörperphysik (WMI Seminar on Current Topics of Low Temperature Solid-State Physics, with R. Gross, S.T.B. Gönnerwein, A. Marx, M. Opel, R. Hackl)</li> </ul>   |
| WS 2010/11 | <ul style="list-style-type: none"> <li>• Mathematische Methoden der Physik I (Mathematical Methods of Physics I)</li> <li>• Übungen zu Mathematische Methoden der Physik I (Mathematical Methods of Physics I, Problem Sessions)</li> <li>• WMI-Seminar über aktuelle Fragen der Tieftemperatur-Festkörperphysik (WMI Seminar on Current Topics of Low Temperature Solid-State Physics, with R. Gross, S.T.B. Gönnerwein, H. Hübl, A. Marx, M. Opel, R. Hackl)</li> <li>• Seminar on Advances in Solid-State Physics (with R. Gross, M. Opel, A. Marx, S.T.B. Gönnerwein)</li> </ul> |

#### Frank Deppe

- |            |   |
|------------|---|
| WS 2010/11 | <ul style="list-style-type: none"> <li>• Angewandte Supraleitung (Applied Superconductivity)</li> <li>• Übungen zu Angewandte Supraleitung (Applied Superconductivity, Problem Sessions)</li> <li>• Seminar on Superconducting Quantum Circuits (with R. Gross, A. Marx)</li> </ul> |
|------------|---|

#### Rudolf Gross

- |            |  |
|------------|--|
| WS 2009/10 | <ul style="list-style-type: none"> <li>• Angewandte Supraleitung (Applied Superconductivity, with A. Marx)</li> <li>• Supraleitung und Tieftemperaturphysik I (Superconductivity and Low Temperature Physics I)</li> </ul> |
|------------|--|

- Übungen zu Supraleitung und Tieftemperaturphysik I (Superconductivity and Low Temperature Physics I, Problem Sessions)
  - WMI-Seminar über aktuelle Fragen der Tieftemperatur-Festkörperphysik (WMI Seminar on Current Topics of Low Temperature Solid-State Physics, with D. Einzel, S.T.B. Gönnerwein, R. Hackl, H. Hübl, A. Marx, M. Opel)
  - Seminar on Advances in Solid-State Physics (with D. Einzel, S.T.B. Gönnerwein, R. Hackl, H. Hübl, A. Marx, M. Opel)
  - Festkörperkolloquium (Colloquium on Solid-State Physics, with D. Einzel)
- SS 2010
- Supraleitung und Tieftemperaturphysik II (Superconductivity and Low Temperature Physics II)
  - Übungen zu Supraleitung und Tieftemperaturphysik II (Superconductivity and Low Temperature Physics II, Problem Sessions)
  - Seminar on Advances in Solid-State Physics (with D. Einzel, S.T.B. Gönnerwein, R. Hackl, H. Hübl, A. Marx, M. Opel)
  - WMI-Seminar über aktuelle Fragen der Tieftemperatur-Festkörperphysik (WMI Seminar on Current Topics of Low Temperature Solid-State Physics, with D. Einzel, S.T.B. Gönnerwein, R. Hackl, H. Hübl, A. Marx, M. Opel)
  - Seminar on Superconducting Quantum Circuits (with R. Gross, A. Marx)
  - Festkörperkolloquium (Colloquium on Solid-State Physics, with D. Einzel)
- WS 2010/11
- Physik der kondensierten Materie I (Condensed Matter Physics I)
  - Tutorium zur Physik der kondensierten Materie I (Condensed Matter Physics I, Tutorium)
  - Übungen zur Physik der kondensierten Materie I (Condensed Matter Physics I, Problem Sessions, with R. Hackl, D. Einzel)
  - WMI-Seminar über aktuelle Fragen der Tieftemperatur-Festkörperphysik (WMI Seminar on Current Topics of Low Temperature Solid-State Physics, with D. Einzel, S.T.B. Gönnerwein, R. Hackl, H. Hübl, A. Marx, M. Opel)
  - Seminar on Advances in Solid-State Physics (with D. Einzel, S.T.B. Gönnerwein, R. Hackl, H. Hübl, A. Marx, M. Opel)
  - Seminar on Superconducting Quantum Circuits (with R. Gross, A. Marx)
  - Festkörperkolloquium (Colloquium on Solid-State Physics, with D. Einzel)

### Sebastian T.B. Gönnerwein

- WS 2009/10
- Seminar on Advances in Solid-State Physics (with D. Einzel, R. Gross, R. Hackl, H. Hübl, A. Marx, M. Opel)
  - WMI-Seminar über aktuelle Fragen der Tieftemperatur-Festkörperphysik (WMI Seminar on Current Topics of Low Temperature Solid State Physics, with D. Einzel, R. Gross, R. Hackl, H. Hübl, A. Marx, M. Opel)

- Seminar zu aktuellen Fragen der Magneto- und Spinelektronik (Seminar on Current Topics in Magneto and Spin Electronics, with M. Brandt, M. Opel)
- SS 2010
- Seminar: Spinmechanik und Spindynamik
  - Seminar on Advances in Solid-State Physics (with D. Einzel, R. Gross, R. Hackl, H. Hübl, A. Marx, M. Opel)
  - WMI-Seminar über aktuelle Fragen der Tieftemperatur-Festkörperphysik (WMI Seminar on Current Topics of Low Temperature Solid-State Physics, with D. Einzel, R. Gross, R. Hackl, H. Hübl, A. Marx, M. Opel)
  - Seminar zu aktuellen Fragen der Magneto- und Spinelektronik (Seminar on Current Topics in Magneto and Spin Electronics, with M. Brandt, M. Opel)
- WS 2010/11
- Seminar on Advances in Solid-State Physics (with D. Einzel, R. Gross, R. Hackl, H. Hübl, A. Marx, M. Opel)
  - Seminar: Spin Caloritronics and Spin Pumping
  - WMI-Seminar über aktuelle Fragen der Tieftemperatur-Festkörperphysik (WMI Seminar on Current Topics of Low Temperature Solid State Physics, with D. Einzel, R. Gross, R. Hackl, H. Hübl, A. Marx, M. Opel)
  - Seminar zu aktuellen Fragen der Magneto- und Spinelektronik (Seminar on Current Topics in Magneto and Spin Electronics, with M. Brandt, M. Opel)

### Rudi Hackl

- WS 2009/10
- WMI-Seminar über aktuelle Fragen der Tieftemperatur-Festkörperphysik (WMI Seminar on Current Topics of Low Temperature Solid-State Physics, with D. Einzel, R. Gross, S.T.B. Gönnerwein, H. Hübl, A. Marx, M. Opel)
  - Seminar: Experimental methods and electronic correlations (with C. Hugenschmidt and C. Pfeleiderer)
  - Seminar on Advances in Solid-State Physics (with D. Einzel, R. Gross, S.T.B. Gönnerwein, H. Hübl, A. Marx, M. Opel)
- SS 2010
- WMI-Seminar über aktuelle Fragen der Tieftemperatur-Festkörperphysik (WMI Seminar on Current Topics of Low Temperature Solid-State Physics, with D. Einzel, R. Gross, S.T.B. Gönnerwein, H. Hübl, A. Marx, M. Opel)
  - Seminar: Many-body effects and scattering methods (with C. Pfeleiderer, W. Zwerger)
- WS 2010/11
- Supraleitung und Tieftemperaturphysik I (Superconductivity and Low Temperature Physics I)
  - Problems and Solutions in Superconductivity (with D. Einzel, R. Gross)
  - WMI-Seminar über aktuelle Fragen der Tieftemperatur-Festkörperphysik (WMI Seminar on Current Topics of Low Temperature Solid-State Physics, with D. Einzel, R. Gross, S.T.B. Gönnerwein, H. Hübl, A. Marx, M. Opel)

- Seminar on Advances in Solid-State Physics (with D. Einzel, R. Gross, S.T.B. Gönnerwein, H. Hübl, A. Marx, M. Opel)

### Hans Huebl

- |            |  |
|------------|--|
| WS 2009/10 | <ul style="list-style-type: none"> <li>• Magnetismus mit Tutorium (Magnetism)</li> <li>• Seminar on Advances in Solid-State Physics (with D. Einzel, R. Gross, S.T.B. Gönnerwein, R. Hackl, A. Marx, M. Opel)</li> <li>• WMI-Seminar über aktuelle Fragen der Tieftemperatur-Festkörperphysik (WMI Seminar on Current Topics of Low Temperature Solid State Physics, with D. Einzel, R. Gross, S.T.B. Gönnerwein, R. Hackl, A. Marx, M. Opel)</li> </ul> |
| SS 2010    | <ul style="list-style-type: none"> <li>• Spinelektronik mit Tutorium (Spin Electronics)</li> <li>• Seminar on Advances in Solid-State Physics (with R. Gross, A. Marx, M. Opel, S.T.B. Gönnerwein, D. Einzel)</li> <li>• WMI-Seminar über aktuelle Fragen der Tieftemperatur-Festkörperphysik (WMI Seminar on Current Topics of Low Temperature Solid-State Physics, with D. Einzel, R. Gross, S.T.B. Gönnerwein, R. Hackl, A. Marx, M. Opel)</li> </ul> |
| WS 2010/11 | <ul style="list-style-type: none"> <li>• Magnetismus mit Tutorium (Magnetism)</li> <li>• Seminar on Advances in Solid-State Physics (with D. Einzel, R. Gross, S.T.B. Gönnerwein, R. Hackl, A. Marx, M. Opel)</li> <li>• WMI-Seminar über aktuelle Fragen der Tieftemperatur-Festkörperphysik (WMI Seminar on Current Topics of Low Temperature Solid State Physics, with D. Einzel, R. Gross, S.T.B. Gönnerwein, R. Hackl, A. Marx, M. Opel)</li> </ul> |

### Anton Lurf

- |            |   |
|------------|---|
| WS 2009/10 | <ul style="list-style-type: none"> <li>• Moderne Aspekte der Chemie für Physiker I (Modern Aspects of Chemistry for Physicists I)</li> <li>• Stoffströme in Natur und Technik (Material Flow in Nature and Technology, with Prof. K. Köhler)</li> </ul> |
| SS 2010    | <ul style="list-style-type: none"> <li>• Moderne Aspekte der Chemie für Physiker I (Modern Aspects of Chemistry for Physicists I)</li> <li>• Nanostrukturierte Materie (Nanostructured Matter, with Prof. J. Plank)</li> </ul>                          |
| WS 2010/11 | <ul style="list-style-type: none"> <li>• Moderne Aspekte der Chemie für Physiker I (Modern Aspects of Chemistry for Physicists I)</li> <li>• Stoffströme in Natur und Technik (Material Flow in Nature and Technology, with Prof. K. Köhler)</li> </ul> |

## The WMI Seminars

### The Friday Seminar – Walther-Meißner-Seminar on Current Topics in Low Temperature Physics

- 1. Full scale simulation of blazars**  
Max Häberlein, Walther-Meißner-Institut, Germany  
15. 01. 2010
- 2. Magnetic Raman Scattering of Antiferromagnetic Nano-particles**  
Prof. Dr. Peter Knoll, Karl-Franzens-Universität, Graz, Austria  
23. 04. 2010
- 3. Negative Refraction and Superlensing with Perovskite Thin Films**  
Prof. Dr. Lukas Eng, Institut für Angewandte Optik, TU Dresden, Germany  
30. 04. 2010
- 4. Phonon-induced Many-body Effects in the Quasiparticle Band Structure**  
Prof. Dr. Claudia Ambrosch-Draxl, Universität Leoben, Austria  
07. 05. 2010
- 5. Transport in doubly gated suspended bilayer graphene in electric and magnetic fields**  
Dr. Thomas Weitz, Harvard University, Cambridge, USA  
12. 05. 2010
- 6. Recent Studies in Superconductivity at Extreme Pressure**  
Prof. Dr. Jim Schilling, Washington University, St. Louis, USA  
28. 05. 2010
- 7. Evolution of stable p-type ZnO**  
Prof. Dr. M.S. Ramachandra Rao, Indian Institute of Technology, Madras, India  
09. 06. 2010
- 8. The Spin Hall Effect and the Importance of Impurities**  
Martin Gradhand, Martin-Luther-Universität Halle-Wittenberg, Halle  
11. 06. 2010
- 9. Microbridge Junctions for Superconducting Phase Qubits**  
Dr. Martin Weides, University of California, Santa Barbara, USA  
17. 06. 2010
- 10. Probing the Fermi Surface of Hole-Doped Cuprates**  
Dr. David Vignolles, Laboratoire National de Champs Magnétiques Pulsés, Toulouse, France  
21. 06. 2010
- 11. Ferromagnetic Resonance Driven by the Spin-Orbit Interaction**  
Prof. Dr. Andrew Ferguson, University of Cambridge, UK  
02. 07. 2010
- 12. Strain induced multiferroicity and electric control of magnetization**  
Dr. Marjana Lezaic, IFF Forschungszentrum Jülich, Germany  
09. 07. 2010
- 13. Quantum Optics on a Chip - Photon Counters and NOON States**  
Prof. Dr. Frank Wilhelm, University of Waterloo, Canada  
16. 07. 2010
- 14. Quantum optics with circuits on a chip: The habitat of artificial atoms and microwave photons**  
Dr. Frank Deppe, Walther-Meißner-Institut, Germany  
16. 07. 2010
- 15. R&D in Industry: Optical Oxygen Analyser for Biopharma and Brewery Applications**  
Dr. Francesca Venturini, Mettler-Toledo GmbH, Greifensee, Switzerland  
23. 07. 2010
- 16. GOCE - erste Ergebnisse einer besonderen Satellitenmission**  
Dr. Anja Schlicht, Forschungseinrichtung Satellitengeodäsie, TU München, Germany  
23. 07. 2010

17. **Ultra-sensitive SQUID microsusceptometer for magnetic measurements at very low temperatures and broad bandwidth**  
Maria José Martínez-Pérez, University of Zaragoza, Spain  
26. 07. 2010
18. **Interface superconductivity - possible origin of high critical temperature in layered superconductors**  
Prof. Dr. S.S. Tinchev, Bulgarian Academy of Sciences, Sofia, Bulgaria  
11. 10. 2010
19. **Quantum simulations in trapped ions**  
Dr. Jorge Casanova, Universidad del País Vasco, Bilbao, Spain  
22. 10. 2010
20. **Resistive switching for memory applications based on nanoionic transport and redox reactions**  
Dr. Rainer Bruchhaus, IFF Forschungszentrum Jülich, Germany  
29. 10. 2010
21. **Selective darkening of degenerate transitions in a system of two coupled flux qubits**  
Dr. Pieter de Groot, Technische Universität Delft, The Netherlands  
19. 11. 2010
22. **Electroresistance effects in ultrathin ferroelectric barriers**  
Daniel Pantel, Max-Planck-Institut, Halle, Germany  
10. 12. 2010

### Topical Seminar on Advances in Solid State Physics – WS 2009/2010, SS 2010 and WS 2010/2011

1. **Preliminary discussion and assignment of topics**  
Rudolf Gross, Walther-Meißner-Institut  
20. 10. 2009
2. **Ladungsdichtewellen in  $R\text{Te}_3$  ( $R = \text{La, Dy, } \dots$ )**  
Hans-Martin Eiter, Walther-Meißner-Institut  
03. 11. 2009
3. **Hochfrequente mechanische Verspannung und Magnetotransporteigenschaften von ferromagnetischen Dünnschichtstrukturen**  
Christian Heeg, Technische Universität München  
10. 11. 2009
4. **Cross-Correlation Measurements of the First Two Moments of Propagating Microwave Signals**  
Edwin Menzel, Walther-Meißner-Institut  
17. 11. 2009
5. **Generation of Arbitrary Quantum States in a Superconducting Resonator**  
Peter Eder, Technische Universität München  
24. 11. 2009
6. **Superconductivity without Electron-Phonon Interaction**  
Christoph Rathgeber, Technische Universität München  
01. 12. 2009
7. **Methods of Crystal growth from melts and solutions**  
Christian Wachauf, Technische Universität München  
08. 12. 2009
8. **Optomechanics**  
Max Rietzl, Technische Universität München  
15. 12. 2009
9. **Tunable Tunneling Barriers**  
Alexander Kaiser, Technische Universität München  
12. 01. 2010
10. **Physics of Interfaces in Oxide Heterostructures**  
Marta Krawczyk, Technische Universität München

19. 01. 2010
11. **Light Propagation in Metals**  
Felix Bilger, Technische Universität München  
19. 01. 2010
12. **Superconducting Group-IV Semiconductors**  
Michael Puls, Technische Universität München  
26. 01. 2010
13. **Topological Insulators**  
Stefan Beer, Technische Universität München  
02. 02. 2010
14. **Multiferroic Magneto-electronic Composites: Foundations and Applications**  
Roberta Kriegel, Technische Universität München  
09. 02. 2010
15. **Preliminary discussion and assignment of topics**  
Rudolf Gross, Walther-Meißner-Institut  
20. 04. 2010
16. **Widerstandsthermometrie bei mK-Temperaturen**  
Karl Neumaier, Walther-Meißner-Institut  
27. 04. 2010
17. **Giant Nernst effect due to fluctuating Cooper pairs in superconductors**  
Andrey Varlamov, CNR-SPIN Consiglio Nazionale delle Ricerche, Rome, Italy  
11. 05. 2010
18. **Towards Ultrastrong Coupling of Superconducting Transmission Line Resonators**  
Thomas Weißl, Walther-Meißner-Institut  
18. 05. 2010
19. **Spin injection experiments using Fe<sub>3</sub>O<sub>4</sub>/ZnO heterostructures**  
Deepak Venkateshvaran, Walther-Meißner-Institut  
25. 05. 2010
20. **Structural, magnetic, electrical, and magnetoelectric properties of undoped and doped BiFeO<sub>3</sub>**  
Prof. Dr. M.S. Ramachandra Rao, Materials Science Research Center, IIT, Madras, India  
01. 06. 2010
21. **The role of gauge invariance in the theory of superconductivity**  
Dietrich Einzel, Walther-Meißner-Institut  
08. 06. 2010
22. **Characterization of a flux-driven Josephson parametric amplifier**  
Alexander Baust, Walther-Meißner-Institut  
15. 06. 2010
23. **Raman Scattering on Metals and Superconductors**  
Andreas Baum, Technische Universität München  
22. 06. 2010
24. **Experiments at High Pressure: Quantum Critical Phenomena, Electronic and Lattice Instabilities**  
Robert Bollig, Technische Universität München  
29. 06. 2010
25. **Hochfrequenzspektroskopie ferromagnetischer Mikrostrukturen**  
Martin Radlmeier, Walther-Meißner-Institut  
06. 07. 2010
26. **Surface Plasmons at Magnetic Interfaces**  
Themistoklis Sidiropoulos, Walther-Meißner-Institut  
13. 07. 2010
27. **Preliminary discussion and assignment of topics**  
Rudolf Gross, Walther-Meißner-Institut  
19. 10. 2010

28. **Study of correlated electron systems with applied pressure**  
Reinhard Rossner, Walther-Meißner-Institut  
02. 11. 2010
29. **Vibrational studies of confined luminescent systems**  
Nitin Chelwani, Hungarian Academy of Sciences, Budapest, Ungarn  
16. 11. 2010
30. **Graphene**  
Michael Schreier, Technische Universität München  
23. 11. 2010
31. **Silicon Detectors and Integrated Readout Electronics for X-ray Imaging, Spectroscopy, and Synchrotron Applications**  
Davide Bianchi, Max-Planck-Institut für Extraterrestische Physik, Garching  
30. 11. 2010
32. **Growth and Characterization of Ferromagnetic Heusler Compound Thin Films**  
Alexander Krupp, Walther-Meißner-Institut  
07. 12. 2010
33. **Thermodynamics of Phase Diagrams**  
Andrea Winnerl, Technische Universität München  
14. 12. 2010
34. **Magnetic Digital Logic and Memory Circuits**  
Alexander Büse, Technische Universität München  
21. 12. 2010
35. **Josephson Light-Emitting Diode**  
Alexander Kupijai, Technische Universität München  
18. 01. 2011

### **Topical Seminar: Spin Mechanics and Spin Dynamics – SS 2010**

1. **Preliminary discussion and assignment of topics**  
Sebastian Gönnerwein, Walther-Meißner-Institut  
21. 04. 2010
2. **Von der magnetischen freien Enthalpie zum Stoner-Wohlfarth-Modell**  
Sebastian Gönnerwein, Walther-Meißner-Institut  
05. 05. 2010
3. **Spin transfer torque**  
Michael Kunz, Walther-Meißner-Institut  
19. 05. 2010
4. **Spin-Mechanik**  
Mathias Weiler, Walther-Meißner-Institut  
26. 05. 2010
5. **Gepulste Elektronenspinresonanz**  
Hans Hübl, Walther-Meißner-Institut  
09. 06. 2010
6. **Ferromagnetische Resonanz**  
Andreas Brandlmaier, Walther-Meißner-Institut  
16. 06. 2010
7. **Breitband-FMR und magnetische Dämpfung**  
Martin Radlmeier, Walther-Meißner-Institut  
23. 06. 2010
8. **Spin waves in confined magnetic structures**  
Christoph Zollitsch, Technische Universität München  
30. 06. 2010
9. **Winkelabhängiger Magnetowiderstand**  
Alexander Krupp, Walther-Meißner-Institut  
07. 07. 2010

10. **Spin caloritronics**  
Deepak Venkateshvaran, Walther-Meißner-Institut  
14. 07. 2010
11. **Magneto-Plasmonics**  
Themis Sidiropoulos, Walther-Meißner-Institut  
21. 07. 2010

### **Topical Seminar on Superconducting Quantum Circuits – SS 2010 and WS 2010/2011**

1. **Preliminary discussion and assignment of topics**  
Frank Deppe, Walther-Meißner-Institut  
20. 04. 2010
2. **Towards Ultrastrong Coupling of Superconducting Transmission Line Resonators**  
Thomas Weißl, Walther-Meißner-Institut  
18. 05. 2010
3. **Joint Readout for Superconducting Qubits in Circuit QED**  
Peter Eder, Technische Universität München  
01. 06. 2010
4. **Superconducting artificial atoms in open space**  
Jan Götz, Technische Universität München  
22. 06. 2010
5. **Optical Quantum Computation**  
Franz Sterr, Technische Universität München  
13. 07. 2010
  
6. **Preliminary discussion and assignment of topics**  
Frank Deppe, Achim Marx, Rudolf Gross, Walther-Meißner-Institut  
19. 10. 2010
7. **Microwave-Induced Cooling of a Superconducting Qubit**  
Thomas Losinger, Technische Universität München  
23. 11. 2010
8. **Frozen Light**  
Benno Blaschke, Technische Universität München  
14. 12. 2010
9. **Ultra-strong Light-Matter Interaction**  
Franz Sterr, Technische Universität München  
18. 01. 2011
10. **Strong Coupling between Spins and Cavities**  
Nikolaj Bittner, Technische Universität München  
25. 01. 2011

### **Solid State Colloquium**

The WMI has organized the Solid-State Colloquium of the Faculty of Physics in WS 2009/2010, SS 2010, and WS 2010/2011. The detailed program can be found on the WMI webpage: <http://www.wmi.badw-muenchen.de/teaching/Seminars/fkkoll.html>



## Staff of the Walther-Meißner-Institute

### Director

Prof. Dr. Rudolf Gross

### Deputy Director

Dr. Werner Biberacher

### Technical Director

Dr. Achim Marx

### Administration/Secretary's Office

Ludwig Ossiander

Emel Dönertas

### Scientific Staff

Dr. Werner Biberacher

Dr. Frank Deppe

Dr. habil. Dietrich Einzel

Dr. habil. Andreas Erb

Dr. Sebastian Gönnenwein

Dr. habil. Rudolf Hackl

Dr. Hans Hübl

Dr. Mark Kartsovnik

Prof. Dr. Anton Lerf

Dr. Achim Marx

Dr. Matthias Opel

Dr. Kurt Uhlig

Dipl.-Phys. Matthias Althammer

Dipl.-Phys. Alexander Baust

Dipl.-Phys. Bea Botka

Dipl.-Phys. Andreas Brandlmaier

Dipl.-Phys. Johannes Büttner

Dipl.-Phys. Franz Czeschka

Dipl.-Phys. Hans-Martin Eiter

Dipl.-Phys. Stephan Geprägs

Dipl.-Phys. Katrin Gruber

Dipl.-Phys. Max Häberlein

Dipl.-Phys. Toni Helm

Dipl.-Phys. Fredrik Hocke

Dipl.-Phys. Elisabeth Hoffmann

Dipl.-Phys. Florian Kretzschmar

Dipl.-Phys. Edwin Menzel

Dipl.-Phys. Bernhard Muschler

Dipl.-Phys. Thomas Niemczyk

Dipl.-Phys. Carsten Rohr

Dipl.-Phys. Manuel Schwarz

Dipl.-Phys. Mathias Weiler

Dipl.-Phys. Georg Wild

### Technical Staff

Peter Binkert

Dipl.-Ing. (FH) Thomas Brenninger

Dipl.-Ing. (FH) Ulrich Guggenberger

Dieter Guratzsch

Astrid Habel

Karen Helm-Knapp

Dipl.-Ing. (FH) Josef Höss

Namwar Jahanmehr

Julius Klaus

Robert Müller

Jan Naundorf

Georg Nitschke

Christian Reichlmeier

Harald Schwaiger

Helmut Thies

Siegfried Wanninger

**Assistants**

Sybilla Plöderl

Brigitte Steinberg

**Permanent Guests**

Prof. Dr. B. S. Chandrasekhar

Dr. Robert Doll

Dr. Karl Neumaier

Dr. Christian Probst

Prof. Dr. Erwin Schuberth

## Guest Researchers

1. Prof. Dr. B.S. Chandrasekhar  
permanent guest
2. Dr. Robert Doll  
permanent guest
3. Dr. Karl Neumaier  
permanent guest
4. Dr. Christian Probst  
permanent guest
5. Prof. Dr. Erwin Schubert  
permanent guest
6. Dr. S. Mahapatra, Centre for Quantum Computing Technology, University of New South Wales  
20. 02. - 13. 03. 2010
7. Dr. Nataliya D. Kushch, Institute of Problems of Chemical Physics, Chernogolovka, Russia  
25. 02. - 26. 03. 2010
8. Dr. M. Lavagnini, ETH Zürich, Switzerland  
01. 04. - 31. 07. 2010
9. Dr. Oleg Vyaselev, Institute of Solid Physics, Chernogolovka, Russia  
09. 05. - 23. 06. 2010
10. Prof. Dr. M.S. Ramachandra Rao, Materials Science Research Centre, IIT Madras, Chennai, India  
19. 05. - 16. 06. 2010
11. Dr. David Vignolles, Laboratoire National de Champs Magnétiques Pulsés, Toulouse, France  
20. 06. - 24. 06. 2010
12. Dr. Sergei Pesotskii, Institute of Problems of Chemical Physics, Chernogolovka, Russia  
29. 06. - 28. 07. 2010
13. E. Senthil Kumar, Indian Institute of Technology IIT, Madras, Chennai, India  
01. 07. - 30. 09. 2010
14. Prof. Dr. Thomas P. Devereaux, Stanford Institute of Materials and Energy Science (SIMES), Stanford and Geballe Laboratory of Advanced Materials, Stanford University, USA  
01. 07. - 29. 07. 2010
15. Dr. Brian Moritz, Stanford University of Materials and Energy Science (SIMES) Stanford, USA  
12. 07. - 28. 07. 2010
16. Dr. Lex Kemper, Stanford Institute of Materials and Energy Science (SIMES), Stanford and Geballe Laboratory of Advanced Materials, Stanford University, USA  
12. 07. - 28. 07. 2010
17. Yvonne Kung, Stanford University, Stanford USA  
12. 07. - 28. 07. 2010
18. Prof. Dr. Juan Poyato Ferrera, Instituto de Ciencia de Materiales, Sevilla, Spain  
05. 07. - 28. 07. 2010
19. Prof. Dr. Alfred Zawadowski, Budapest University of Technology and Economics, Bu-

- dapest, Ungarn  
26. 07. - 08. 08. 2010, 05. 12. - 18. 12. 2010
20. M. Fuchsle, Centre for Quantum Computing Technology, University of New South Wales  
26. 07. - 15. 08. 2010
21. Dr. Juan-Jose Garcia Ripoll, Instituto de Fisica Fundamental, CSIC, Madrid, Spain  
05. 09. - 10. 09. 2010
22. Jorge Casanova, Universidad del Pais Vasco, Bilbao, Spain  
06. 10. - 24. 10. 2010
23. Dr. Guillermo Romero, Universidad del Pais Vasco, Bilbao, Spain  
06. 10. - 24. 10. 2010
24. Dr. Daniel Ballester, Universidad del Pais Vasco, Bilbao, Spain  
06. 10. - 24. 10. 2010
25. Prof. Dr. Katalin Kamarás, Hungarian Academy of Science, Budapest, Hungary  
09. 11. - 17. 11. 2010
26. Nitin Chelvani Hungarian Academy of Sciences, Budapest, Ungarn  
15. 11. - 17. 11. 2010
27. Prof. Vladimir Zverev, Institute of Solid Physics, Chernogolovka, Russia  
15. 11. - 21. 12. 2010
28. Prof. I. Tüttö, Hungarian Academy of Sciences, Budapest, Hungary  
05. 12. - 18. 12. 2010

## Commission for Low Temperature Physics

Members of the Commission for Low Temperature Research of the Bavarian Academy of Sciences and Humanities:

Kaiser, Wolfgang, Leiter (Technische Universität München)  
Abstreiter, Gerhard, stellv. Leiter (Technische Universität München)  
Gross, Rudolf (Walther-Meißner-Institut)  
Landwehr, Gottfried (Universität Würzburg)  
Hänsch, Theodor (Max-Planck-Institut für Quantenoptik, Garching)  
Kotthaus, Jörg Peter (Ludwig-Maximilians-Universität München)  
Schwoerer, Markus (Universität Bayreuth)  
Vollhardt, Dieter (Universität Augsburg)  
Weiss, Dieter (Universität Regensburg)